Instrument Study of the Lunar Dust eXplorer (LDX) for a Lunar Lander Mission

Von der Fakultät Luft- und Raumfahrttechnik und Geodäsie der Universität Stuttgart
zur Erlangung der Würde eines Doktor-Ingenieurs (Dr.-Ing.) genehmigte Abhandlung

Vorgelegt von

Yanwei Li

aus Hebei, China

Hauptberichter:	Priv.-Doz. Dr.-Ing. Ralf Srama
Mitberichter:	Prof. Dr.-Ing. Stefanos Fasoulas
Mitberichter:	Prof. Dr. Eberhard Grün
Tag der mündlichen Prüfung:	02.11.2015

Institut für Raumfahrtsysteme der Universität Stuttgart
2016

Contents

List of Figures

List of Tables

Kurzfassung

Eine der höchsten wissenschaftlichen Prioritäten für eine zukünftige bemannte oder robotische Erforschung des Mondes stellt der Mondstaub dar. Einschläge von Meteoroiden auf der Oberfläche mit einer durchschnittlichen Geschwindigkeit von 17 $\mathrm{km \cdot s^{-1}}$ bestimmen die Eigenschaften der Mondoberfläche. Die Einschlagsprozesse sind deshalb wesentlicher Bestandteil des Umgebungsmodells des Mondes. Die aktuellen Modelle zur Beschreibung der Dynamik des Mondstaubs sind unvollständig und ungenau und decken sich nicht mit den Beobachtungen. Deshalb sind exakte Messungen dicht über der Mondoberfläche mit zuverlässigen Staubsensoren notwendig. Die zukünftigen Mondlander-Missionen berücksichtigen die Messung der Staubtransportphänomene an der Mondoberfläche. In dieser Arbeit wird ein Designkonzept für ein Staubinstrument beschrieben, um langsame und schnelle geladene feine Regolithpartikel zu charakterisieren. Die Messmethode des Sensors basiert auf dem Prinzip der Ladungsinduktion. Das entwickelte Experiment *Lunar Dust eXplorer* (LDX) hat eine geringe Masse von 1.2 kg, eine elektrische Leistung von 1.1 W (digitale Elektronik), eine empfindliche Fläche von 400 cm^2 und bestimmt den Geschwindigkeitsvektor der Trajektorien von einzelnen Staubpartikeln. Die Empfindlichkeit des Sensors erlaubt die Messung von Partikelgröβen von unter einem Mikrometer. Darüber hinaus hat LDX ein separates Einschlagstarget, um den interplanetaren Staubhintergrund zu überwachen.

Der LDX Sensor ist aus drei Ebenen aufgebaut, die segmentierte Gitterelektroden enthalten. Alle Signale der Gitterelektroden werden ladungsempfindlich verstärkt und digitalisiert. Aus dem Vergleich der einzelnen Induktionssignale lässt sich die Partikeltrajektorie berechnen. Labordaten wurden mit numerischen Simulationen verglichen. Die durchgeführten Simulationen und Experimente zeigen, dass mit dem vorgestellten Sensorsystem die Trajektorien mit Unsicherheiten von unter 2° und die absoluten Positionsgenauigkeiten der Partikel mit eine Genauigkeit von weniger als 2 mm bestimmt werden können.

Der LDX Sensor wurde entworfen, gefertigt und am 2 MV Van-de-Graaff Beschleuniger des Max-Planck-Instituts für Kernphysik in Heidelberg erfolgreich getestet.

Diese Beschleunigeranlage ist weltweit einzigartig und erlaubt die Simulation von Hochgeschwindigkeits-Einschlagsprozessen von Mikropartikeln. Er wird vom Institut für Raumfahrtsystem (IRS) der Universität Stuttgart betrieben. Die experimentellen Ergebnisse zeigen Genauigkeiten von besser als $\pm 5\%$ bei der Bestimmung der Partikelprimärladung und von besser als $\pm 7\%$ bei der Bestimmung der Partikelgeschwindigkeit.

Welche Staubpopulationen kann LDX auf der Mondoberfläche untersuchen? Wie groß ist der Anteil der zurückfallenden Ejektapartikel auf die Oberfläche und was ist ihre Winkel und Geschwindigkeitsverteilung? Autodyn 14.0/2D-Software wurde verwendet, um den Einschlag von Mikrometeoriten auf der Mondoberfläche zu simulieren. Die Projektile wurden als Kugeln mit einem Durchmesser von 10 μm und mit einer Geschwindigkeit von 17 km·s^{-1} angenommen. Die verwendeten Einschlagswinkel hatten Werte von 15°, 30°, 45°, 60°, 75°, und 90°. In der sogenannten Frühphase des Einschlagsprozesses koppelt das Projektil noch Energie und Impuls in das Target ein. Ein Teil dieser Ejekta aus der Frühphase können dann von einem Sensor, der auf der Mondoberfläche platziert wird, erfasst werden (wie z.B. dem Lunar Ejecta and Meteorites (LEAM) experiment). Alternativ lässt sich der Sensor an einem Mondlander anbringen (LDX). Die Ergebnisse der Simulationen zeigen, dass die meisten Partikel der nachweisbaren Auswurfmasse sehr kleine Geschwindigkeiten (<100 m·s^{-1}) hat. Es gibt nur wenige schnelle Ejekta mit Geschwindigketen von mehr als 1 km·s^{-1}. Vergleicht man die Simulationsergebnisse mit der neuesten Interpretation der LEAM Daten, so können die Ejekta als Ursache für die Apolloergebnisse herangezogen werden. Untersucht man die Beobachtungsgeometrien für die Oberflächenejekta, so muss ein Sensor, der an einem Lander in gewisser Höhe befestigt ist, gegenüber einem System direkt auf der Mondoberfläche, für die Messung von Ejekta mit hohen Geschwindigkeiten bevorzugt werden.

Ein neu entwickeltes Instrument wie LDX ist ein leistungsfähiges Werkzeug, um den Mondstaub-Umgebung zu studieren. Zukünftige Mondmissionen basieren nicht nur auf Landestrukturen, sie setzen auch vermehrt auf mobile kleine Rover. Ein Staubdetektor an Bord eines Mondfahrzeugs hätte einige Vorteile. Man kann in verschiedenen Regionen der Oberfläche Messungen durchführen. Der Sensor kann die Wechselwirkung des Rovers mit dem Plasma, den elektrischen Feldern und den Staub studieren. Aber es gibt auch wesentliche Nachteile. Die Instrumente an Bord eines Rovers müssen kleinere Massen haben und dürfen keine großen Datenmengen produzieren. In dieser Arbeit wurden daher auch zwei vereinfachte Entwürfe für einen Rover-Staubsensor entwickelt. Diese Systeme haben eine geringere Anzahl von Elektroden und eine kleinere Masse als der ursprüngliche LDX Sensor. Ein Design basiert auf einer runden Baumform des Gehäuses

(LDX-c), das zweite Design nutzt einen quadratischen Sensorquerschnitt (LDX-s). Die Messgenauigkeit der beiden Detektorkonstruktionen ist ähnlich zu LDX, jedoch verringert sich die Genauigkeit der Flugbahnbestimmung um bis zu 2 Grad.

Im Vergleich zu den bisherigen Ergebnissen der Apollomissionen, erlaubt das hier entwickelte Sensorkonzept wesentlich zuverlässigere und genauere Messungen, um insbesondere die möglichen Gefahren bei der zukünftigen Mondexploration einzuschätzen.

Abstract

One of the highest-priority issues for a future human or robotic lunar exploration is the fine lunar dust created by meteoroid bombardment on the lunar surface with an average speed of 17 km·s^{-1}. This problem should be studied in depth in order to develop an environment model for future lunar explorations. The proposed ESA lunar lander mission requires the measurement of dust transport phenomena above the lunar surface. In response to the mission requirements, an instrument design concept was developed, simulated, manufactured and tested at the Heidelberg dust accelerator facility. In contrast to former detectors, the sensor is capable to measure charged particles in a broader speed window, ranging from as low as meters per second to several kilometers per second. Furthermore, the new instrument approach is optimized for the instrument requirements of the lunar lander concept investigated by ESA. The *Lunar Dust eXplorer* (LDX) has a low mass of 1.2 kg and consumes a power of 1.1 W (digital electronics). The sensitive area of LDX is approximately 400 cm^2. It measures the charge, speed and trajectory of individual dust particles. Meanwhile, LDX has an impact ionization target to monitor the mass of interplanetary dust and high speed ejecta.

In the beginning of this study, the charge induction signals of the detector were simulated using the COULOMB software package in order to constrain the sensor accuracies. Simulations reveal trajectory uncertainties of better than 2° with an absolute position accuracy of better than 2 mm. Following simulations, a laboratory model of the LDX sensor was designed, manufactured and tested at the 2 MV Van-de-Graaff accelerator located at the Max-Planck Institute for Nuclear Physics in Heidelberg. This accelerator is a worldwide unique facility to simulate hyper-velocity impacts of micron and sub-micron particles. It is currently operated by the Institute of Space System of the University of Stuttgart (IRS, Stuttgart). The experimental results additionally reveal particle primary charge uncertainties of better than ±5% and particle speed uncertainties of better than ±7%.

What are the dust populations a sensor like LDX can detect on the lunar surface? How large is the contribution by secondary ejecta falling back to the surface and what is their angular distribution and speed range? To answer these questions, the Autodyn 14.0/2D

software was used to simulate hyper-velocity impacts of micrometeoroids bombarding the lunar surface. The initial projectiles were selected as 10 μm spheres in diameter with an average speed of 17 km·s^{-1}. Furthermore, we used impact angles of 15°, 30°, 45°, 60°, 75° and 90° for these projectiles. In the early stage of the impact process, the projectile is coupling its energy and momentum to the target. A part of the ejecta grains created during this early stage can be captured by a sensor located on the lunar surface, e.g. the Lunar Ejecta and Meteorites (LEAM) experiment or mounted on a lander (e.g. LDX). The simulations show, that most of the detectable ejecta have low speeds (< 100 m·s^{-1}), and there are also a few grains with high speeds (> 1 km·s^{-1}).

The observation geometry of the sensor was investigated. Here we discuss a trade-off between a lander-mounted sensor and a surface located system. Although the LEAM data are not fully understood until today, our recent re-analysis of the data consider impact ejecta as one of the most likely sources to explain the observed event rates. Meanwhile, our studies show that a sensor mounted on the lander instead of standing on the lunar surface has more chances to measure the high speed component of the ejecta population.

The newly developed LDX sensor system is a powerful tool to study the lunar dust environment. In addition to lunar landers, smaller rover systems are also very interesting in future missions. A dust detector onboard a lunar rover would have several advantages: the measurements by the sensor can be taken at different regions of the lunar surface. Furthermore, the sensor will monitor the interaction of the rover with the lunar dust environment (plasma, electric fields, and dust). On the other hand, there are also disadvantages. The instruments onboard a rover have to maintain severe mass and data volume restrictions. Therefore we developed two further simplified designs with a lower number of electrodes and an even lower instrument mass with respect to the original LDX design. The fundamental difference between the two versions is their housing geometries. One design uses a cylindrical housing (LDX-c), and the second design has a square cross section (LDX-s). The measurement accuracies of these two detector designs are similar to LDX, but the trajectory accuracy decreases slightly by up to 2 degrees. Nevertheless, such an instrument promises, for the first time, reliable data for the properties of the lunar dust environment.

Chapter 1

Introduction

During the brief periods of time spent on the Moon during Apollo it became apparent that the lunar dust could pose significant problems for the operations of both people and equipment. Dust was found to adhere to clothing and equipment, it reduced visibility during landing, mechanical devices were severely compromised by lunar dust contamination, optical components were covered with visible dust layers and Apollo astronaut spacesuits became coated with fine-grained dust. Once inside the spacecraft dust caused breathing difficulties and inhibited vision. In addition dust was also found to prevent effective sealing of pressurised and depressurised containers. None of the containers containing rock samples from any of the Apollo missions was found to be able to hold vacuum after return to Earth due to dust grains inhibiting the knife edge indium seals. Pressurisation of lunar modules after the initial opening required more oxygen in order to counter the effects of dust on the seals. The processes by which lunar dust grains are charged and transported around the lunar surface are complex and require an understanding of the properties of dust particles and how they interact with ionising radiation and the plasma and electric field on the Moon. The Lunar Dust EXperiment (LDEX) onboard the lunar orbiter Lunar Atmosphere and Dust Environment Explorer (LADEE) identified successfully the dust cloud above the lunar surface along the spacecraft orbit [44]. However, reliable in-situ dust measurements on the lunar surface were not success until today. The newly developed dust detector placed on the lunar surface can monitor both ejecta and lofted dust, respectively [56]. Both populations are candidates to maintain the lunar dust cloud.

1.1 Lunar Dust Environment

From the Apollo missions it is known, that dust on the lunar surface can cause serious problems for exploration activities. The spacesuits of astronauts are directly exposed to the lunar dust environment. A large amount of dust grains were carried by the spacesuits into the capsule - the habitat environment astronauts need to live within. Furthermore, the dust grains have potential harmful effects on the multiple components and systems of the spacesuits [29] and other equipment like rovers. Even without a direct proof, many people think the lunar dust is one of the most plausible explanations for the mechanical control anomaly of the Yutu Rover. The ground-based studies reported by Linnarsson et al. [57] investigated the toxicity of dust on the health of the astronauts. Study topics were the abundance, size distribution and chemical reactivity of the dust grains. Impressive statements of the Apollo astronauts are given here:

'one of the most aggravating, restricting facets of lunar surface exploration is the dust and its adherence to everything no matter what kind and its restrictive friction-like action to everything it gets on. You have to live with it but you're continually fighting the dust problem both outside and inside the spacecraft.' [31].

'After lunar liftoff, when we were again in a zero g environment, a great quantity of dust floated free within the cabin. This dust made breathing without the helmet difficult, and enough particles were present in the cabin atmosphere to affect our vision. The use of a whisk broom prior to ingress would probably not be satisfactory in solving the dust problem, because the dust tends to rub deeper into the garment rather than to brush off.' [12].

People could find out better methods to protect the exploration activities (manned or robotic) from the negative effects of dust grains by understanding the surface charging effects of the fine regolith grains and the related dynamics.

The current knowledge about the dust environment at the Moon was summarized by Grün et al. [34]. The lunar dust grains are the product of meteoroid bombardment on the lunar surface. Each year, the surface of the Moon is bombarded by about 10^6 kg of interplanetary micrometeoroids of cometary or asteroidal origin. Most of these projectiles range from 10 nm to about 1 mm in size and they impact on the Moon at speeds from 10 to 72 km·s^{-1}. They may excavate the lunar soil with a yield of up to 1000 times of their own mass [34]. These impacts leave crater records on surfaces from which the micrometeoroid size distribution has been deciphered [48]. Most of the excavated mass returns to the lunar surface and blankets the lunar crust with a highly pulverized layer [35], which is called 'Lunar regolith', as shown in Figure 1.2. The finest particle grains ($< 100\ \mu$m) are called

Fig. 1.1 Spacesuits with the lunar dust. (a) Astronaut Gene Cernan unveils Apollo 17 plaque on leg of LM (Lunar Module) 'Challenger'; (b) Gene Cernan in the LM with EVA (Extra-Vehicular Activity) spacesuit; (c) EVA and (d) Gene Cernan in LM. Images are credited by NASA [62].

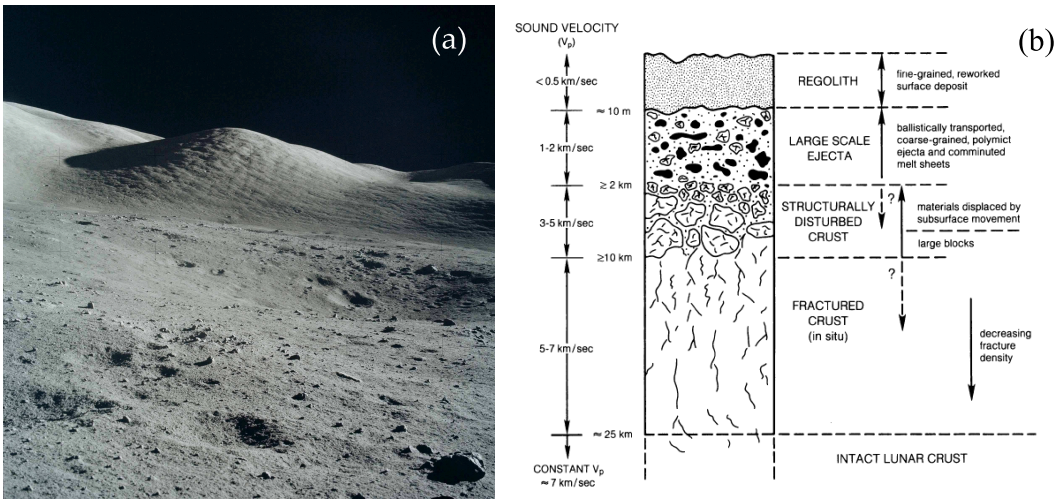

Fig. 1.2 Lunar surface. (a) The lunar regolith imaged by astronauts during the Apollo 17 mission credited by NASA; (b) The schematic cross-section illustrates the upper lunar crust [38].

simply 'Lunar dust'.

As reported by Liu et al. [58], the particle size distributions of the Apollo 11 and Apollo 17 dust samples display peaks near 0.1 and 0.2 μm, respectively (see Figure 1.3). More than 95% of the lunar dust grains are smaller than 2 μm.

Fine grains from the lunar surface can be lifted due to human activities, and there are indications that lunar fines can be electrostatically charged and naturally transported under the influence of near-surface electric fields. Observations by the Apollo astronauts of sticking dust to their space suits, even after short extravehicular activities demonstrated the importance of dust contamination control [18].

According to the observed brightness in solar corona images taken by the Apollo 15 and Apollo 17 missions, McCoy [60] set up a hypothetical model of density distribution of the levitated dust above the lunar surface. Analysis results of this model for dust concentrations in the lunar exosphere showed a decrease with altitude to approximately 0.1 cm^{-3} at an altitude of 1 km ($10^{-2}cm^{-3}$ at 10 km and possibly $10^{-5}cm^{-3}$ at 100 km). Dust reaching these altitudes falls back to the surface within seconds to minutes. Dust from 1 km altitude reaches the surface with 56 $m{\cdot}s^{-1}$ and dust grains from altitudes of 5 km fall back with an average speed of 130 $m{\cdot}s^{-1}$.

One of the most famous dust detectors located on the lunar surface is the Lunar Ejecta and Meteorites (LEAM) experiment. LEAM was deployed on the lunar surface by the Apollo 17 astronauts in order to characterize the lunar dust environment [15]. Instead of the expected low impact rate from interplanetary and interstellar dust, LEAM registered more

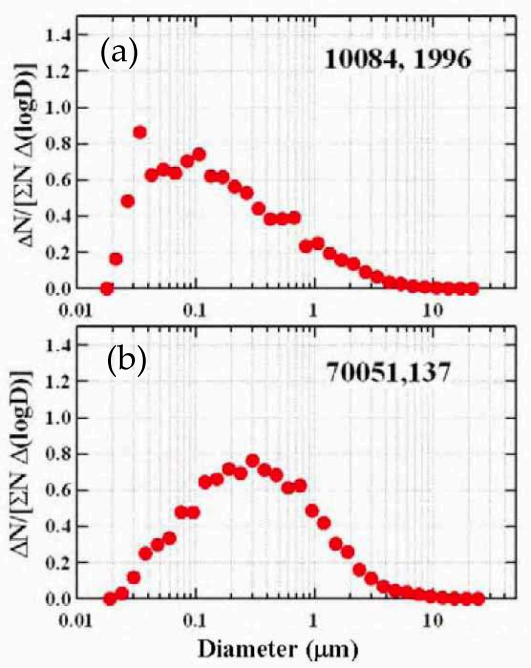

Fig. 1.3 Particle size distributions of the lunar dust sample. (a) Apollo 11 lunar dust 10084; (b) Apollo 17 lunar dust 70051. $\triangle$N is the number of particle normalized by the total number of counted particle $\sum$N and logarithmic diameter $\triangle$(logD) [58].

than one thousand of signals associated with the passage of the terminator. These signals were explained by charged particles - the lofted dust - in the initial data analysis. However, the observation results obtained by LEAM are still contradictory and they were discussed by O'Brien [63] and Grün and Horányi [33].

The surfaces of dust grains above the airless objects and in interplanetary space are embedded in the heliosphere and interact with ultraviolet (UV) light of the sun and with solar wind particles [43]. They are affected by a variety of charging mechanisms leading normally to an equilibrium potential at the grain surface of about +5 V. UV photoelectron emission dominates the charging process in regions with low plasma densities. Other contributing charging processes are sticking and penetration of plasma particles, and secondary electron emission due to the bombardment of highly energetic plasma particles [43, 85]. The highly energetic particles were thought also to play an important role in dust charging processes [59]. The surface charge Q_p of a dust particle with the potential Φ depends on the morphology of the grain. The UV light and solar wind plasma are the two main factors of the charging process in interplanetary space. For spherical particles the relation is given by:

$$Q_p = 4\pi\varepsilon_0 R_p \Phi \tag{1.1}$$

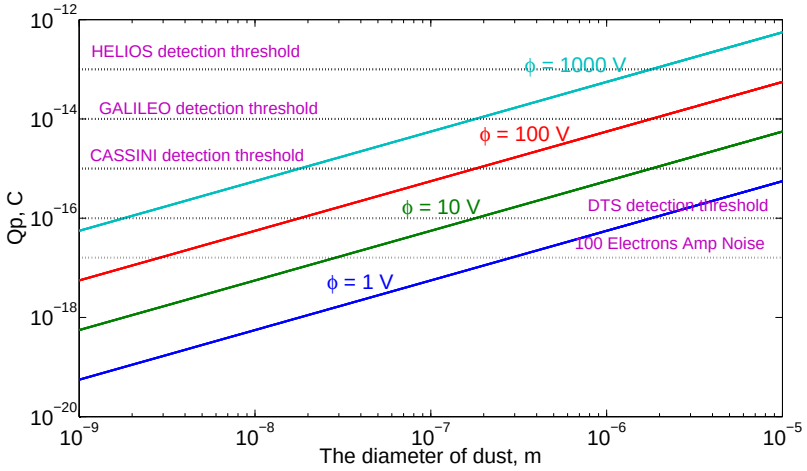

Fig. 1.4 Surface charge of dust particles calculated by Equation 1.1 and the measurement thresholds of previous detectors.

where Q_p is the particle surface charge, ε_0 is the vacuum permittivity, which has a value of 8.85×10^{-12} F·m^{-1}, R_p is the radius of the particle and Φ is the particle surface potential.

Figure 1.4 shows the possible surface charge of dust grains with surface potentials from 1 V to 1000 V, and the measurement threshold of previous charge induction detectors. What should be noted here is that the charge induction detector onboard Cassini detected the cosmic dust particle charge for the first time [52].

An impact crater is more than a mere hole on the lunar surface. The material excavated from the crater and deposited on the surrounding terrain is called ejecta. Hoerth et al. [41] studied the ejecta dynamics of porous sandstone using experimental methods. They found the ejecta cone angles separate from 44 degrees to 60 degrees for vertical impacts during the early-time stage of the ejecta cone evolution process. In the early-time stage of the impact process, pressures are highest in the impact point zone, and the materials ejected near the impact point are therefore dominated by small fragments with high speeds and shallow angles with respect to the target surface. As the process continues, ejecta with larger size, slower velocity and more vertical angle are released from the crater zone.

The secondary ejecta impact phenomenon is a fundamental process for the lunar surface change. Grün et al. [35] compared in-situ spacecraft measurements, optical observations with hyper-velocity impact experiments. He found, that the observed size distribution of lunar micron sized craters usually do not agree with the flux of interplanetary dust with masses of less than 10^{-10} g. These microcraters are probably created by the secondary ejecta impacts. Based on the experimental results from Zook et al. [90], the number of secondary impact pits from oblique impact angles is more than 2 orders of magnitude higher than from

vertical impacts. The distances that ejecta grains can be thrown on ballistic trajectories depend on both, their velocity vectors at which the materials are ejected and the gravity field of the Moon.

All airless planetary bodies are expected to be surrounded by dust clouds. One of the source mechanisms is the generation of fragments ejected from the planetary bodies surface by the bombardments of bigger interplanetary objects. Dust clouds were firstly detected by the dust detector onboard the Galileo spacecraft during the close flybys of the icy moons of Jupiter [54]. Based on the latest data, the Lunar Dust EXperiment (LDEX) sensor onboard the lunar orbiter Lunar Atmosphere and Dust Environment Explorer (LADEE) already identified the existence of a dust cloud around the lunar surface down to altitudes of 10 km [44].

When micrometeoroids or other interplanetary bodies impact on the lunar surface, individual ejecta grains follow their own ballistic trajectories in the airless environment. Ejecta grains with velocities exceeding the escape velocity on the Moon (2.4 $km \cdot s^{-1}$) contribute to the interplanetary dust cloud, which takes an important role for the determination of the dust density and flux near earth [81]. However, most of the excavated mass returns to the lunar surface and blankets the lunar crust with a highly pulverized layer [35].

1.2 ESA Lunar Lander

An important step in dealing with dust-related problems is to understand how dust grains behave in the ambient lunar environment. This will require both, advances in our theoretical understanding together with a thorough characterization of the near-surface dust-plasma environment with comprehensive in-situ observations.

The planned lunar lander mission is a robotic mission led by the human spaceflight and operations directorate at the European Space Agency (ESA). Its primary objective is to test the safe landing technology preparations for future cooperations, which will be an asset for future human and robotic exploration missions to the Moon or Mars. The ESA lunar lander mission will land in the south polar region (within about 5 degrees latitude) of the Moon. In this area, the lander life time is longer without additional thermal control or power. Figure 1.5 shows the potential landing site locations and the sketch of the ESA Lunar Lander.

The lander will be launched by a Soyuz 2.1B rocket from Guyana, which requires an upper limit on the total mass of the whole spacecraft. The platform is the most recent approach to ensure that the primary scientific objective (landing technology) is achieved.

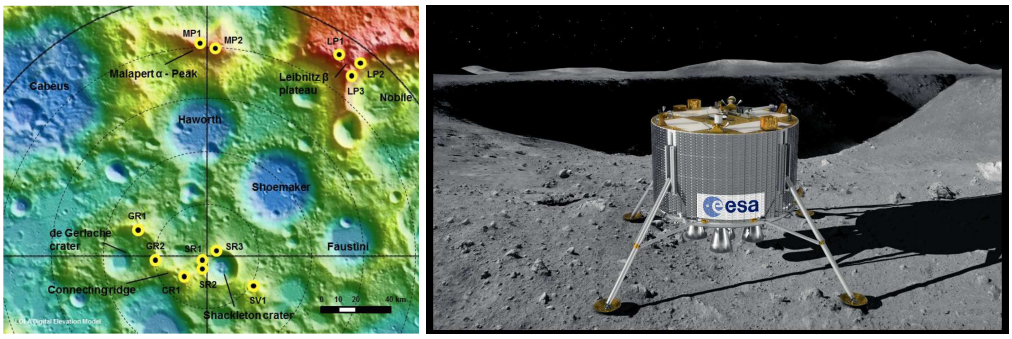

Fig. 1.5 Potential landing sites (lunar south pole) for the ESA Lunar Lander [78] and sketch of the lander on the lunar surface (image is credited by ESA).

There is no doubt that the mass of the payloads will be strictly limited.

1.3 Scientific Goals and Instrument Requirements

The current knowledge of the dust environment above the lunar surface is based on a rare set of indirect observations. Different physical processes were proposed to explain the optical and in-situ measurements. Major open questions of the lunar dust environment are:

- Were the results of the LEAM experiment unique?
- Is the dust transport triggered by lit/unlit transitions?
- How does the ejecta distribution look like?
- What is the temporal and spatial variability of the properties of the transported grains?
- What is the size, charge and velocity of mobilized dust grains above the lunar surface?
- What is the overall contribution of the three dust populations?
- What is the flux of secondary ejecta and levitated dust?

The observed rates by LEAM were too high and the electrostatic loft mechanism is not understood. What is the role of the terminator and of crater shadows? What is the temporal and spatial variability of the properties of the transported grains? The lunar surface is a large dusty-plasma laboratory such that these questions are directly related to the objectives: What is the charge distribution on the surface as a function of local time? What is the plasma density distribution above the surface, and what is the configuration of small scale local electric fields? How do the field components evolve during lit-unlit passages?

Table 1.1 Summary of scientific requirements with respect to dust particle properties.

Parameter	Range min	Range max	Accuracy	Notes
Flux ($m^2 \cdot s^{-1}$)	10^{-3}	10	10%	RQ1
Speed ($m \cdot s^{-1}$)	1	3×10^3 (3×10^4)	20%	RQ2
Mass (kg)	10^{-17}	10^{-9}	$\times 2$	RQ3
Charge (fC)	0.2	100	10%	RQ4
Trajectory (degree)	-40°	+40°	$\pm 5°$	RQ5

To answer these mentioned questions, the measurements of the dust environment above the lunar surface should be focused but not limited to: (1) the characterization of dust transport mechanisms; (2) the parameters of dust particle charge, speed and trajectory; and (3) the characterization of dust-plasma interaction (grain surface potential) with time during day, night and transition times.

The priority list of the requirements for the lunar dust detector onboard a lunar lander focuses on the characterization of dust transport mechanisms in this study, which requires the sensitive determination of dust particle charge, speed and trajectory combined with the ability to determine low dust fluxes (interplanetary dust particles (IDPs) and ejecta), as well as high dust fluxes (levitated dust). Table 1.1 shows an overview of the scientific requirements and the derived particle properties.

- RQ1: The dust flux has to be measured between 1×10^{-5} $m^2 \cdot s^{-1}$ and 10 $m^2 \cdot s^{-1}$ in order to be sensitive for sporadic events (individual ejecta or interplanetary dust particles) and particle streams as they occur from nearby surface impacts.

- RQ2: The particle speeds on the lunar surface can be very low (for the levitated dust, $\sim m \cdot s^{-1}$) and very fast (for IDPs, ~ 26 $km \cdot s^{-1}$). Such a broad speed range has to be measured.

- RQ3: The size distribution of the lunar regolith ranges from the nanometre (nm) scale to many microns. Here the mass range of from 10^{-17} to 10^{-9} kg includes particle sizes between 100 nm and 50 μm in radius, which have to be measured by the sensor.

- RQ4: The dust particles are charged to unknown surface potentials. General equilibrium potentials in the lunar environment are +5 V during the daytime and down to -100 V during the nighttime. For the low measurement threshold with a charge of 0.2 fC, equilibrium potentials correspond to 400 nm and 20 nm sized grains for the day and night measurements, respectively. A charge of 100 fC is carried by a dust

grain with radius of 200 μm in the daytime. Such a broad charge range has to be addressed by the sensor.

- RQ5: The three dust populations above the lunar surface are levitated dust, surface dust ejecta and IDPs moving on different trajectories. The levitated dust grains move slowly in the horizontal direction, whereas the surface ejecta grains enter with shallow angles the instrument aperture. IDPs are supposed to enter with a broad distribution in elevation and azimuth. The detector shall resolve the dust trajectories by 5° in order to distinguish the three populations.

The primary purpose of this study is to design a detector in order to get a high prioritization of the monitoring of dust transport mechanisms. Here, we list the scientific goals for a dust detector related with detailed measurement requirements:

- A: Distinguish levitated dust grains on the lunar surface environment from IDPs and their ejecta
- B: Search for dust transport mechanisms (levitated dust)
- C: Characterize the dust plasma interaction (grain surface potential) with time during day, night and transition times
- D: Determine relative fluxes over time of individual populations (night, day, sunrise, sunset, terminator)
- E: Characterize ejecta over direction and time (night, day, sunrise/sunset)
- F: Characterize levitated dust over time (mass, speed, direction, particle charge to mass ratio Q/m)
- G: Characterize particle charging (photoelectric/triboelectric effects)

In order to achieve the desired scientific goals, Table 1.2 shows the derived dust particle parameters and their measurement requirements for a dust detector. The scientific goals B, D and F (in blue) related with the levitated dust are of higher priority in future explorations, which require the measurements of dust particles with extremely low speeds. Depending on the final lunar lander mission duration, interplanetary or interstellar dust particles might be detected as well.

Table 1.2 Scientific goals and derived measurement requirements. TA: Trajectory accuracy.

Goal	Flux ($m^2 \cdot s^{-1}$)	Q/m ($C \cdot kg^{-1}$)	Speed ($m \cdot s^{-1}$)	Mass (kg)	Charge (fC)	TA (°)
A	10^{-5} - 10	-	1 - 3 $\times$ 10^4	10^{-17} - 10^{-9}	-	< 10
B	10^{-3} - 10	no	1 - 100	10^{-17} - 10^{-9}	0.2 - 100	< 10
C	10^{-4} - 10	yes	1 - 3 $\times$ 10^3	10^{-17} - 10^{-14}	0.2 - 100	< 5
D	10^{-3} - 10	no	1 - 3 $\times$ 10^3	10^{-17} - 10^{-9}	-	< 5
E	10^{-4} - 10	no	1 - 3 $\times$ 10^3	10^{-17} - 10^{-11}	-	< 5
F	10^{-3} - 10	yes	1 - 100	10^{-17} - 10^{-9}	0.2 - 100	< 10
G	-	yes	-	10^{-17} - 10^{-9}	0.2 - 100	-

1.4 Dust Particle Detectors

The value of a space dust trajectory sensor has been demonstrated in astronomy. Accurate triangulation of meteor tracks provides the heliocentric obit of the meteoroids that causes the known meteor phenomena. The dust detectors onboard Ulysses and Galileo provided the first statistical significant measurements of different dust populations in interplanetary space. Types of dust detectors often used in interplanetary space were: momentum sensors, penetration detectors, impact ionization detectors, capacitor discharge detectors and induced charge detectors.

(1) Momentum sensors measure the transferred momentum of a projectile impacting on a piezo-electric material plate. Momentum sensors are not sensitive to the environmental effects, such as temperature variations and energetic particle radiation. Momentum sensors were successfully employed with rather low sensitivities (> 10^{-8} g) in high dust fluxes like cometary environments. The Dust Impact Monitor (DIM) experiment onboard the Rosetta lander Philae is a cube with three sides covered with piezoelectric (PZT) detectors, aiming at measuring the physical properties of millimeter and sub-millimeter dust particles [27]. The advantages of PZT sensors are mechanical simplicity and stiffness, no additional high voltages, working high temperature, radiation tolerance, and low weight.

(2) Penetration detectors record the local destruction by a dust particle impact. The meteoroid detectors onboard Pioneer 10 and Pioneer 11 both consist of 234 pressurized cells with a device to monitor the pressure in each cell wall with a thickness of 25 μm for Pioneer 10 and 25 μm for Pioneer 11. When a meteoroid penetrates the cell wall, the gas escapes from the cell and the loss pressure is detected by the device [49]. The Polyvinylidene difluoride (PVDF) film is normally used as a penetration detector, which has higher sensitivity than the pressure cell method. A PVDF detectors employs a thin

film of the polarized polymer polyvinylidene difluoride, which has conducting electrodes on each side. The detecting element of PVDF doesn't need additional high voltage [69]. A dust particle with high speed impacting on the sensor removes local destruction of dipoles and creates a crater or a penetration hole, which results in a large and fast current pulse. The typical measurement threshold of PVDF detectors ranges from 10^{-13} g to 10^{-9} g with impact speeds above 1 km·s^{-1}. The primary objective of the High Rate Detector (HRD) onboard the Cassini spacecraft is to measure the particle flux and mass distribution during passages through the saturnian ring system [73].

(3) The impact ionization is the most sensitive method for high velocity dust measurements. A dust particle that hits the target with speed above 1 km·s^{-1} will produce a partially ionized vapor cloud. The ions and electrons of the cloud are separated in an electric field within the detector, which can be collected and reported by electrodes and/or multipliers. The instrument normally consists of a larger hemispherical impact ionization target with a central ion collector similar to dust detector onboard Galileo spacecraft [32]. Another improved design in the Cosmic Dust Analyzer (CDA) onboard Cassini is the Chemical Analyzer Target (CAT) in the middle of the impact target [73].

(4) Capacitor discharge measurement is another possible method for high speed dust. In the design, the fast dust particle penetrates the surface electrode of a charged capacitor and strikes the dielectric. Because of the hyper-velocity impact created high pressure, high temperature, impact ionization, and the locally increased electric field, the dielectric behind the shock wave front is compressed and may become conductive. As a result, a conductive path through the dielectric may form through which the capacitor is discharged. The Metal-Oxide-Silicon (MOS) capacitor discharge detector used in the European Technology Exposure Facility (EuTeF) platform is shown in Figure 1.6.

- Detector type: Capacitor discharge detector
- Mass measurement range: 10^{-13} - 10^{-10} g
- Speed measurement range: 1 - 20 km · s^{-1}
- Sensitive area: 1 m^{-2} for LDEF (total)
- Field of view: 360°
- Established detectors: EuTeF [26], MTS Explorer 46 [51] and LDEF [70]

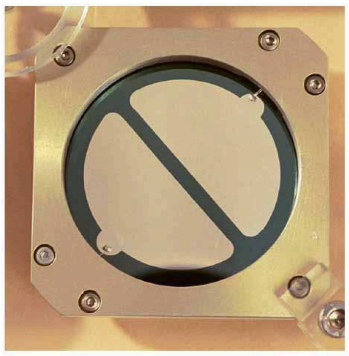

Fig. 1.6 MOS capacitor sensor [26].

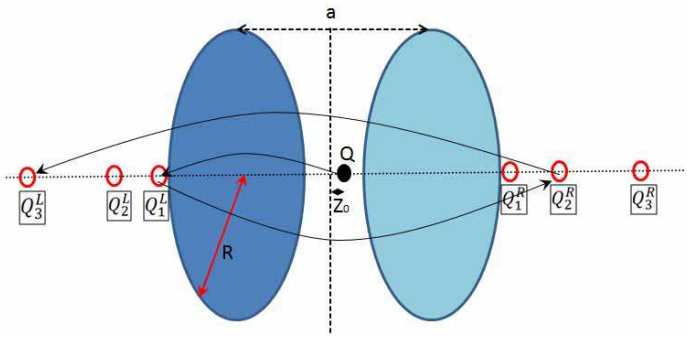

Fig. 1.7 A charged particle between two parallel plates induces a series of image charges.

(5) Charge induction is a widely used method for the measurements of charged dust grains. When a charged particle approaches a conductive electrode, it will create a certain amount of induced charge on this electrode. The induced charge signals generated on the electrode can be amplified and analyzed by charge sensitive amplifiers, which show the presence and position of the dust particle. More details about the charge induction method are shown below.

1.5 Charge Induction Method

When a charged particle gradually approaches a metal plate, the free electrons in the metal move due to the force induced by the particle electric field. The amplitude of induced charge on conductive electrode is dependent on the distance from the charged particle to the electrode and size of electrode.

A simple example of induced charge on two parallel plates is shown in Figure 1.7. The dust particle with a surface charge of Q located between two parallel metal plates induces a group of image charges on both sides. In the figure, a is the distance between the two parallel plates, and the particle has a distance of Z_0 to the center of two parallel plates. The charged dust induces an image charge Q_1^L at Z_1^L in the left side plate. This image charge conversely induces an image charge Q_2^R at Z_2^R in the right side plate. The other image charge sequences staring with Q_1^R are also shown. The images have equal values of primary charges but with opposite sign [84].

The induced charge Q_{plate} in the left side plate with a radius R is obtained by summing all image charges of the left side as shown in Equation 1.4. It is clear that the induced charge on the plate depends on the radius R of the plates and the position of the charged particle Z_0.

$$\begin{cases} Z_n^L = (2n-1)\dfrac{a}{2} - Z_0(-1)^n, & (1.2) \\ Q_n^L = -Q_{n-1}^L \left(1 - \dfrac{Z_n^L}{\sqrt{R^2 + ((Z_n^L)^2)}}\right), & (1.3) \\ Q_{plate} = -Q\left(1 - \dfrac{Z_0}{\sqrt{R^2 + ((Z_0)^2)}}\right) + \sum -Q_{n-1}^L \left(1 - \dfrac{Z_n^L}{\sqrt{R^2 + ((Z_n^L)^2)}}\right) & (1.4) \end{cases}$$

where, n = 1, 2, 3, ..., R is the radius of disk electrode, Q is the surface charge of dust grains, and Z_0 is the distance from the dust location to the center of the two plates.

The particle position Z_0 can be deduced from the induced charges Q_{plate} and the radius of the plate based on the Equation 1.4, theoretically. However, the location dependent image charge becomes asymmetric and more complex in practical applications: (1) If the particle moves out of the symmetry axis, (2) if the electrode shapes are irregular or (3) if further electrodes (e.g. the shielding walls) are added to the system. Hence, the simulation tools, such as the COULOMB software, are very useful during the development of charge induction detectors.

Actually, the charge induction method has a long history of application for charged particle measurements. In order to measure and analyze hyper-velocity dust particles in dust accelerator facility, the non-contact method using charge induction effect was selected by Friichtenicht [28] firstly. The properties of an electrically charged particle can be determined by employing Charge Sensitive Amplifiers (CSAs). During the charge induction process, electrons are attracted by the positive charge of the moving dust grain. If the electrode is connected to a CSA, the additional negative charge (electrons) move to the electrode. The induced charge on the electrode varies from 0 to 100% of the primary particle charge depending on the position of the particle and the exact electrode geometry. The values of particle charge, position and speed are obtained from the amplified output signal for individual particles.

The Cosmic Dust Analyser (CDA) onborad the Cassini spacecraft includes a charge sensitive entrance grids system (QP detector.) The QP detector has two shielding grids (front and rear, connected with cylindrical wall) and two connected parallel grids, which have a 9 degrees tilt angle with respect to the front grid (first shielding grid) of the detector. While entering the instrument, sufficiently charged particles induce characteristic charge features on the girds, which allows a reliable determination of particles charge Q_d as well as particle speed v_d (see Chapter 2).

- Detector type: Particle charge detector
- Mass threshold: 10^{-15} g
- Charge threshold: < 1 fC
- RMS noise: $1.5{\cdot}10^{-17}$ (with bandwidth from 10 kHz to 10 MHz)

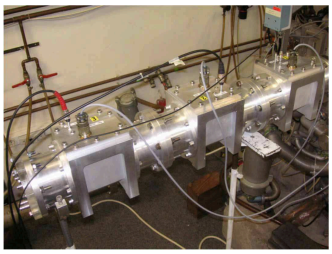

Fig. 1.8 Particle detector modules for accelerator [74].

- Detector type: Particle charge detector
- Mass threshold: 10^{-14} g
- Charge threshold: 1 fC
- Sensitive area: 0.1 m^{-2}
- Field of view: $\pm$ 64°
- Trajectory accuracy: 5° (single direction)

Fig. 1.9 Cosmic Dust Analyzer (CDA) [73].

The dust trajectory sensor determines in-situ the speed, primary charge and trajectory of micrometeoroids with high accuracy. Its underlying concept was first described by Auer [4]. Auer also reported a method for mass measurements by adding an additional vertical electrical field [5]. The measurement is based on charge induction of the particle's charge on individual wire electrodes. Each wire is connected to a separated charge sensitive amplifier (CSA) allowing the reconstruction of the particle trajectory in the three dimensional space.

Table 1.3 shows a summary of some missions and dust detector instruments. The table also includes the distance ranges where dust measurements were obtained. Detector types are momentum sensors (MS), penetration detectors (PD), impact ionization detectors and chemical analyzers (II, IA) and induced charge detectors (IC).

- Detector type: Dust Trajectory Sensor
- Mass threshold: 10^{-15} g
- Charge threshold: 0.1 fC
- Noise: 0.15 fC (100 electrons)
- Sensitive area: 0.1 m^{-2}
- Field of view: $\pm$ 45°
- Trajectory accuracy: 1° (with charge to noise radio QNR $>$ 6.25)

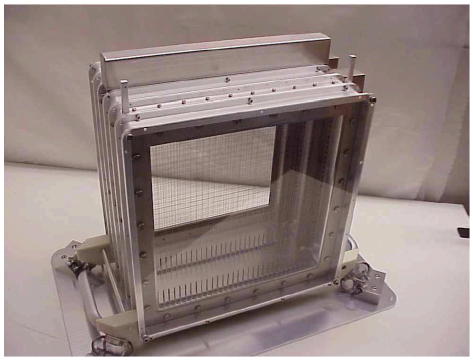

Fig. 1.10 Dust Trajectory Sensor (DTS) [75].

Table 1.3 Characteristics of in-situ dust measurements in interplanetary space.

Mission Instrument	Distance range AU	Detector type	Mass threshold g	Speed threshold km/s	Sensitive area m^2	Field of view °	Refs.
LEAM	1	II	1×10^{-14}	2.4	0.0094	60	[14]
Pioneer 8	0.75-0.99	II	1×10^{-14}	2.4	0.0075	60	[13]
Pioneer 9	0.97-1.09	II	1×10^{-14}	2.4	0.0094	60	[65]
Helios 1, 2	0.3-1	IA	9×10^{-15}	2.5	0.01	-	[24]
HEOS 2	1	II	2×10^{-15}	2.5	0.01	76	[24]
Galileo	0.7-5.4	II, IC	9×10^{-15}	2.5	0.01	76	[32]
Ulysses	1-5.4	II, IC	1.6×10^{-13}	2.5	0.01	76	[24]
VeGa 1,2	0.79-0.83						[68]
DUCMA		PD	10^{-11}	20	0.0075	360	[49]
PUMA		IA	2×10^{-15}	2	0.0005	-	[53]
SP-1		II	2×10^{-15}	2	0.0081	-	[30]
SP-2		MS, II	10^{-11}	2	0.05	-	[30]
Giotto	0.86	MS	2×10^{-8}	2	0.1	-	[30]
Cassini	1-10						[73]
CDA		II, IA	2×10^{-15}	2	0.1	45	[73]
HRD		MS	5×10^{-15}	1	0.005	360	[73]
QP		IC	10^{-10}	-	0.1	45	[52]
Stardust	0.98 - 2.7						[50]
CIDA		IA	-	6	0.0086	-	[50]
DFMI		PD	10^{-11}	6	0.02	360	[79]
SDC	2.6 -15.5	MS	10^{-12}	-	0.1	360	[45]
IKAROS	0.72 -1.08	MS	10^{-12}	-	0.54	360	[88]
LADEE	-	II	1.7×10^{-13}	1	0.01	60	[46]

Chapter 2

Dust Trajectory Measurements by Charge Induction

When a charged particle approaches a conductive plate connected to an amplifier, the electrons in the plate move due to particle's electric field in order to reach a state of equilibrium, which is known as charge induction effect. The charge induction effect has been used to detect dust particle velocities and dust particle charges in accelerator experiments [28, 74]. The principle of charge induction is also used in the cosmic dust analyzer onboard Cassini [72], Galileo and Ulysses [32, 83] to measure charges and velocities of individual particles entering the instrument aperture.

2.1 Wire Electrode Array Sensor - DTS

The Dust Trajectory Sensor (DTS) is based on the charge induction effect employing four planes of wire electrodes. A charged particle flying through a set of wires generates induced charges on the most adjacent wires. The wire geometry determines how much charge is measured at the individual channels. For the trajectory information it is necessary to locate the particle at two positions in the instrument volume. Each position sensor consists of two perpendicular planes separated by 40 mm from each other. Each plane is formed by a quadratic frame holding 16 parallel wires. An electronics board is located inside the metal frame and carries 16 charge sensitive amplifiers connected to the individual wires. This instrument requires 64 measurement channels.

All of the wire electrodes have the same length and they require a quadratic cross section in the pointing direction of the senor. Each wire electrode is attached to a separate charge sensitive amplifier (CSA) and all channels are digitized continuously. Incident dust particles

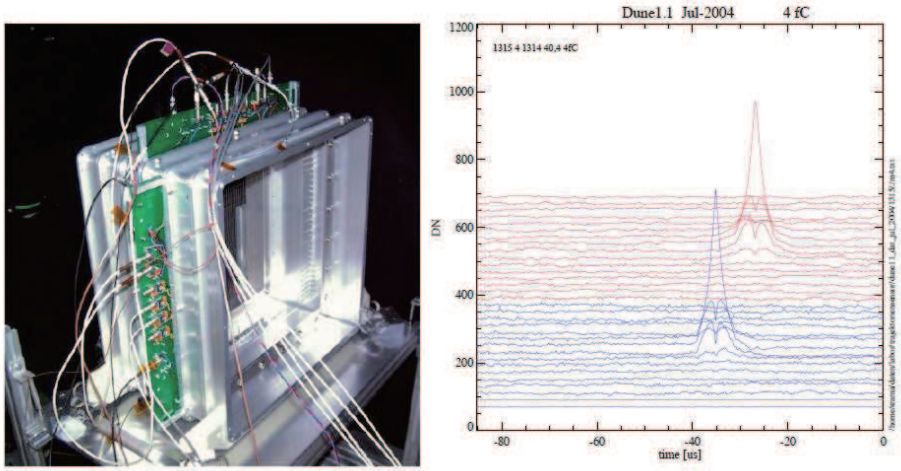

Fig. 2.1 Laboratory model of the Dust Trajectory Sensor (DTS) during tests at the Heidelberg dust accelerator facility. The wires of this laboratory model have a length of 300 mm leading to a cross section of 360 $\times$ 360 mm^2. The width of DTS is 240 mm. Right: Signals of a particle passing the wire planes of DTS. The particle speed and charge was 5 km$\cdot$s^{-1} and 4 fC, respectively [75].

are recognized by real time digital filters connected to all channels. The detector provides particle speeds, charges and trajectories with high accuracies. The very high sensitivity allows the measurement of dust particles smaller than 0.4 μm, but it also leads to sensitive response to plasma and the UV component of the sun.

This type of trajectory sensor was designed to measure high speed micrometeoroids and its underlying concept was first described by Auer [4]. Figure 2.1 shows a laboratory trajectory sensor model built by the Heidelberg Cosmic Dust group [75]. More recently, a Dust Trajectory Sensor (DTS) has been described by Auer et al. [8]. The Electrostatic Lunar Dust Analyzer (ELDA) described by Duncan [25] and Xie [86] provides a new and advanced design approach, but it is still based on the DTS concept. ELDA uses two trajectory sensors and deflection electrodes for an independent measurement of the particle charge and particle mass.

2.1.1 Simulation Model

With the help of the COULOMB software, we built up an in-scale simulation model of DTS as shown in Figure 2.2. Different geometry designs were compared by changing the diameters and distances of wire electrodes: (1) the diameter of each wire electrode was

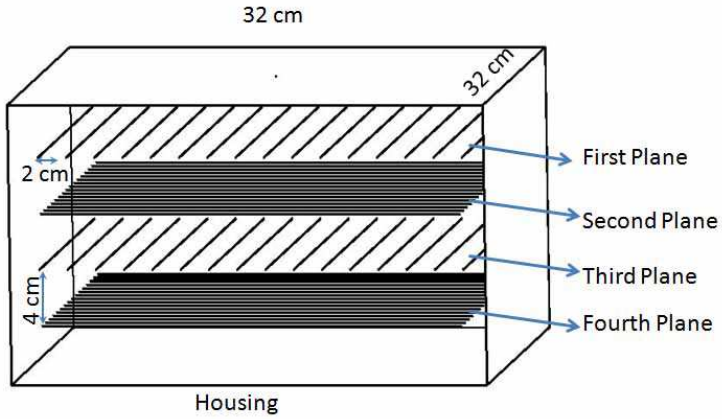

Fig. 2.2 Sketch of the simulation model for DTS. During simulation, we built up the first two planes of the sensor. The first two active planes are simulated in this study and a single plane has 16 electrodes with a distance of 2 cm between each other.

selected as 0.1 mm, 0.2 mm and 0.3 mm; and (2) the distance between each wire was 1 cm and 2 cm. The distance between the first plane and second plane were also varied and set to 3 cm, 4 cm and 5 cm.

Figure 2.3 gives some simulation results for the electrodes on the first plane of DTS which has 16 channels in total. When the charged particle passes through a position nearby channel 8, there is one peak appearing in the signal of channel 8. Another two nearby channels of channel 8 (channel 7 and channel 9) show relatively weak signals with two maxima. The induced charge in channel 8 has a value of 60% of the particle primary charge. When the insertion point moves from channel 8 to channel 9 step by step, the amplitude of the peak in channel 8 decreases. In contrast, the signal of channel 9 shows an opposite trend with decreasing distance to the particle.

2.1.2 Measurement Accuracy of Particle Charges

A lot of results about the calculation method and measurement accuracies of particle speed and trajectory by DTS have been reported [4, 8, 25, 75, 86]. Hence, in this work, we focus our analysis on the wall effect in order to answer the questions: how significant is the effect caused by shielding walls to the induced charge in nearby wire electrodes, and what is the measurement accuracy of particle charges?

The induced charges obtained by wire electrodes are determined by the relative area of the electrode, the distance to the charged particle and to the grounded electrically conductive environment (e.g. shielding wall and other electrodes). When the particle approaches an

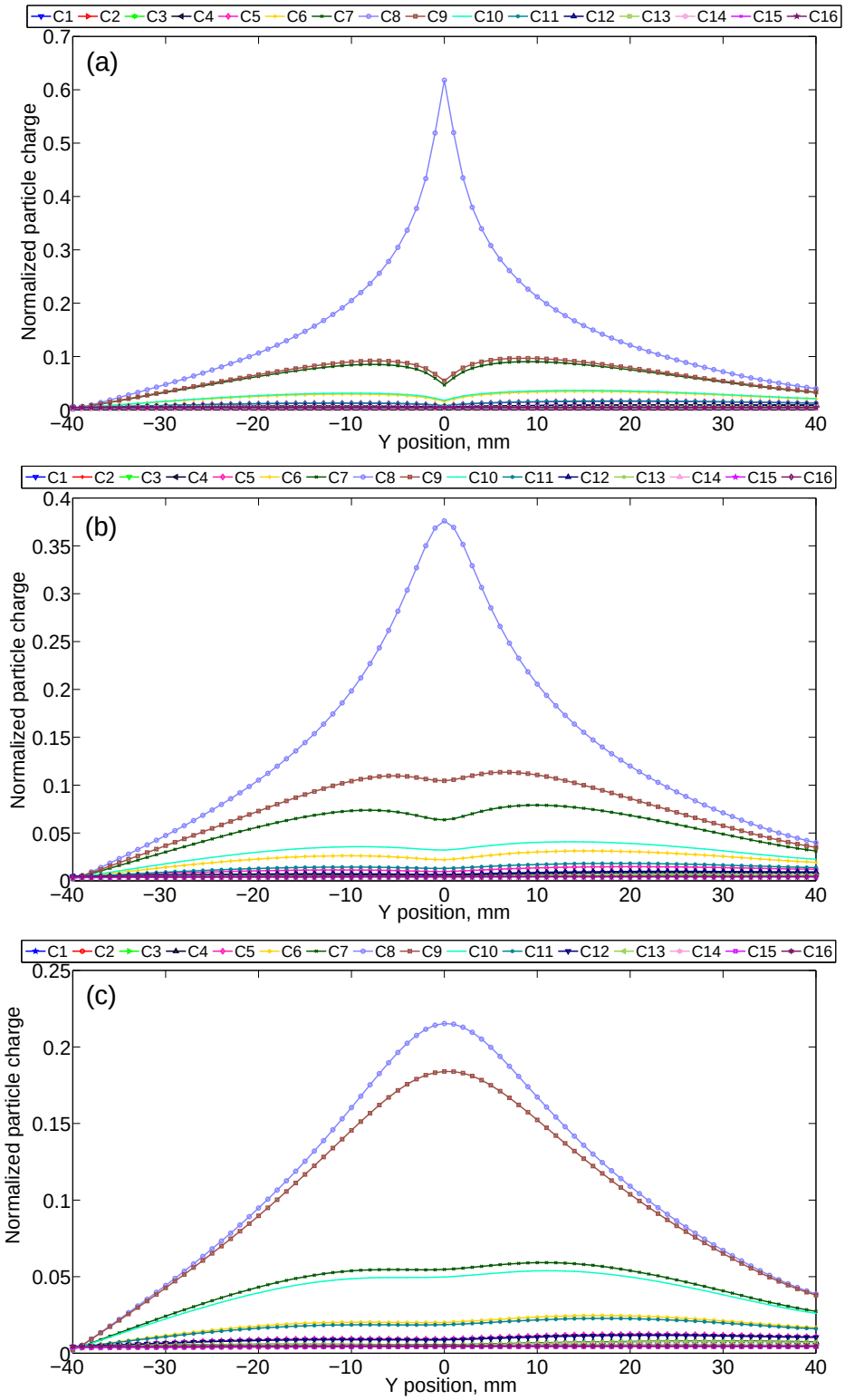

Fig. 2.3 Simulation results for the electrodes of the first plane of DTS. Charged particles fly through the space between shielding grids (Y = -40 mm) and the secondary electrodes plane (Y = 40 mm). In the figure, Z_p is the distance between the particle and the plane center in Z direction. (a) Z_p = 9.5 mm, (b) Z_p = 7 mm, (c) Z_p = 1 mm.

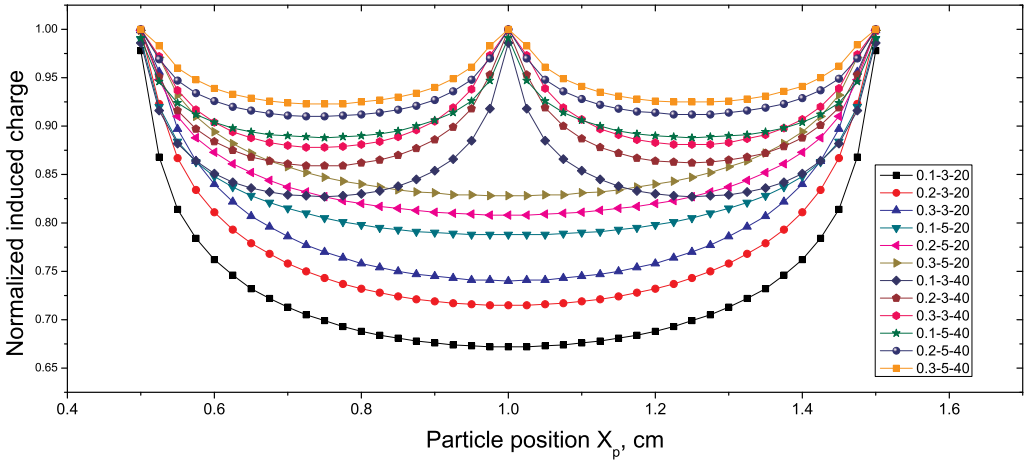

Fig. 2.4 Wire electrode geometries were tested for the wall effect. The labels like (0.1-3-20) are the wire plane parameters (d-D-N), where d is the wire diameter, D is the distance from the center plane to the first or third plane. X_p is the position of the particles. The wires are mounted at X_p = 0.5 cm and 1.5 cm for the case of N = 20; and at X_p = 0.5 cm, X_p = 1.0 cm and 1.5 cm for the case of N = 40.

electrode nearby the grounded side wall, a fraction of the image charge would lose the wall, which decreases the signal amplitude in the wire electrode.

Does the wire diameter play a role in terms of signal efficiency? Do thicker wires produce signals with higher amplitudes due to their larger surface areas? What is the recommended diameter of the wire electrodes? A thin wire would lose some induced charge and it is also more prone to mechanical damage. However, thicker wires decrease the overall optical transmission of the system and a trade-off has to be made. A study was performed investigating the efficiency of an electrode with individual wire thickness for the case when a charged particle passes two parallel wires under normal incidence.

Figure 2.4 shows the simulation results of the wall effect using different geometry designs of DTS-like electrodes. The wire thickness d was selected as of 0.1 mm, 0.2 mm and 0.3 mm. The spacing between the wires D_x was either 10 mm and 20 mm, respectively. The distances between the wire planes D_y was 30 mm and 50 mm. In total, there were 20 or 40 wire electrodes with an equal length of 200 mm covering a sensitive area of 200×200 mm^2. Here, the integrated induced charge of all the 20 or 40 electrodes in a plane was studied. If wires are used in a DTS-like configuration, the recommended distance between the wires is 5 mm and the wire thickness shall be 0.2 mm. According to the results, the maximum uncertainty to measure the particle charge in such a DTS-like system is approximately 40%, even without adding any noise to the signals.

Table 2.1 Wire plane parameters and related transmission.

d_w,mm	D_x,cm	D_y,cm	T, %	T_4, %	T_{total}, %	Accuracy$_Q$, %
0.1	3	2	0.99	0.96	90	33
0.2	3	2	0.98	0.92	86	26
0.3	3	2	0.97	0.88	83	24
0.1	5	2	0.99	0.96	90	19
0.2	5	2	0.98	0.92	86	18
0.3	5	2	0.97	0.88	83	16
0.1	3	1	0.98	0.92	86	16
0.2	3	1	0.96	0.85	80	12
0.3	3	1	0.94	0.78	73	11
0.1	5	1	0.98	0.92	86	10
0.2	5	1	0.96	0.85	80	8
0.3	5	1	0.94	0.78	73	8

Table 2.1 shows the possible transmission of particles through the DST-like detector. In the table, T is the transmission of a single wire electrode plane, T_4 is the transmission of the combined 4 electrode planes, and T_{total} gives the transmission of the total detection stage with two additional shielding grids (with 3×3 mm^2 mesh, 0.1 mm wire width and 95% open area) before and after the electrode planes. In the table, d_w is the wire width, D_x is the spacing between each electrode in a single plane and D_y is the distance between the two nearby planes as shown in Figure 2.4.

Based on our simulation results, there are three possible methods to increase the induced charge on the electrodes and to optimize the accuracy in particle charge detection: (1) One effective way is to decrease the spacing between the electrodes in a single plane. According to the simulation results, for decreasing the spacing of wire electrodes from 20 mm distance to 10 mm, the total integrated induced charge increases more than 10%. However, this method to increase the number of electrodes limit the total open area. On the other hand, decreasing the distances will increase the capacitance of the electrodes and therefore will add more noise to the CSAs. (2) Another possible method is to use thicker wires to get additional 5% to 10% of the induced charge. Using thicker wires can also benefit the mechanical stability for hyper-velocity impacts (as shown in Figure 2.18, 2.19 and 2.20). But this method will decrease the transmission and increases the noise by a higher capacitance. (3) The third method is to extend the distances between each plane of the electrodes. Unfortunately, this method will decrease the field of view of the detector and

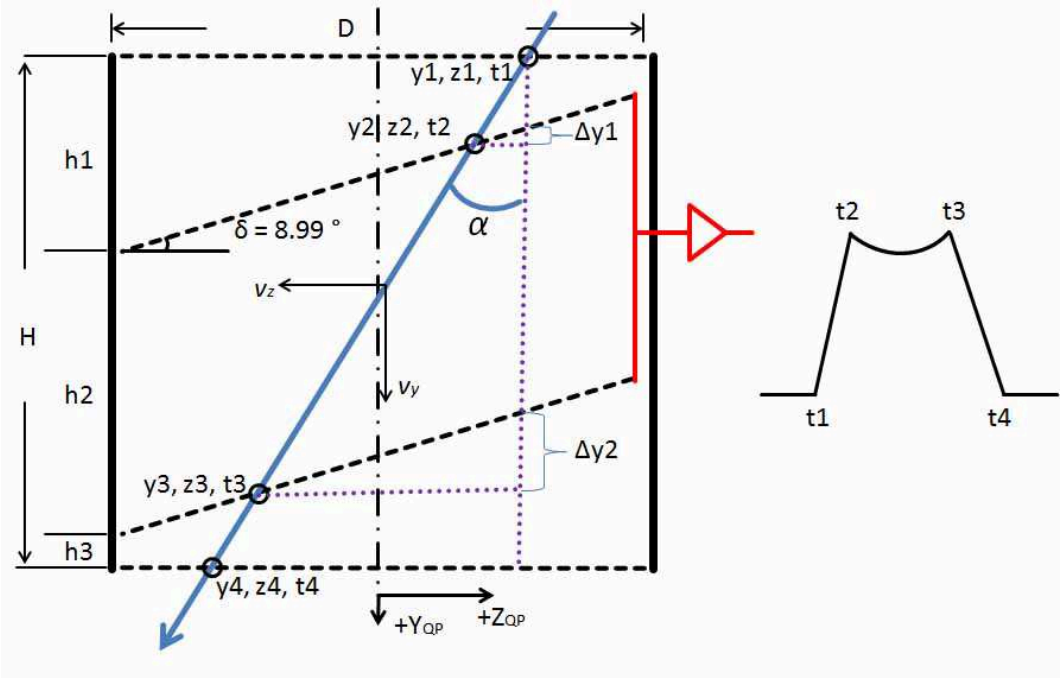

Fig. 2.5 Sketch and schematic cross-section of the CDA QP subsystem. The diameter of the detector is $D = 410.5$ mm, and the distance between the two gird electrodes $h2$ is 99.6 mm. In the design, $h1 = 15.9$ mm and $h3 = 80.6$ mm, which are the minimum and maximum distance between the shielding grid planes and the signal electrodes, respectively [9].

will increase the instrument mass and volume requirements.

2.2 Double Grids Electrode Sensor - CDA

The Cosmic Dust Analyser (CDA) onboard the Cassini spacecraft includes a charge sensitive entrance grid system (QP detector). The QP detector has two shielding grids (front and rear) and two connected parallel grids, which are tilted by an angle of 9 degrees with respect to the front plane (first shielding grid) of the detector. While entering the instrument, sufficiently charged particles induce characteristic image charge on the girds, which allows a reliable determination of the particle charge Q_d as well as the particle speed v_d. The dimensions of the QP detector is shown in Figure 2.5.

Basic trigonometric relations lead to the following formula calculated based on the sketch of Figure 2.5:

$$v_y = \frac{H}{t_4 - t_1} \tag{2.1}$$

$$v_z = (\frac{H}{t_4 - t_1} - \frac{h_2}{t_3 - t_2})\frac{D}{h_3 - h_1} \tag{2.2}$$

$$tan\alpha = \frac{v_y}{v_z} \tag{2.3}$$

The CDA instrument has the capability to determine the electrical charge of incident dust with a sensitivity approximately 1 fC. Auer et al. [9] reported some experimental results of oscilloscope signals of CDA tested at the dust accelerator, as shown in the left hand side of Figure 2.6. Between 1 AU and 2.1 AU heliocentric distance CDA registered six impacts showing a clear charge signal of interplanetary dust particles (IDPs), which are shown on the right hand side of Figure 2.6. This was the first unambiguous detection of electrostatic charges carried by dust particles in interplanetary space, and a detailed description can be found in the report by Kempf et al. [52]. The dust charge varied between 1.3 fC and 5.4 fC corresponding to particle masses between 1.3×10^{-13} kg and 9.5×10^{-13} kg. A reliable grain mass determination was derived under the assumption of a grain surface potential of +5 V. The particle properties are in agreement with the interplanetary dust model predictions and the grain speeds are close to the predicted values of circular Kepler velocities of micrometeoroides at the Cassini location during the time of detection. The detector has a very higher accuracy for trajectories at lower speeds and highly charged grains. However, the uncertainties of the grid crossing times are huge to determine the trajectory angle α from Equation 2.3, using the 6 MHz sampling rate and with additional signal noise during the operations in space.

In this study, a simulation model is developed using the COULOMB software to obtain further details on the particle trajectory and velocity measurements using CDA. The signals are continuously sampled at 6 MHz in order to obtain a high time resolution. If the charged particle passes through the QP detector with a velocity of 6 km·s^{-1}, in total 197 sampling points are recorded theoretically. For the simulations a 20 μm grain with a positive charge of 1 fC was moved through the detector using different trajectories. The double girds electrode, the shielding grids and the detector wall are electrically grounded. The relevant physical parameter for CDA is the integrated charge induced in the two sensing grids. This procedure was repeated with the location of the charge grains being stepped through an entire trajectory parallel to the detector axis, and then repeated for the trajectories at different distances to the detector wall. The different results for position changes in Z direction are shown in Figure 2.8. Figure 2.9 shows the results for particle trajectory changes. For the particles with different entry positions and trajectory changes in Z direction, the passing times of

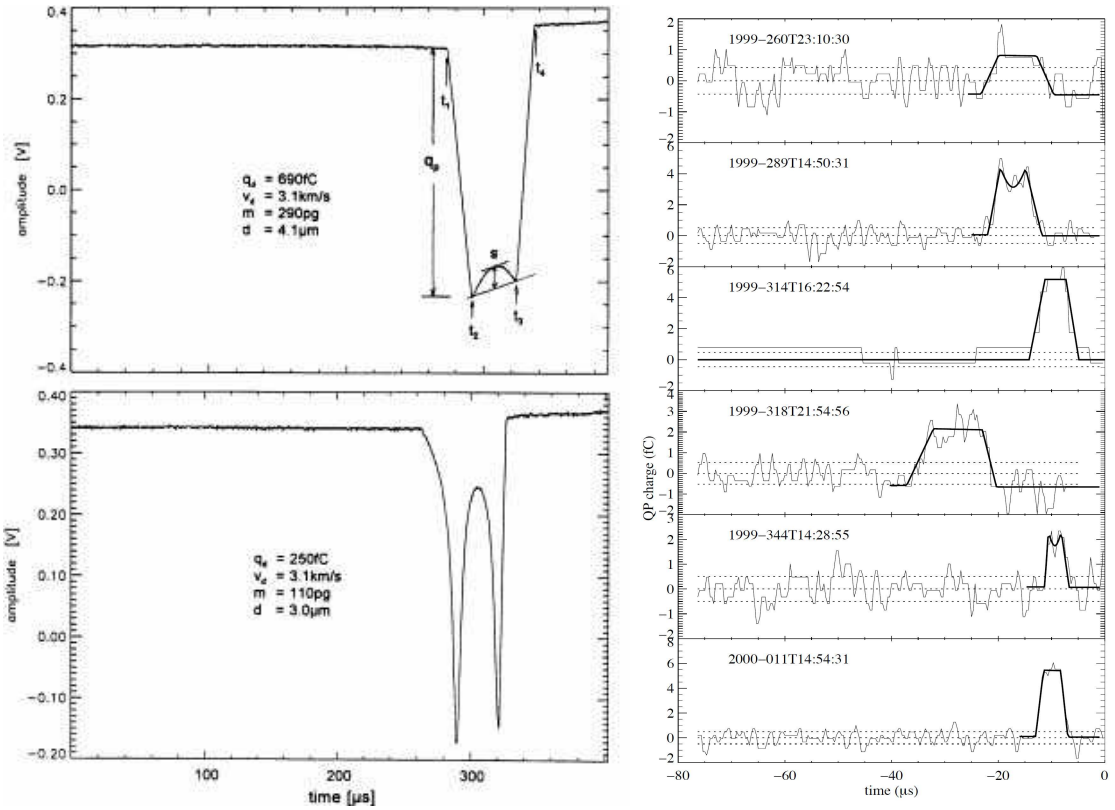

Fig. 2.6 Measurement signals of the CDA entrance grid channel. The left side shows two oscilloscope signals from a test grain at the dust accelerator. The top view was produced by a grain flying near the center of the detector. The bottom shows a trace nearby the the wall. The difference in sag is caused by a wall effect, and which will be discussed later. The right hand side shows the measurement signals of the CDA entrance grid channel (Qp) of IDPs carrying electrostatic charges between 1.3 and 5.4 fC, recorded during the interplanetary cruise in 1999 and 2000 between Earth and Jupiter. The reconstructed charge features are indicated by thick lines by Kempf et al. [52]. The impact speeds of the detected dust grains are 15 km·s^{-1}, 21 km·s^{-1}, 34 km·s^{-1}, 13 km·s^{-1}, 45 km·s^{-1}, and 34 km· s^{-1} from top to bottom[52].

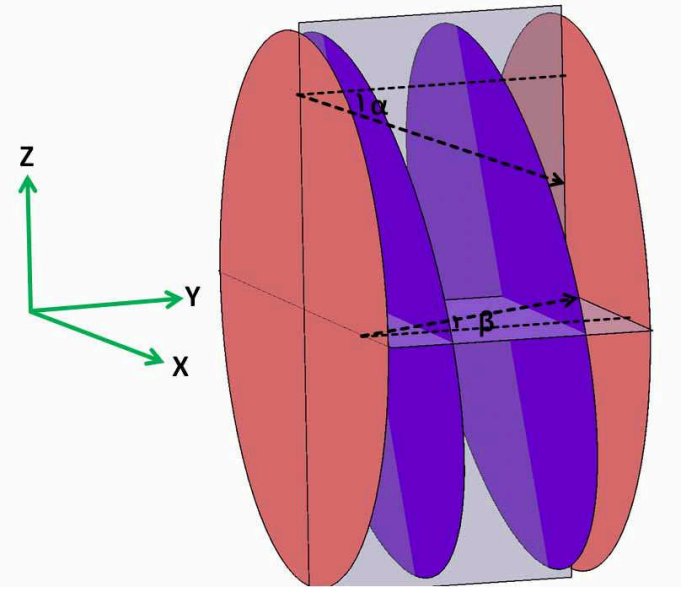

Fig. 2.7 Simulation model set up of QP detector in the CDA sensor. All tests were carried out in the center planes of X=0 and Z=0. The trajectory component angles in X and Z direction are called α and β, respectively.

Table 2.2 Particle charge, speed and trajectory accuracies based on simulated induced charge signals (simulated) for the QP detector. A_Q is the charge accuracy; A_{Vz} is the speed accuracy in speed vector Vz and A_α is trajectory accuracy. This table gives different velocity components Vy using a signal digitization clock speed of 6 MHz.

Vy, km $\cdot$ s^{-1}	N	A_Q, %	A_{Vz}, %	A_α, degree
3	393	2	0.6	0.35
6	197	3	3.7	2.2
12	99	5	16.6	9.5
24	50	7	22.5	16.7

the grid electrodes are different. Meanwhile, there is always a sag appearing between the two electrodes caused by the shielding wall, and its value and position also change with trajectory parameters.

All of the simulation results here assume an average particle speed of 6 km·s^{-1}. However, the relative velocities between cosmic dust particle and the CDA detector are normally larger than 10 km·s^{-1}, which means, that the number of sampling points will be less than 197 as used in the simulation process. Table 2.2 shows 4 different velocity components (Vy). The accuracy of the particle trajectory would be as low as 16.7 degrees, if the speed component Vy is lager than 24 km·s^{-1}. N is the number of sampling points from the first shielding grid to the second grid plane.

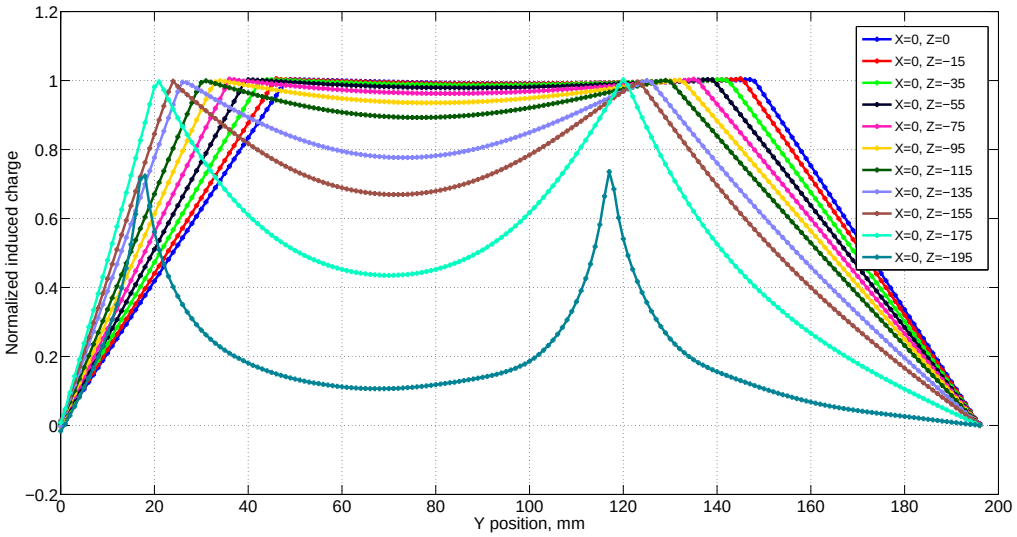

Fig. 2.8 Induced charge signals of the QP detector with particle entry position changes in Z direction. All entry points were selected in the center plane ($X = 0$) with trajectory angles $\alpha = \beta = 0$. X and Z show the entry positions of the first shielding plane.

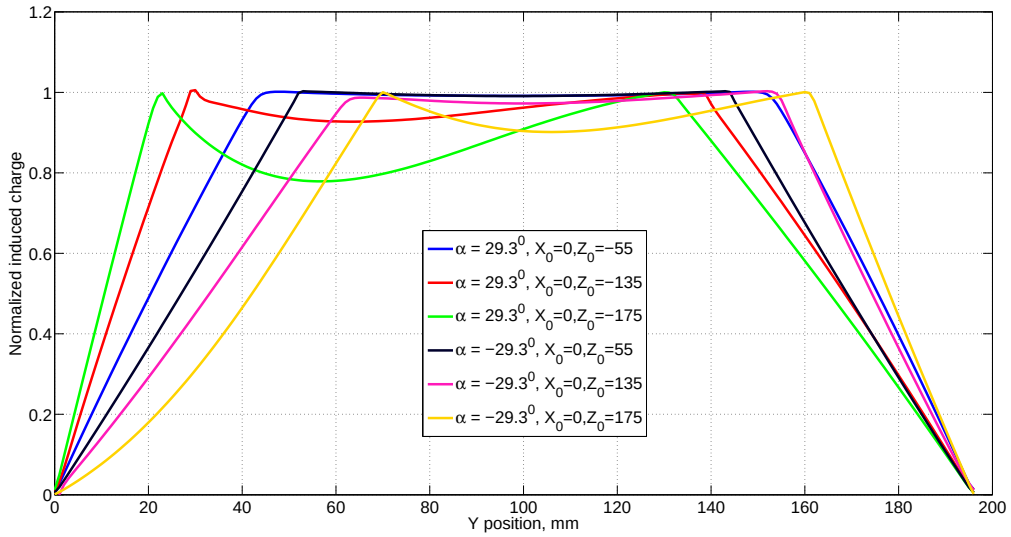

Fig. 2.9 Induced charge signals of the QP detector with particle trajectory (α) changes. All of the entry points where selected in the center plane ($X = 0$). Positive and negative α angles are compared here with different entry positions (Z_0) in the first shielding plane.

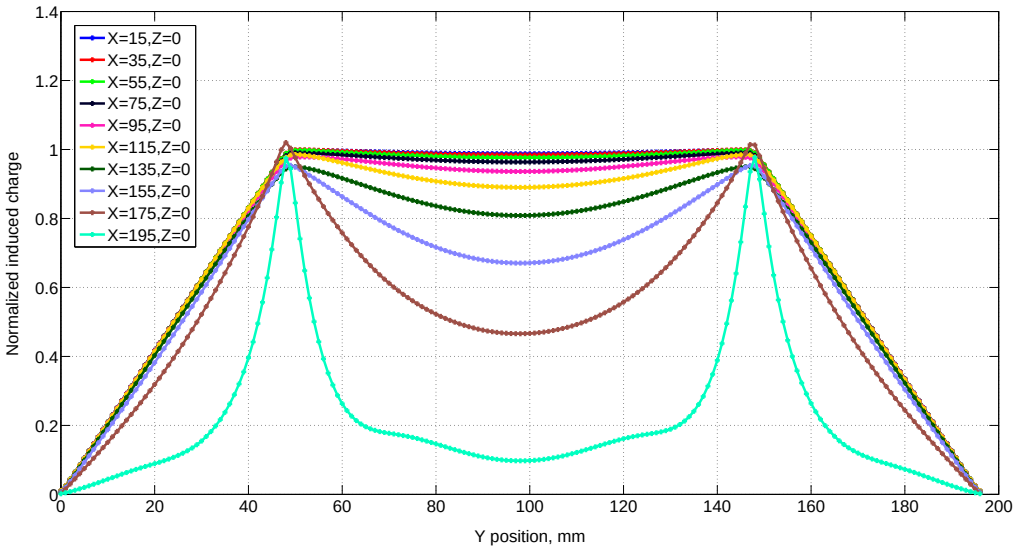

Fig. 2.10 Induced charge signals of the QP detector for particle entry position changes in X direction. The trajectory angle β is 0 and the position parameter $Z = Z_0 = 0$.

Figure 2.10 shows the results for different entry positions in X direction. From the results, although the sags have the same positions, the amplitudes of the sags vary with entry positions. Figure 2.11 shows some results of simulations with different particle trajectories (variable β). The differences of the sag pattern contain the information of the particle trajectory. However, as shown in Figure 2.6, an exact signal reconstruction including the shape of the sag is difficult for in-flight data due to the low signal-to-noise ratio.

The differences in the sag shape are caused by the image charges induced on the wall areas. The wall effect increases with the relative distance of the particle to the gird electrode and to the shielding wall, which is most significant when a particle is in the middle between the two electrodes. Figure 2.12 shows the summarized results of all features of the sags in Figure 2.10 and Figure 2.11. The amplitudes of sags are in good agreement with the experimental results from Auer et al. [9]. In the center of the QP structure, the sag value is approximately equal to the particle primary charge. Because of the wall effect cased by the shielding walls in the edge area structure, the induced charge on the QP structure is less than 10% of the particle primary charge.

The QP detector is sensitive to dust charges above 1 fC. Smaller charges are hidden in the amplifier noise or in interference patterns. Auer et al. [9] suggests that interference can be reduced by shielding and filtering. Especially the means of a low capacitance between detector and signal ground will decrease the amplifier noise. An advanced shielding concept

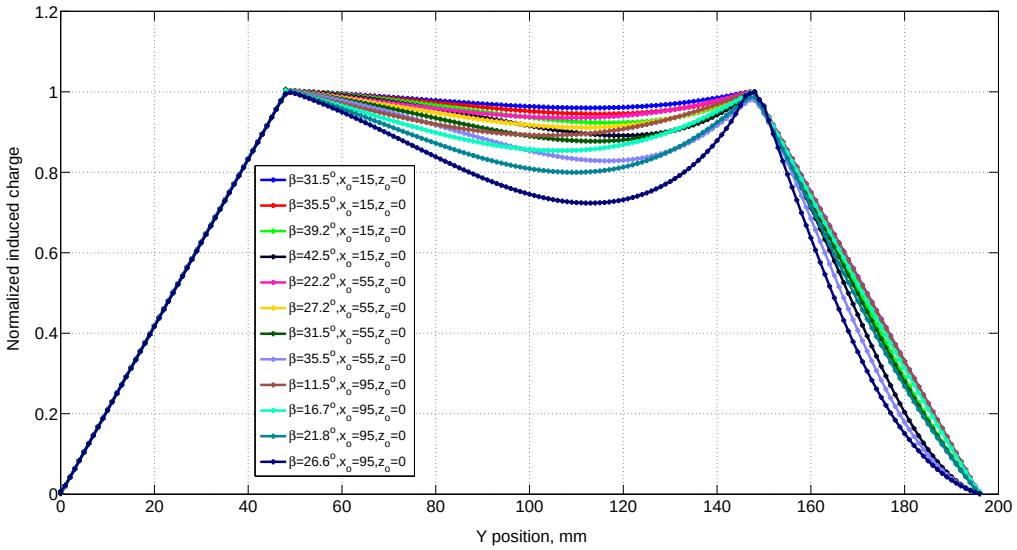

Fig. 2.11 Induced charge signals of QP detector for particle trajectory changes in angle (β) and entry positions in X direction. The position component $Z = Z_0 = 0$ in Z direction, and three entry position $X_0 = 15$ mm, 55 mm and 95 mm were selected from the center to the edge of the QP structure with various β in X direction.

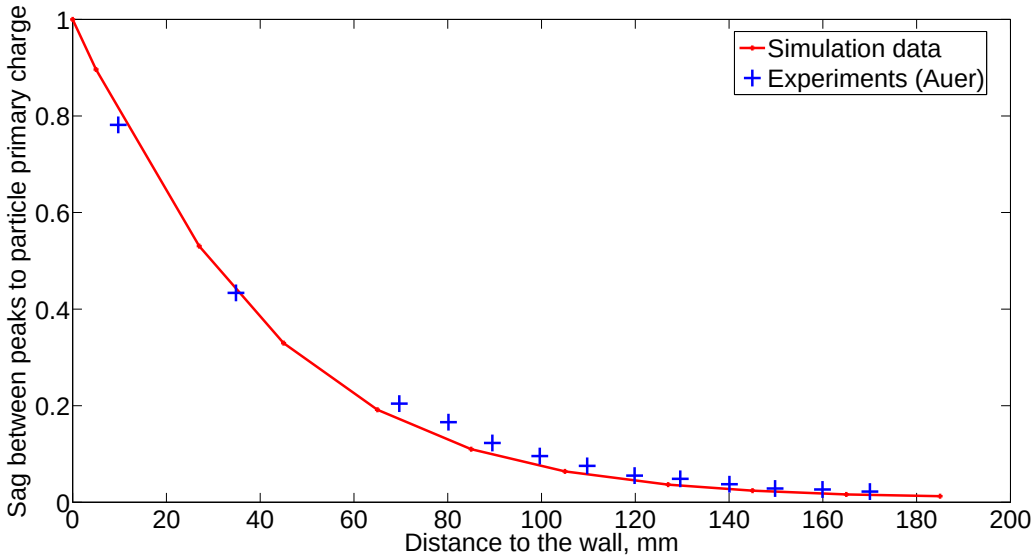

Fig. 2.12 The relationship between sag and the distance from particle to the wall. The sag is defined as the minimum value between the two peaks of the induced charge signal. The red line is the fit curve of simulation results and the blue '+' points are the results taken from Auer's experiment [9].

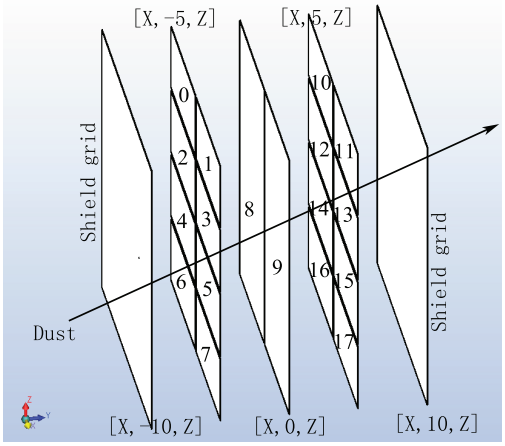

Fig. 2.13 The design of grid electrodes array sensor with labeled segment numbers.

of a new detector designed for the beam control of the dust accelerator was recently taken into operation. This system shows a much lower capacitance of only 9 pF (versus the CDA's 220 pF) and a noise as low as 0.15 fC. Such a detection system is suited to measure particle masses down to 10^{-15} g (with 0.05 μm in diameter) [74].

2.3 Grid Electrode Array Sensor

The third design of a dust trajectory sensor studied in this work employs a grid electrode array. Each of the grid electrode connects to a single charge sensitive amplifier to detect the induced charge of a dust particle. The three planes have 18 electrodes in total (see Figure 2.13). The total size of the instrument is about 25 $\times$ 21 $\times$ 21 cm^3 with an open area of approximately 400 cm^2. The particle trajectory detection is performed by the 16 electrodes of the planes labeled A and B. The sizes of the segments on Plane A and B are approximately 10 cm $\times$ 5 cm. The distance between two nearby segments is 3 mm in order to allow for a mountain structure and low capacitances of electrodes.

When a charged particle flies through an array of grid electrodes, two types of induced charge signals are created with one maximum or two maxima, respectively. Figure 2.14 shows the simulation results of induced charges of electrode for different insertion points in Z direction (Za = 0.5 cm for Figure 2.14 (a) and Figure 2.14 (b), and Za = 2.5 cm for Figure 2.14 (c) and Figure 2.14 (d)). The incident angles α are 0 degree for Figure 2.14 (a) and Figure 2.14 (c), and 14 degrees for Figure 2.14 (b) and Figure 2.14 (d). The signals

of the directly crossed segments 3 and 13 have only one maximum and lead to amplitudes of 100% of the particles primary charge. In the following discussion they will be called "Main Segment". Since the maximum values and the peak positions of the signals remain unchanged on these main segments, they can be used to determine the charge and velocity of the particle.

Another type of signals have two maxima which appear on segments 5, 11 and 15. They are the closest segments to the insertion points on the main segments and are called "Neighbor Segment". When the distance Za changes from 0.5 cm to 2.5 cm, the two maxima on segment 5 decrease from 0.2 to 0.05. The two maxima of neighbor segments show opposite change with the particle incident angle. Therefore, the signals recorded by neighbor segments can be used to analyze the trajectory information of charged particles.

Considering the scientific measurement requirements (dust charge, speed and trajectory, etc.) and the payload limitations (low mass, low data volume and low power), in this study, we selected the design with grid electrode arrays to develop, build and test the laboratory model. More details of the grid electrode array sensor will be described in Chapter 3 and additional experimental signals are shown in Appendix B.

2.4 Electrode Geometry Analysis

2.4.1 Transmission

The induced charge signal recorded by an electrode depends on the relative area and the distance to the charged particle. When the charged particle approaches the grounded side wall, a fraction of the induced charge moves from the target electrode to the wall, which is called 'wall effect' in this study. The reduced induced charge is determined by the relative area of the wall to the electrodes. The diameter and distance of wire electrode influence the wall effect, as well as the transmission of the electrode array. For the design employing grid electrodes, the directly related parameters are the diameter of the mesh wire and the mesh width.

Figure 2.15 shows the parameters for the calculation of the transmission of grid electrodes and the wire electrodes designs. In this figure, $D1$ and $D2$ are the width and length of a single mesh in grid electrode. For the design with wire electrodes, $D1$ is the distance between two wires and $D2$ is the length of the wires. d is the width of the wire (or mesh line of the grid) and M is the width of the open area for both wire and grid electrodes.

For a quantitative investigation of the described wall effect caused by a grounded

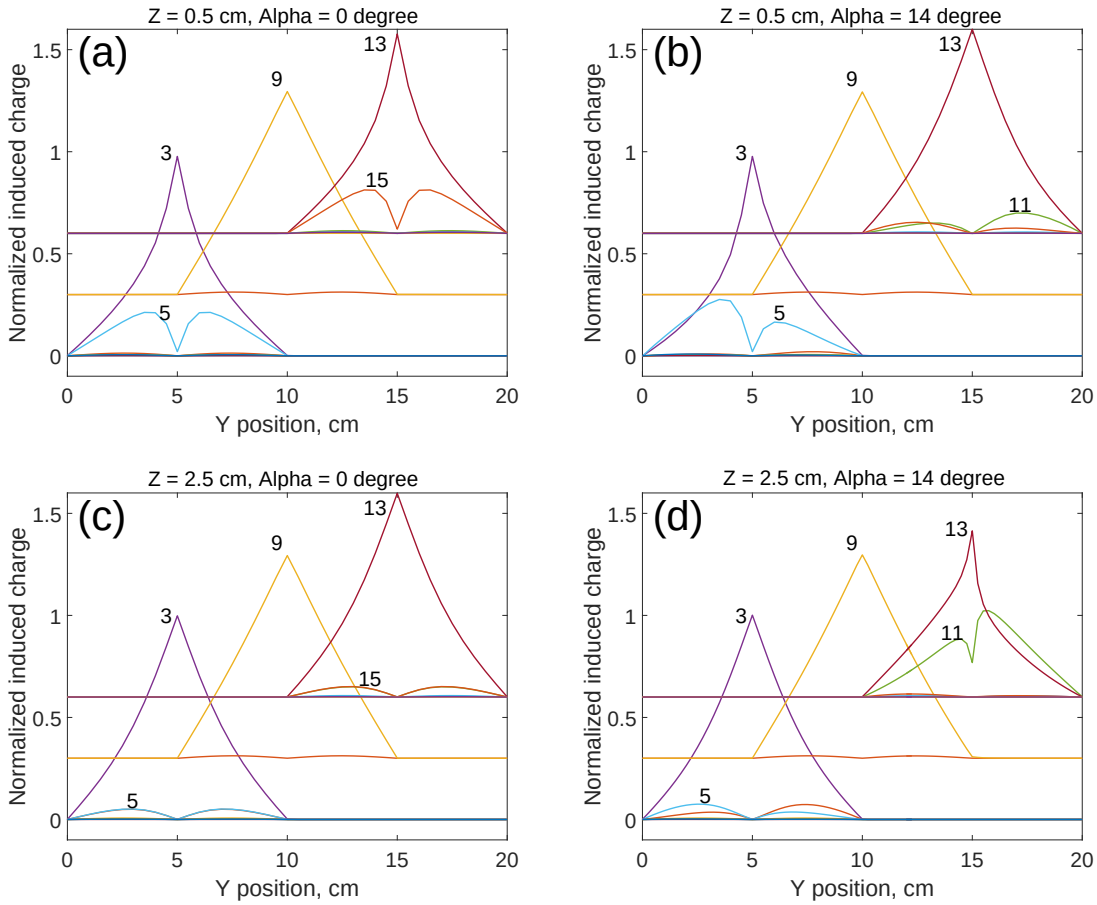

Fig. 2.14 Induced charge signals on the segments for particles with different incident angles and insertion positions. Figures (a) and (b) show the results for an insertion point in the edge of segment 3 (nearby segment 5), and (c) and (d) give the results for an insertion point in the middle of segment 3. The values labeled close to the data curves are the segment numbers (Figure 2.13). *Z* is the minimal distance from the insertion points to the bottom edge of segment 3 in Z direction. The particles fly through segments 3, 9 and 13 with a relatively large signal on the nearby segments 5, 11 and 15. For a quantitative analysis small amplitudes below a normalized value of 0.05 are ignored.

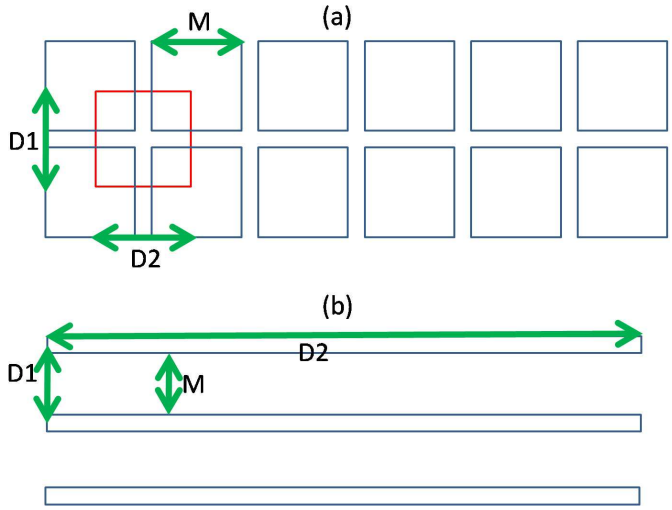

Fig. 2.15 Transmission (T) calculations for grid and wire electrodes. For grid: the $T = M^2/(D1 \times D2)$, for wires: $T = M/D1$, where, $M = D1$ - W.

housing, we do consider a simple electrode design using the COULOMB software. We built up a small sized (2.4×2.4 cm^2) grid electrode, with different mesh widths D and mesh wire diameters d. The gird was located in the center of a $10 \times 5 \times 10$ cm^3 grounded box, as shown in Figure 2.16. The simulation results of the induced charges in the grid electrode are shown in Figure 2.17. Here, the charged particle flies through the mesh electrode at its edge. According to our simulation results, the geometry design of the grid electrode, such as its mesh size and the diameter of its mesh wire, influences the final wall effect. The grid with mesh length of 1 mm and wire width of 0.05 mm has an open area of 90% and induced charge measurement accuracy is better than 8%, which meets the requirement for a dust trajectory sensor design.

The transmission significantly affects the applicability of a dust trajectory sensor with a wire electrode array or a grid electrode array. An useful trajectory signal is obtained only when the particle passes through all of the wire or grid electrodes combined with one or more shielding grids. The final transmission has an exponential relationship with the transmission of a single plane. For example, if we use girds with a mesh width D = 1 mm and with a diameter of mesh wire d = 0.05 mm, the transmission of a single plane is 90%. The transmission of the sensor with 4 planes is obtained as:

$$T_n = T^n = 0.9^4 \times 100 = 66\% \tag{2.4}$$

where n is the total number of planes including shielding grids.

Table 2.3 shows the relationship between grid geometry design, transmission and the

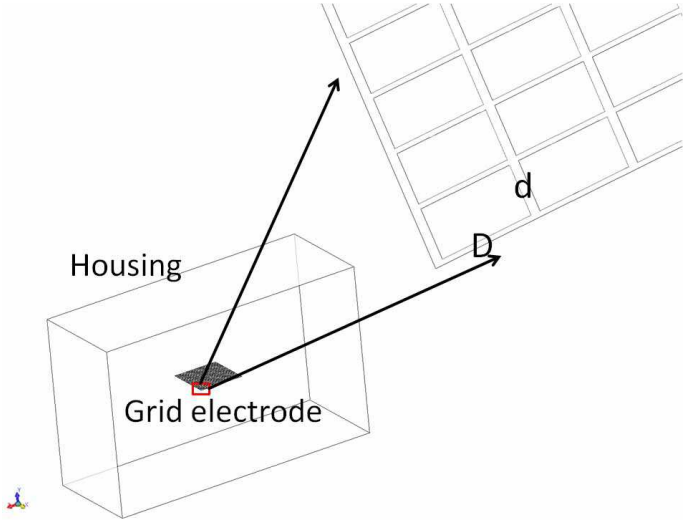

Fig. 2.16 Grid electrode used for wall effect test. The grid is in the center of a semi-infinite housing (10 cm $\times$ 5 cm $\times$ 10 cm). The mesh of the grid has a square shape, where D is the width of the mesh and d is the diameter of the mesh line. The diamond shape of grid mesh shown in the figure is cased by the perspective view.

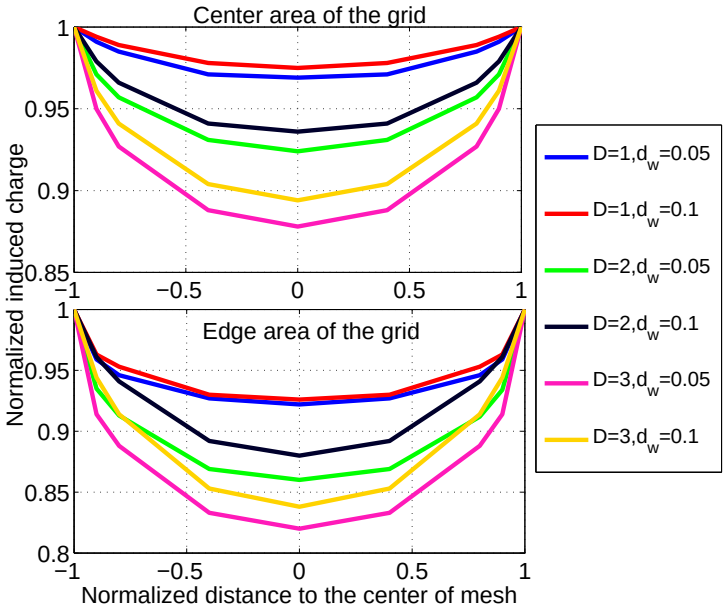

Fig. 2.17 Grid electrode geometries and test of the wall effect. 6 different geometry designs were simulated with different D and d. Nine different insertion positions from the center (Y = 0) to the mesh line ($Y = \pm$ 1 mm) were tested.

Table 2.3 Transmission and charge measurement accuracy A_Q for different grid geometries. D is the width of grid mesh, d is the diameter of grid mesh line, T is the transmission of a single grid, T_4 is the transmission of 4 planes, A_Q(center) and A_Q(edge) are the accuracy of the charge measurement based on simulation results when the particle passes through center and edge regions of the grid respectively.

D, mm	d, mm	T, %	T_4, %,	A_Q(center), %,	A_Q(edge), %
3	0.05	97	88	12	18
3	0.10	94	78	11	16
3	0.20	88	60	-	-
2	0.05	95	81	8	14
2	0.10	90	65	6	12
2	0.20	82	45	-	-
1	0.05	90	65	3	8
1	0.10	83	47	3	7
1	0.20	69	23	-	-

measurement accuracy A_Q of detected induced charges when a charged particle flies through the grid with a normal incident angle.

2.4.2 Mechanical Strength

The electrode array is one of the functional structures for a charge induction sensor. These metal wires or grids are explored to the hyper-velocity impact environment. The high speed particles are the measurement targets, and we wish all of them can pass through the electrode array. However, due to the limitation of the electrode geometry, some grains might impact on the electrode and cause damages. There are two types of hyper-velocity impacts which can destroy the electrodes: direct impacts and indirect impacts. Direct impacts are caused by interplanetary dust particles impact on the electrode directly. Indirect impacts are the secondary impacts caused by fragments created during impact events on detector the housing or on other exposed parts of the spacecraft. The large sized interplanetary dust particles and the secondary ejecta (above 100 μm) are rare on the lunar surface. In this study, we used three different micron-sized projectiles (10 μm, 50 μm and 100 μm) to bombard copper wires with speeds from 1 km·s^{-1} to 17 km·s^{-1}.

The Autodyn 14.0/2D software was used to simulate the damage of the electrode bombarded by different sized projectiles. The projectile and target models are both built up by the Lagrangian method. The targets have the length of 1600 μm with different widths of 50 μm, 100 μm and 200 μm. All material models used in the numerical analysis were

taken from the Autodyn material database. The CONC-35MPA and COPPER material models were chosen to simulate the projectiles and targets, respectively. All parameters of the material models used in the simulation are shown in Appendix B.

Figure 2.18, Figure 2.19 and Figure 2.20 show the simulation results for different sized dust particles impacting on copper wires with diameters of 0.05 mm, 0.1 mm and 0.2 mm. Based on our simulation results, for the wire electrode designs we suggest to use thicker wires (0.2 mm or 0.3 mm in width), which can survive in the most hyper-velocity impact cases. The wire electrodes with thickness as lager than 0.3 mm might reduce the total transmission. In contrast, for the design with grid electrodes, we do suggest to use smaller values of mesh widths and mesh line diameters (D = 1 mm and d = 0.05 mm), since the electrodes still function even if some parts of individual grid electrodes are cut by impact events.

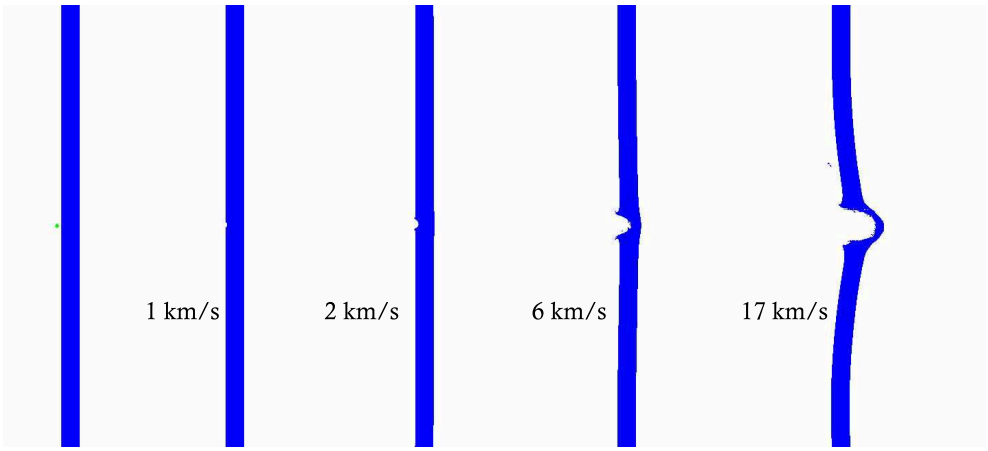

(a) Particle diameter D = 10 μm, target wire width is 50 μm.

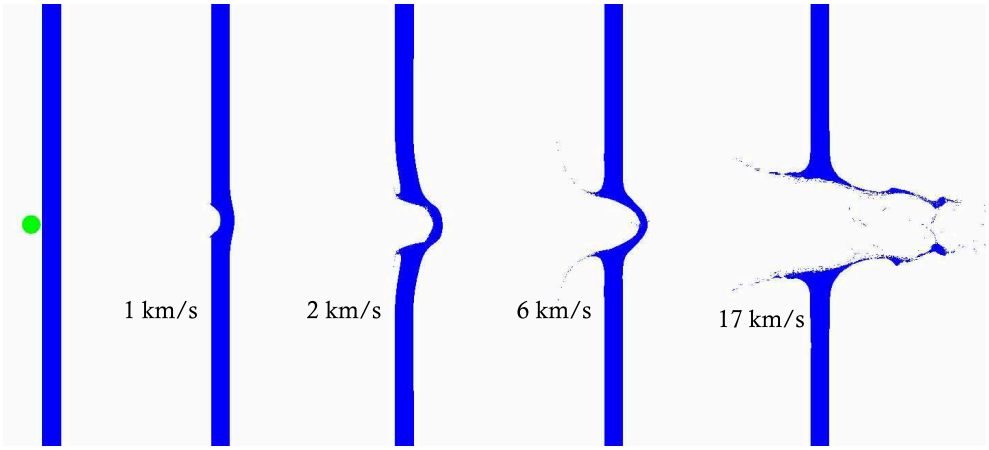

(b) Particle diameter D = 50 μm, target wire width is 50 μm.

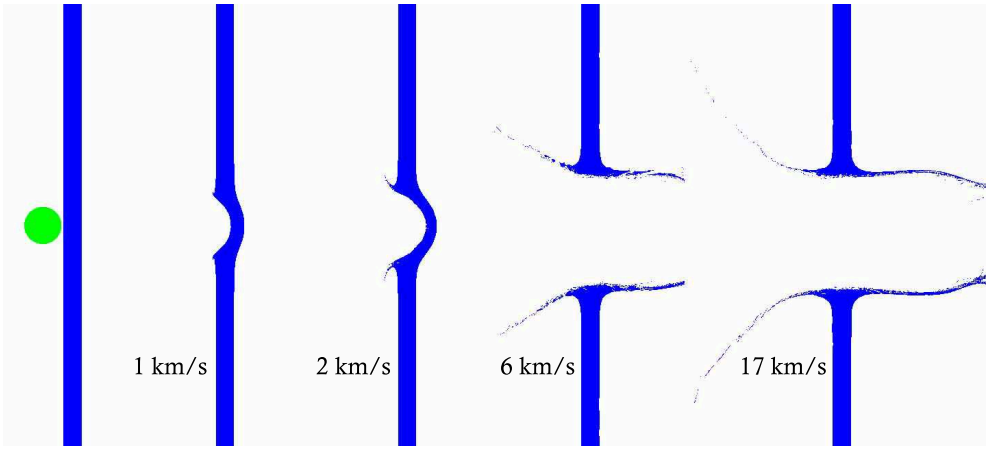

(c) Particle diameter D = 100 μm, target wire width is 50 μm.

Fig. 2.18 Impact damage of the 50 μm thick wire for different impact conditions. The green circles are impact projectiles and the blue tubes are target wires. Damages of wires are created by projectiles with diameters of 10 μm, 50 μm, and 100 μm (from top to bottom); and with speeds of 1 km·s^{-1}, 2 km·s^{-1}, 6 km·s^{-1}, and 17 km·s^{-1} (from left to right).

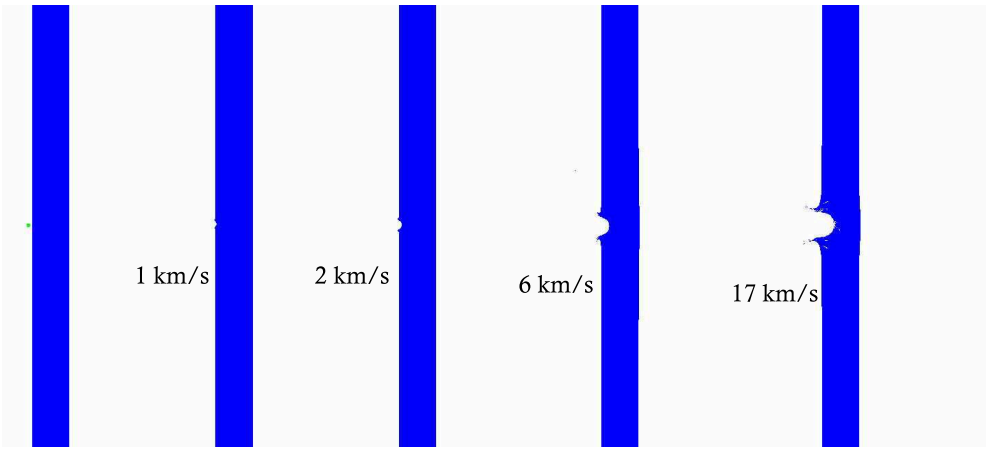

(a) Particle diameter D = 10 μm, target wire width is 100 μm.

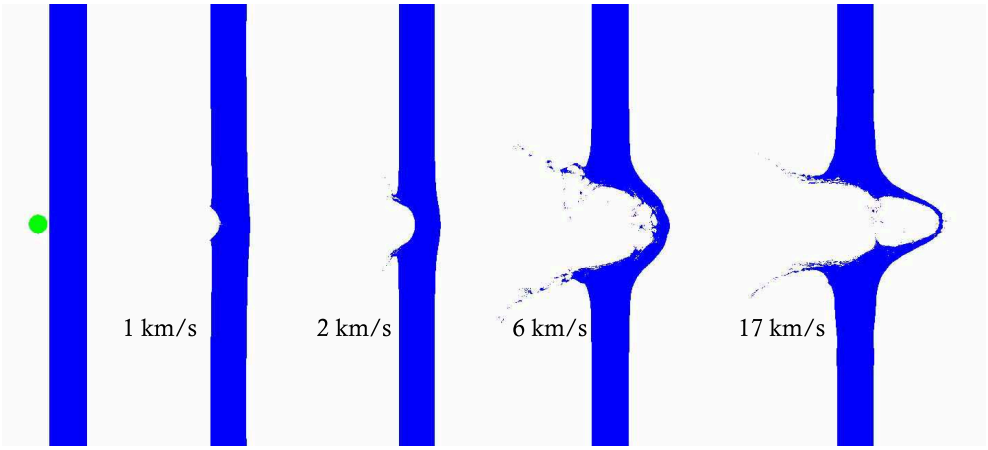

(b) Particle diameter D = 50 μm, target wire width is 100 μm.

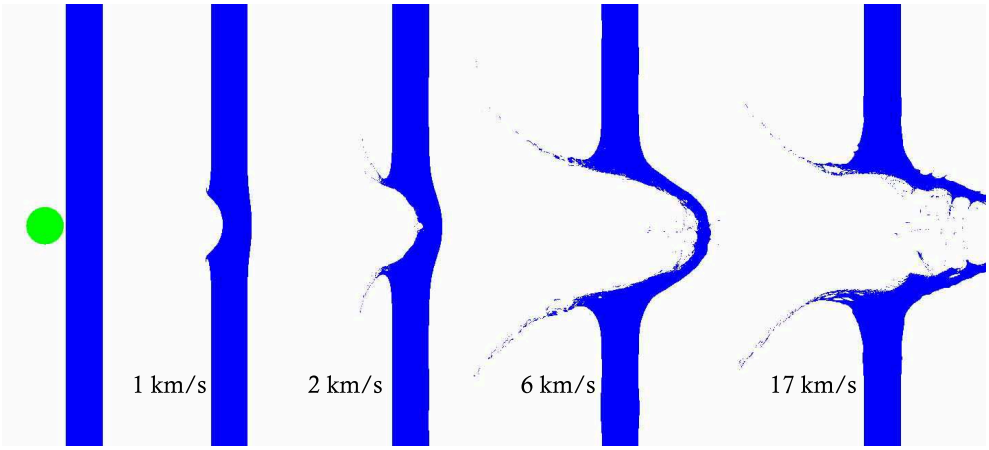

(c) Particle diameter D = 100 μm, target wire width is 100 μm.

Fig. 2.19 Impact damage of the 100 μm thick wire for different impact conditions. The green circles are impact projectiles and the blue tubes are target wires. Damages of wires are created by projectiles with diameters of 10 μm, 50 μm, and 100 μm (from top to bottom); and with speeds of 1 km·s^{-1}, 2 km·s^{-1}, 6 km·s^{-1}, and 17 km·s^{-1} (from left to right).

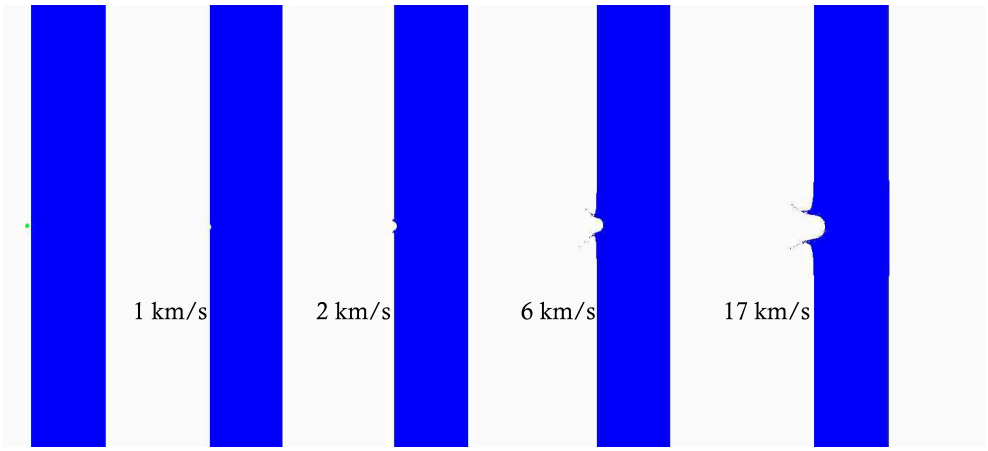

(a) Particle diameter D = 10 μm, target wire width is 200 μm.

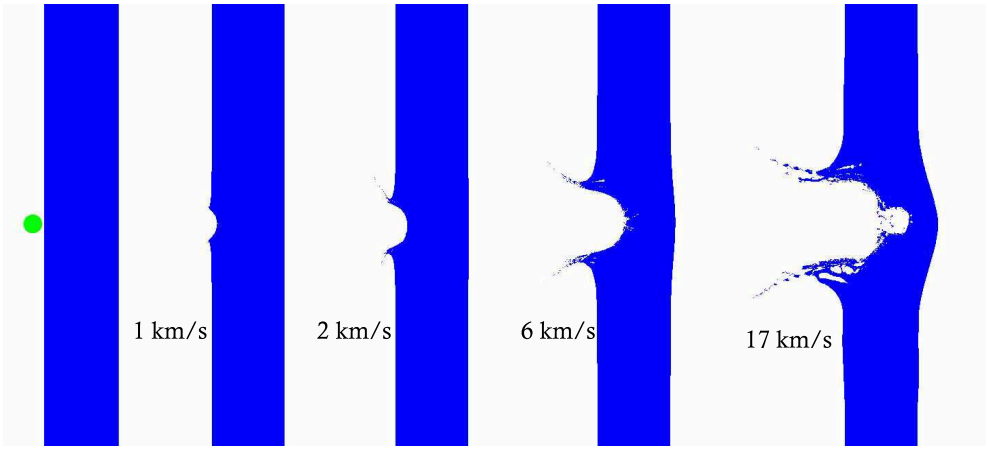

(b) Particle diameter D = 50 μm, target wire width is 200 μm.

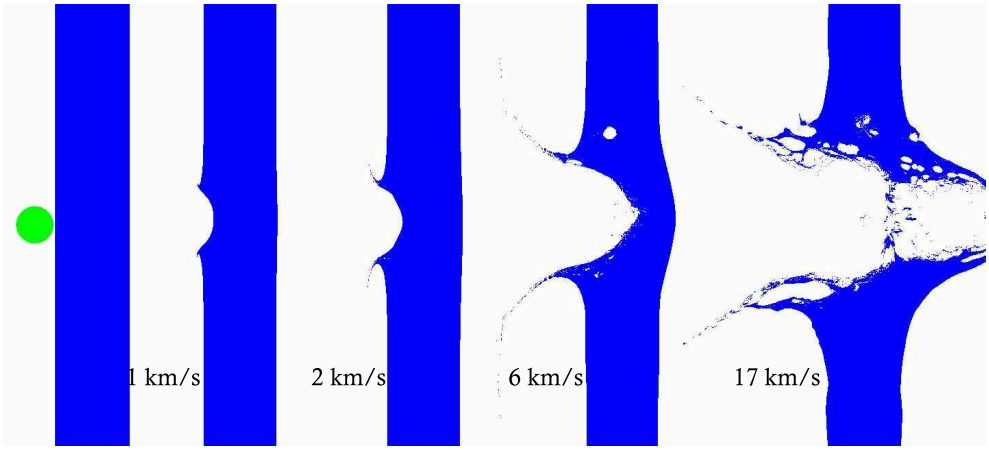

(c) Particle diameter D = 100 μm, target wire width is 200 μm.

Fig. 2.20 Impact damage of the 200 μm thick wire for different impact conditions. The green circles are impact projectiles and the blue tubes are target wires. Damages of wires are created by projectiles with diameters of 10 μm, 50 μm, and 100 μm (from top to bottom); and with speeds of 1 km·s^{-1}, 2 km·s^{-1}, 6 km·s^{-1}, and 17 km·s^{-1} (from left to right).

Chapter 3

Lunar Dust eXplorer Concept

One of the highest-priority issues for a future human or robotic lunar exploration is the lunar dust. This problem should be studied in depth in order to develop an environment model for a future lunar exploration. A future ESA lunar lander mission requires the measurement of dust transport phenomena above the lunar surface. Here, we describe an instrument design concept to measure slow and fast moving charged lunar dust which is based on the charge induction method. The new dust detector should have a simpler design, and should be with lower mass and power comparing with the known Dust Trajectory Sensor (DTS). The predicted measurements using the new design should have a trajectory accuracy better than 5°, a speed accuracy of better than 20%, and a charge accuracy of better than 10%.

In this chapter, we present the details of the LDX laboratory model, which was tested at the dust accelerator located at the Max Plank Institute for Nuclear Physics. The experimental results and data analysis are described in this chapter as well.

3.1 Instrument Design

The Lunar Dust eXplorer (LDX) contains an electron reflector, three planes of charge sensitive electrodes and an impact ionization target. Each of the grid electrodes connects to a single amplifier, which works by detecting the induced charge of a dust particle. The three planes have in total 18 electrodes as shown in Figure 3.1. The total size of the instrument is about $25 \times 21 \times 21$ cm^3 with an open area of approximately 400 cm^2. The particle trajectory detection is performed by the 16 electrodes of the planes labeled A and B.

The segments on Plane A and B have a size of approximately 10 cm $\times$ 5 cm. The distance between the segments on each plane is 3 mm in order to allow for a mountain structure and a low capacitance between the electrodes. Each electrode of the laboratory

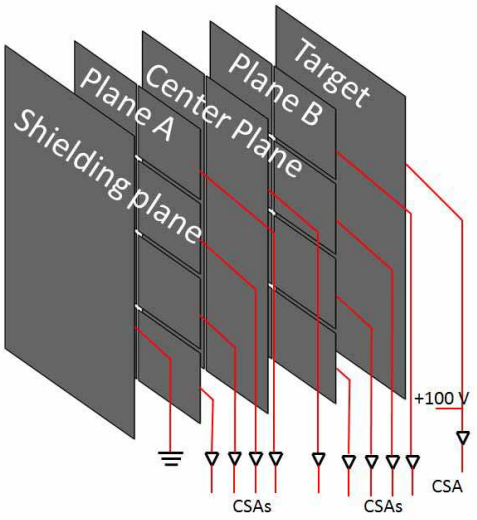

Fig. 3.1 Sketch of the LDX instrument. The main structure of the instrument includes an electron reflector (which is hidden here), and a shielding grid for the plasma protection of the trajectory sensor and the impact target.

model consists of a nickel alloy grid with the mesh width of about 1.5 mm and an open area of more than 90%.

For the detection of high speed particles (>1 km·s^{-1}), an impact ionization target is added behind the second shielding grid (Figure 3.1). The impact stage consists out of a grounded grid (shielding grid) and an impact plate (e.g. gold coated aluminum).The impact target connects to a single charge sensitive amplifier with a bias potential of +100 V. Fast impacts generate a plasma charge at the plate which can be used as a trigger signal, similar to the description of impact ionization detectors like Galileo, Heos or Cassini [6]. Slower particles are triggered by digital filters of the signals from the electrodes of the three planes.

For the exact mechanical dimensions of the grid mounting structure, special capacity considerations were necessary. The minimum noise of a designed CSA increases roughly in proportion with the capacitance of its connected detector [7, 23]. To reduce the measurement noise of a designed charge sensitive amplifier, a possible way is to reduce the extra capacitance as much as possible. The segmented electrodes need some support structure to be separated from each other and they are mounted at the main structure of the detector. The COULOMB simulations were used to calculate the capacitance of the grid mounting structure. The smaller sized grid electrodes (5×10 cm^2) have a capacitance of 7.6 pF, and the larger ones (10×20 cm^2) have a capacitance of 26.3 pF. If a conducting material is selected as mounting structure, the capacitance of smaller sized electrodes increases from 7.6 pF to 13.8 pF. As an alternative to metal material, nylon holding frames, produced

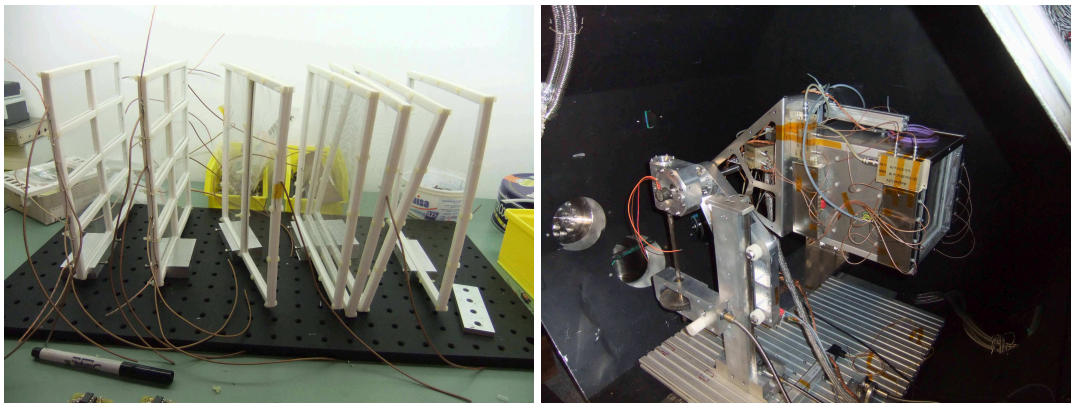

Fig. 3.2 Set up of the laboratory model at the dust accelerator. The platform has 3 degrees of freedom: (1) right $\leftrightarrow$ left, (2) up $\leftrightarrow$ down, and one angle in the vertical direction with respect to the accelerator beam line.

by a 3D printing technology were used for the laboratory model (as shown in left side of Figure 3.2).

During the calibration, the LDX laboratory model was mounted on a platform that provided articulation about the horizontal (Y)-axis and translation in X and Z in coincidence with the coordinate system used in the simulation process (see Figure 3.3). In each test orientation, more than 10 events were recorded by 3 Lecory digital storage oscilloscopes (Type Wavepro7000, HD4024 and HD6054).

3.2 Signal Simulations

3.2.1 LDX Model Parameters

The tested trajectories of particles with different incident angles in Z direction (left side of Figure 3.3, angle α) and X direction (right side of Figure 3.3, angle β). When particles fly through one insertion point on segment 3 with variable angles, they arrive at different positions on segment 13. All of the insertion points were chosen from the center area of the segment (following X or Z direction) to simplify the concurrent trajectory analysis process. The distance between each insertion point is 0.25 cm in Z direction and 1 cm in X direction, respectively. Up to 10 different incident angles were studied for each insertion point on segment 3. The ranges of incident angles for different insertion points on segment 3 varied between (0 - 16) and (0 - 25) degrees with an interval of about 3 degrees. The relationships between incident angles (α or β) and the insertion point positions ([Xa, Ya, Za] and [Xb, Yb, Zb]) on segment 3 and 13 are:

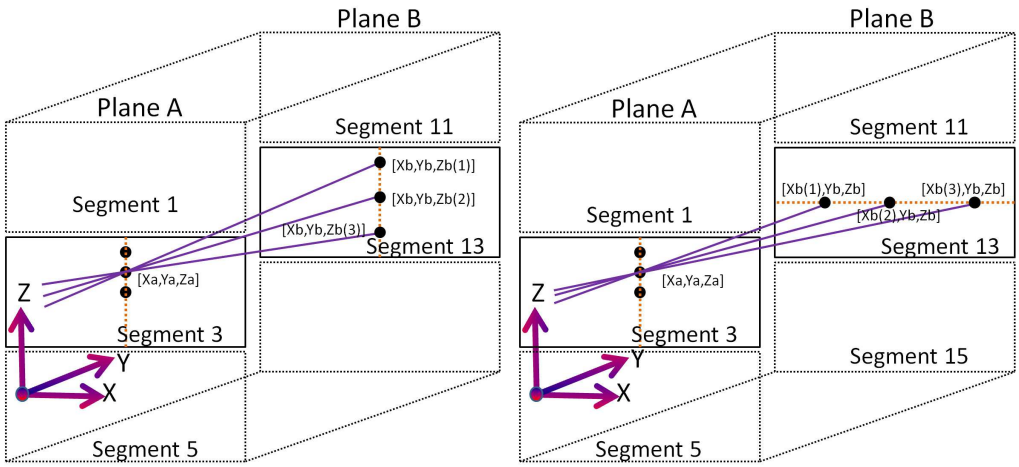

Fig. 3.3 Different scenarios for particle track geometries in Plane A and Plane B (half-model). The left part shows the incident angles changing in Z direction; the right part shows the incident angles changing in X direction. Xa or Xb are the distances from the insertion point to the left edges of segments 3 and 13; Za and Zb are the distances from the insertion points to the bottom edges of segments 3 and 13.

$$\alpha = arctan\frac{(Zb - Za)}{Yb - Ya} \tag{3.1}$$

$$\beta = arctan\frac{(Xb - Xa)}{Yb - Ya} \tag{3.2}$$

The parameter (Yb-Ya) describes the distance between Plane A and Plane B, which has a value of 10 cm for the LDX design.

3.2.2 Dust Trajectory Determination

In Chapter 2 we showed that the values of maxima on neighbor segments hide the information of particle insertion point position and particle trajectory. The average values of the two maxima are normalized to the particle primary charge, and it will be defined as amplitude Q_{alpha} in this study. Figure 3.4 shows the relationship between Q_{alpha} and the incident angle α for different insertion points. The value of Q_{alpha} decreases with Za. Meanwhile, there is a weak increase of Q_{alpha} with the incident angle α. The simplified relationship between particle trajectory parameter α and the position parameters Za and Xa (derived from the same process like Za) is shown in Figure 3.5, which ignored the weak difference on incident angle for the same insertion point. Equation 3.3 and 3.4 are the formulas to calculate the insertion point position (Xa, Za) derived from Figure 3.5. The

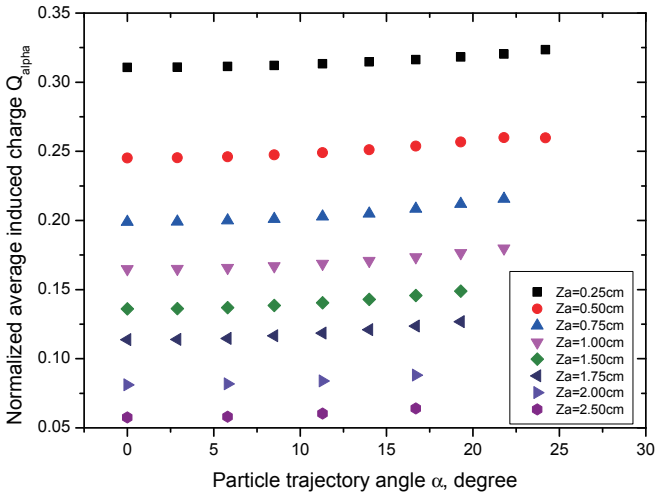

Fig. 3.4 The relationship between Q_{alpha} and particle incident angle α for different insertion points in Z direction (Za). The incident angles varies from 0° to +25° with up to 10 different angles for each insertion point with an interval of about 3 degrees. The maximum value of the incident angle of 25 degrees was selected to make sure that all insertion points on plane B are constrained to segment 13. As segment 3 has a symmetrical structure, only half of the distances Za are tested (Za = 0.25 - 2.5 cm) with an interval 0.25 cm.

deviation caused by the simplified signal processing and amplifier noise is discussed in section 3.2.3.

$$Za = 1.043 \times lg\frac{0.356}{(Q_{alpha} - 0.028)} \tag{3.3}$$

$$Xa = 0.934 \times lg\frac{0.340}{(Q_{beta} - 0.023)} \tag{3.4}$$

In our design, Plane B has the same geometrical structure as Plane A, therefore, the insertion point position (Xb, Zb) on Plane B is available using the same equations as for Plane A (Equation 3.3 and 3.4). After we get the two entry point positions on Plane A and Plane B, the tangent theorem can be used to find out the particle trajectory direction (Equation 3.1 and 3.2).

3.2.3 Detector Accuracies

The attained accuracy of the LDX instrument with the chosen geometry is limited by the noise of the charge sensitive amplifier (CSA), the electrode capacitances, the primary charge

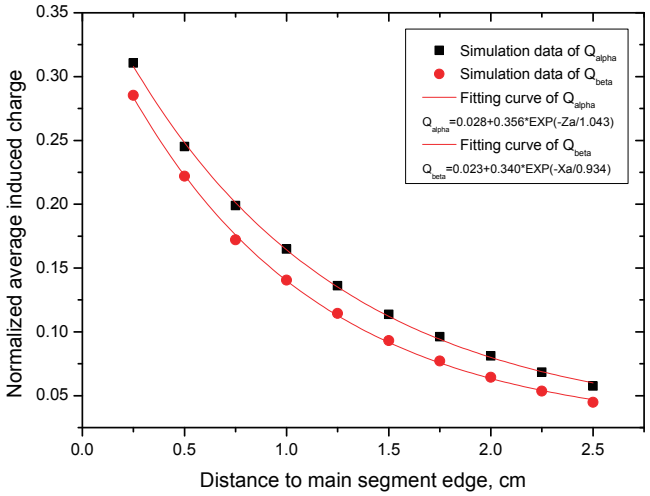

Fig. 3.5 Fitting curves for Q_{alpha} and Q_{beta} with particle position parameters Za and Xa. Q_{alpha} is the normalized average induced charge of obtained by the electrode on left or right side of the 'Main Segment', and Q_{beta} is the normalized average induced charge obtained by the electrode on top or down side of the 'Main Segment'.

of the dust particle itself and its velocity. As reported by Srama et al. [72], the root mean square (rms) noise level of CSA at a detector capacitance of 5 pF is 1.5×10^{-17} C (equal to 100 electrons) over a bandwidth of 10 kHz - 10 MHz. The CSA noise increases roughly in proportion with the detector capacitance [23]. As we calculated using the COULOMB software, the capacitance of each small electrode segment is about 7.6 pF. Hence the noise level of the grid electrodes should be similar with the results reported by Srama et al. [72], which is about 1.5×10^{-17} C. Xie et al. [87] described a method of analyzing the accuracy of trajectory measurements for a DTS-like detector. They found an accuracy for the determination of the incident angle of lower than 1° as long as the Charge to Noise Ratio (QNR) is larger than 10.

Sampling rate is another important parameter for the design of a dust trajectory detector. The dust trajectory depends on the number of sampling points when dust grain flies through the grid electrodes array. For our simulation study, 41 data points (assumed particle speed is 5 km/s and CSA working bandwidth is 1 MHz) contributed for each electrode plane crossing (from the first shielding grid to the second shielding grid, 20 cm) in our studies. The dust charge is normalized and white noise with normal (Gaussian) distribution was added to the signal. The parametric study is performed for three different QNR values (10, 20 and 100). Figure 3.6 and Figure 3.7 show the scatter of $\triangle$Za and the accuracy of α for different insertion positions and QNR values. The measurement accuracy of the angle α in most cases stays within $\pm 2^{\circ}$. However, when Za becomes larger than 2 cm (in the center regions

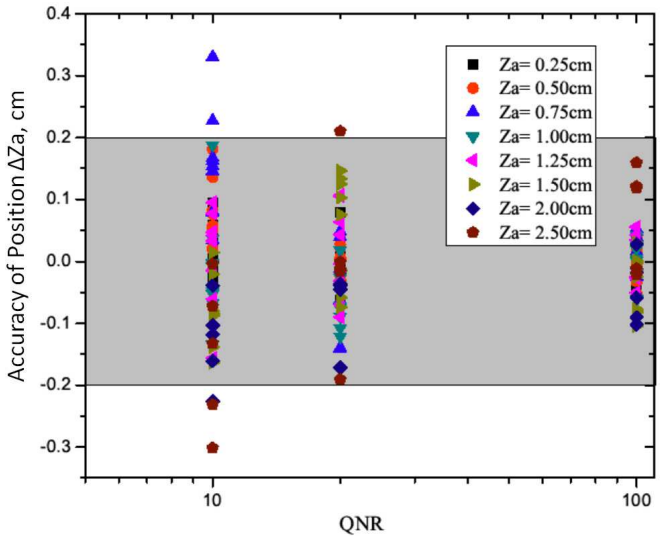

Fig. 3.6 Scatter in measurement accuracy of entry point position and QNR for different insertion points. Za is the distance between insertion point and the main segment edge. For QNR = 100 the error is minimal and the analysis returns the correct value. With decreasing QNR the scatter of the data points increases.

of the main segment), or when the QNR is lower than 10, the uncertainty rises up to $\pm 4^{\circ}$.

3.3 Laboratory Verification

3.3.1 Dust Accelerator Facility

The experiments were carried out using the 2 MV Van de Graaff accelerator located at the Max-Planck Institute of Nuclear Physics (MPIK, Heidelberg), which is operated by the Institute of Space System at University of Stuttgart (IRS, Stuttgart), as shown in Figure 3.8. To avoid sparking, the voltage generator (right hand side of Figure 3.8) is protected by a surrounding pressure tank (SF_6 + N_2, 16 bar). The dust accelerator facility enables the acceleration of micron- and submicron-sized electrically conductive dust powders to speeds between 1 and 100 km·s^{-1}. Single grains can be selected with a well defined speed and size range. The laboratory model was mounted on the moving platform in the vacuum tank of the accelerator. Before reaching the LDX detector, each particle passes through a cylindrical dust charge detector [75]. The detector operates similarly to LDX: the charged particle induces a charge signal. Its amplitude Q_d is directly correlated with the particle primary charge and the signal width corresponds to the particle speed v_d and the length of the cylinder electrode of 20 cm.

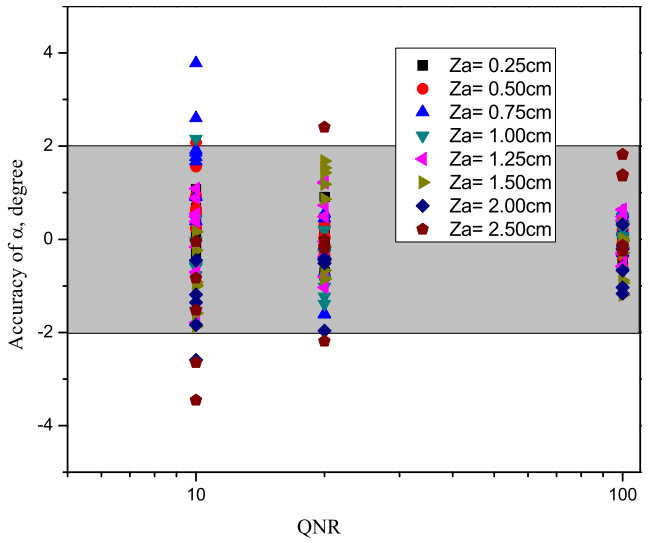

Fig. 3.7 Scatter in angular accuracy and QNR for different insertion points. The angular accuracy was calculated from the position accuracies of the two planes (Plane A and Plane B).

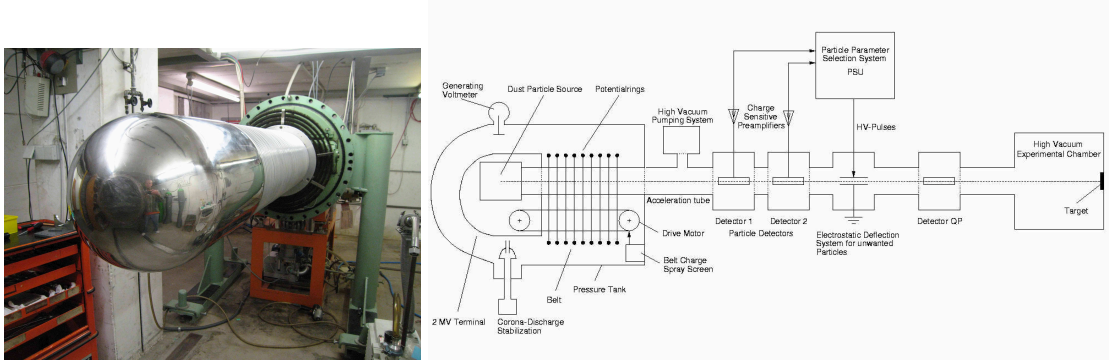

Fig. 3.8 The dust accelerator facility used in the experiments. The Van de Graaff accelerator stage (without pressure tank) at MPIK (right hand side) and the schematic representation of a Van de Graaff accelerator with the particle selection unit (PSU) system. After acceleration, charged projectiles fly along the beam tube, passing the charge and velocity detectors, and then arrive at the particle selection unit. When a suitable projectile arrives, the deflection electrodes are temporarily grounded to allow an undisturbed flight pass towards the target chamber.

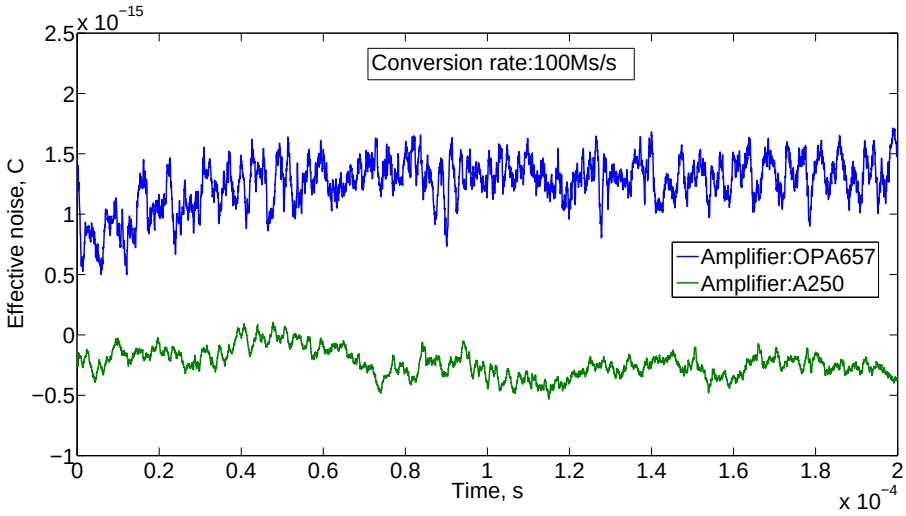

Fig. 3.9 The white noise of the two amplifier types. The blue line is the noise signal of OPA657 amplifier and the green line is the noise signal of A250 amplifier.

3.3.2 Experimental Results

The selection of the low noise charge sensitive amplifiers is an essential task to record the induced charge signals at the electrodes. In our experiments, two different typical CSA designs were used, OPA657 from the Texas Instrument and A250 from AMPTEK, for comparison. The OPA657 combines a high gain bandwidth, low distortion, voltage feedback operational amplifier. The A250 is a hybrid charge sensitive preamplifier for a wide range of detectors with capacitances from less than one to several thousand picofarads. During tests, two types of CSAs, OPA657 and A250, were connected to the grid electrodes on Plane A and Plane B, respectively. All of the amplifiers and electrodes were connected under identical conditions with shielded cables. The white noise comparison between the two types of CSAs is shown in Figure 3.9. From these preliminary results, the A250 amplifier has a noise of 0.5 fC (2900 electrons) and the OPA657 amplifier has a noise about 2 times larger (about 1 fC). What should be noted here is that the well screened dust accelerator beam detectors are using the same A250 amplifiers and they have a noise of less than 1000 electrons [75]. As the sensitivity of a charge induction detector is determined by the noise of the amplifier, better connections and electronics are needed for the future developments.

The charge, speed and trajectory information of individual particles are obtained from the induced charge signals. Figure 3.10 shows a typical result when a particle flies through the detector. The experimental results record two types of signals from the 'Main Segment' and two 'Neighbor Segments' of Plane A and Plane B, which is similar to our simulation

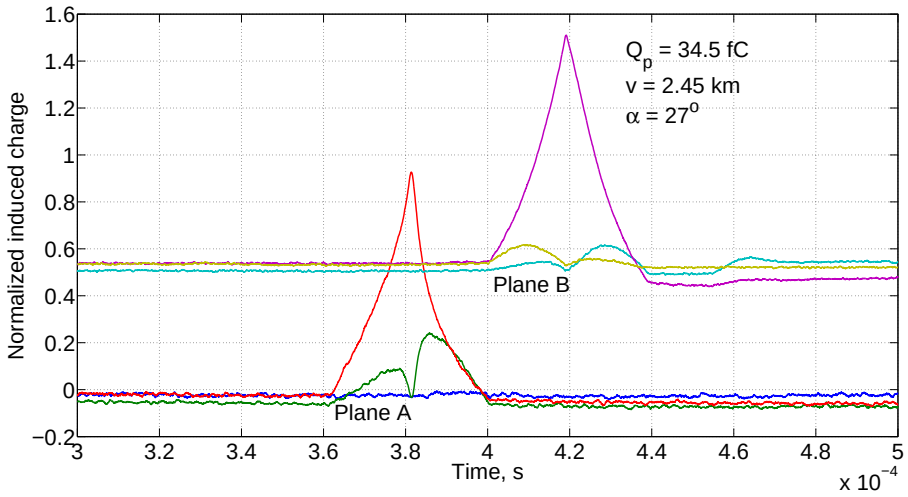

Fig. 3.10 Signals for a dust grain impacts on the target. The bottom three signals belong to the channels of Plane A, which were connected to an OPA657 amplifier unit. The top three signals belong to the channels of Plane B with an A250 amplifier unit. The particle grain flies through all of the grids and impacts on the target which creates an ionization charge.

results. There are also some other incomplete signals when the particle impacted on the nylon structures or the grid electrodes before reaching the target, which are shown in the Figures 3.10 to 3.13. More experimental signals are shown in Appendix A.

In most experimental cases, the detected particle charge Q_d recorded by 'Main Segment' electrodes get about 90% of the primary particle charge Q as shown in Figure 3.14. There are two explanations why the detected particle charge is lower than the primary charge: (1) The wall of the detector attract some part of the induced charge, even the mesh size of the grid is quite small (1.5×1.5 mm^2); (2) The signal of the 'Main Segment' detector is a peak pulse, unlike the square pulse signal obtained by a 20 cm tube detector. The signal processing might lose some induced charges as well. Hence, we suggest that the value of the measured particle charge needs to be multiplied by a factor k ($k = 1.1$ for the laboratory model) in future.

The measurement accuracy of the particle charge by LDX is better than $\pm 5\%$ as shown in Figure 3.15. For the particles with surface charges above 10^{-14} C, the measurement accuracy is much better. The red bars in Y-axis show the measurement accuracy with different particle charge ranges (red bars in X-axis).

The speeds v_d detected by LDX are closely in line with the values of v given by the tube detector of the accelerator beam as shown in Figure 3.16. The measurement accuracy of particle speed by LDX is better than $\pm 7\%$ (Figure 3.17). In Figure 3.17 the red bars in

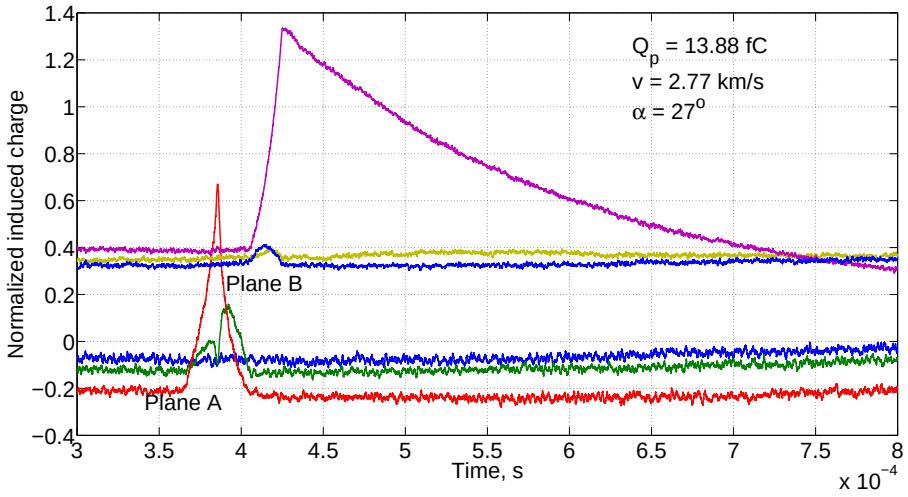

Fig. 3.11 Signals for a dust grain impacts on Plane B. Particle grain impacts on the grid electrodes of Plane B, which provides half of the normal induced charge.

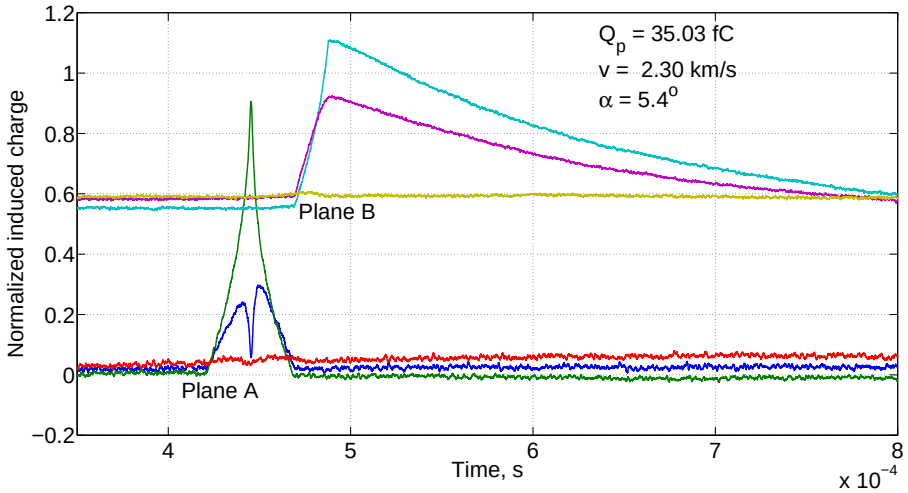

Fig. 3.12 Signals for a dust grain impacts on Center Plane. Particle grain impacts on the grid electrodes of the Center Plane. The generated impact charges were observed by two electrodes of Plane B.

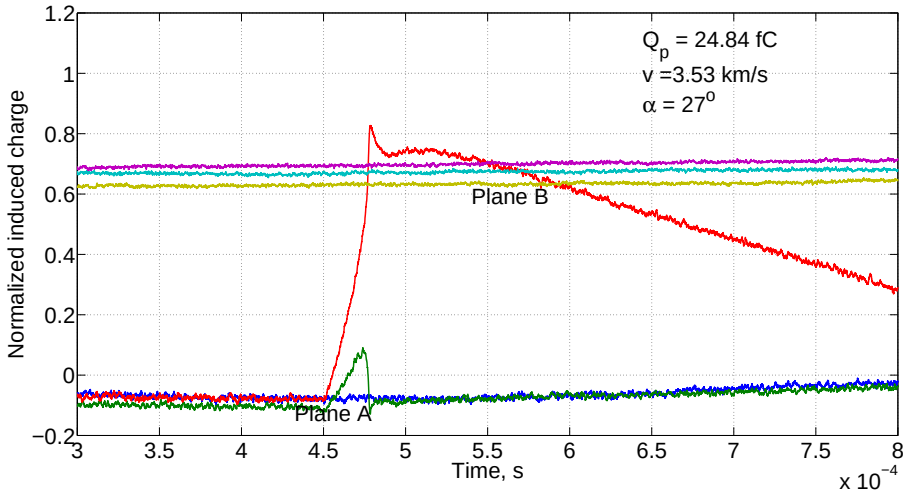

Fig. 3.13 Signals for a dust grain impacts on the nylon frame of Plane A. The impact ionization charge is very tiny in this case.

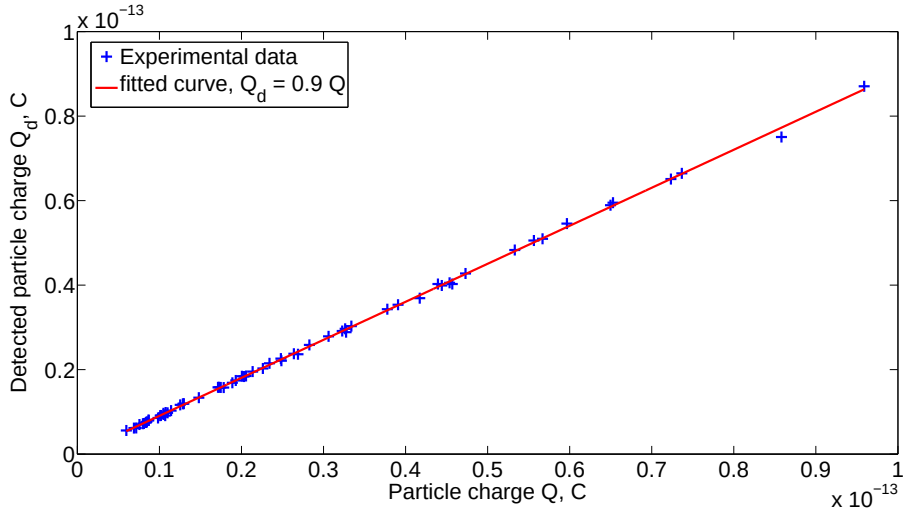

Fig. 3.14 The particle charge comparison between the tube detector of the dust beam and LDX (Q_d). Particle charge (Q) values were obtained by the tube detector system of the accelerator. Blue '+' points show the experimental data and the red line shows their fitted curve.

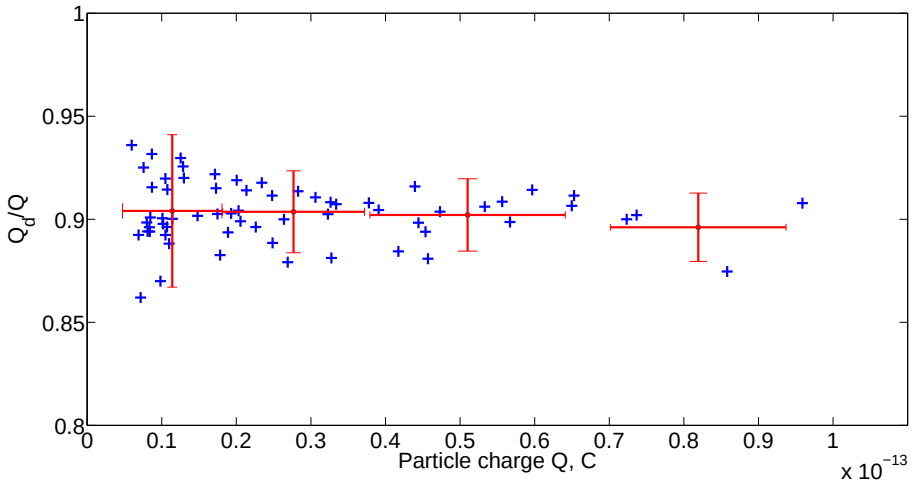

Fig. 3.15 The particle charge measurement accuracy. In the figure, blue '+' points show the experimental data and red bars show the measurement accuracy with different particle charge ranges.

Y-axis show the measurement accuracies with different particle speed ranges (red bars in X-axis).

Our experimental results show that the measurements for both, charge and speed, using the LDX laboratory model are in good agreement with the dust beam detector, which is established for a long time.

The laboratory testing of particle positions is limited by the dust beam spot (about 10 mm in diameter), it is not possible to obtain the accuracy position information of an individual dust particle. We selected three test positions for the 5 cm width grid electrode from edge (Za = 0 mm) to center (Za = 2.5 mm). As shown in Figure 3.18, all of the test results concentrated in regions calculated by Equation 3.3, which implies that the accuracy of the detector on position detection is close to the simulation.

We introduced the experimental results of a laboratory model based on the design of LDX. The results of the measurements can be summarized as follows:

(1) The design of LDX has high accuracies for the measurement of particle charges (better than $\pm$5%) and speeds (better than $\pm$7%).

(2) An advantage of the grid electrode based design of LDX is the detection of nearly 100% of the dust particle primary charge in each electrode plane. This value is more than twice as high as for a detector using individual wires. Because of the wall effect and signal smoothing, the dust primary charge Q is larger than the detected value Q_d, where $Q = k \cdot Q_d$ (k $>$ 1, for the design of LDX, k = 1.1).

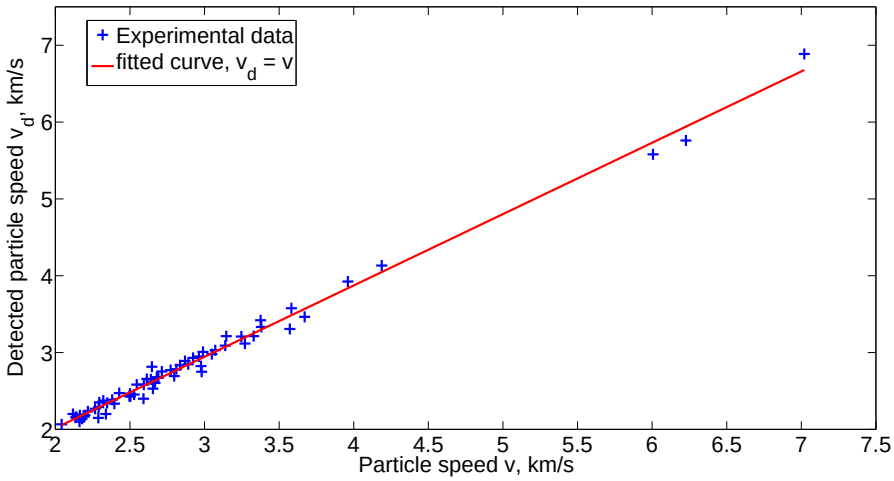

Fig. 3.16 The particle speed comparison between the tube detector of the dust beam (v)and LDX (v_d).

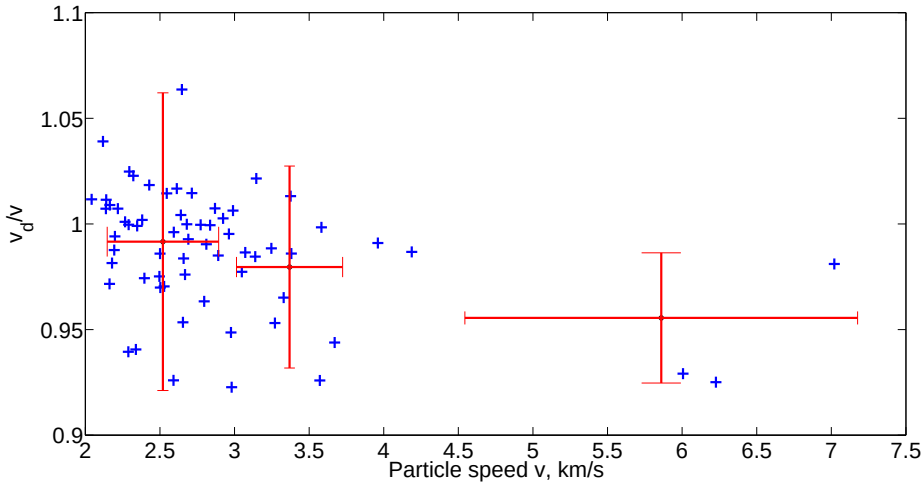

Fig. 3.17 The particle speed measurement accuracy. In the figure, blue '+' points show the experimental data and red bars show the measurement accuracy with different particle speed ranges.

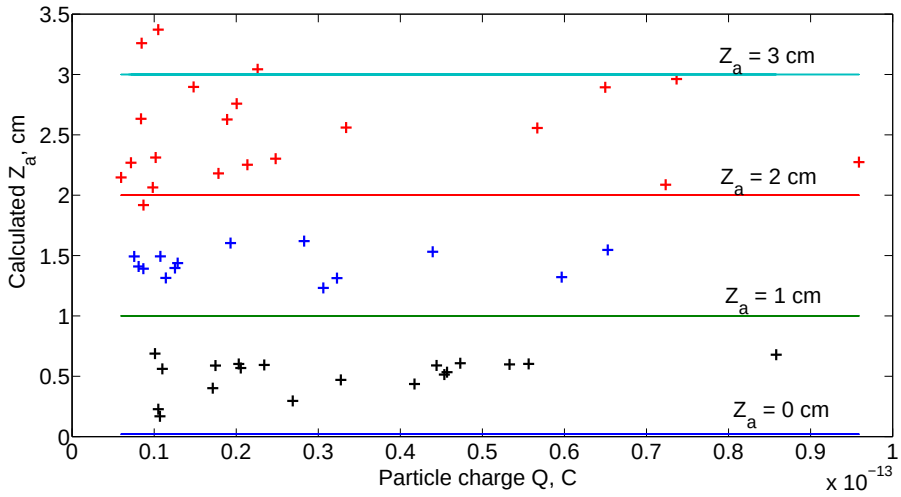

Fig. 3.18 Particle trajectory parameter Z_a of the Plane A derived from signal shape of the induced particle charge. In the figure, black '+' points show the data obtained from the range $Z_a = 0$ to $Z_a = 1$ cm; blue '+' points show the data obtained from the range $Z_a = 0$ to $Z_a = 1$ cm; red '+' points show the data obtained from the range $Z_a = 2$ to $Z_a = 3$ cm.

(3) The signals are highly symmetric and the amplitudes in each plane are equal which is beneficial for the means of digital filters in future instrumentation, and the design will allow for low speed (< 1 km·s^{-1}) particle measurements. For the detection of high speed (> 1 km·s^{-1}) particles, impact ionization can be added to provide trigger signal [73].

Chapter 4

Observation Requirements

The grains of the three dust populations above the lunar surface (interplanetary Dust Particles (IDPs), impact ejecta and lofted dust) follow different trajectories. IDPs are supposed to enter the LDX aperture with a broad distribution in elevation and azimuth. The impact ejecta grains generated by the bombardments of interplanetary impactors launch from the lunar surface with different directional and velocity properties. The levitated dust grains are thought to move slowly in horizontal direction lofted by a near surface electric field.

Can dust particles be measured by a sensor located directly on the surface of the moon? Which sensor boresight orientation is suitable for the detection of secondary ejecta? In this chapter we discuss the parameters of the three types of dust grains and their observation requirements for the dust detector located on the lunar surface or on a lunar lander.

4.1 External Dust Sources

The majority of external dust sources is interplanetary dust coming from a variety of sources inside our planetary system. Cometary dust is most famous and shows up as meteor streams easily recognized from the ground. Other meteorites come from differentiated objects such as asteroids, the Moon or the planet Mars, or are still undifferentiated and preserve the cosmic elemental abundance.

Each year, the surface of the Moon is bombarded by about 10^6 kg of interplanetary micrometeoroids of cometary or asteroidal origin. Most of these projectiles have diameters varying from 10 nm to about 1 mm, and they impact on the surface of the Moon at speeds from 10 to 72 km·s^{-1}. They may excavate the lunar soil with a yield of up to 1000 times of their own mass [34]. These impacts leave crater records on surfaces from which the

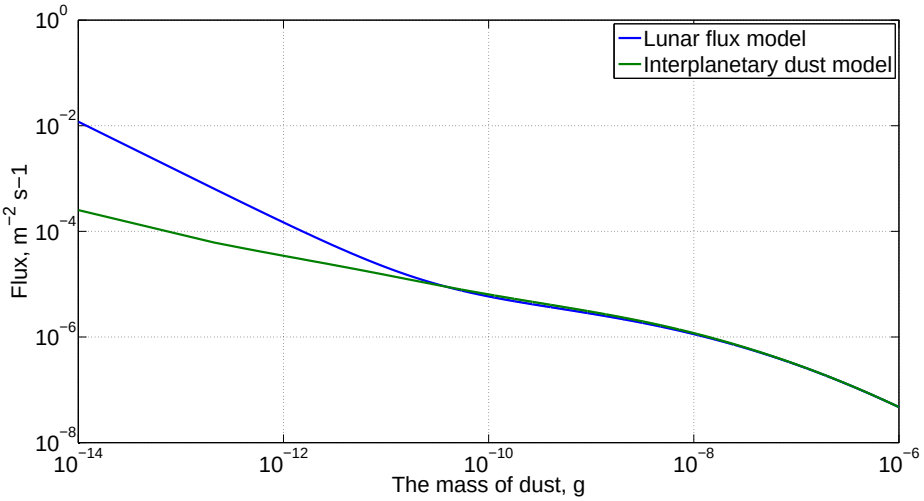

Fig. 4.1 Interplanetary dust flux (green line) and impactor flux (which is derived from craters, blue line) at the lunar surface [35]. The difference between these two fluxes makes the importance of the secondary ejecta observation.

micrometeoroid size distribution has been deciphered [48]. Most of the excavated mass returns to the lunar surface and blankets the lunar crust with a highly pulverized layer [35].

The Grün model assumes an isotropic environment with a viewing angle of 2π. Hence the total amount N_i of potential interplanetary dust which could be obtained by a detector located on the lunar surface is:

$$N_i = f_i \cdot \frac{FOV}{2\pi} \cdot A \cdot t \tag{4.1}$$

where, f_i is the interplanetary dust flux calculated by the Grün model, as shown in Figure 4.1. The parameters FOV and A are the field of view and the open area of the detector, which have values of $\pi/2$ and 0.04 m^2 for LDX, respectively. t is the operational time of the mission. What should be noted is that the Moon shields half of the interplanetary dust population for the detector mounted on its surface and the field of view of the detector has to multiplied by a factor of 0.5. The impact rate at the detector for interplanetary dust grains larger than 0.1 μm diameter (about 10^{-15} g), with a density of 2.5 g·cm^{-3} is calculated by:

$$N_i = 1 \times 10^{-3} \cdot \frac{\pi/2 \cdot 0.5}{2\pi} \cdot 0.04 = 5 \times 10^{-6} s^{-1} \tag{4.2}$$

4.2 Lunar Dust Sources

4.2.1 Lunar Impact Ejecta Environment

An impact crater is more than a mere hole in the ground. The material excavated from the crater and deposited on the surrounding terrain is called ejecta. The impact phenomenon of fast secondary ejecta impacting on the surface is a fundamental process for the change of the lunar surface. Grün et al. [35] compared the in-situ spacecraft measurements and the optical observations of rock samples taken back during the Apollo missions. The observed size distribution of craters on the samples usually does not agree with the flux of interplanetary dust particles with masses of less than 10^{-10} g (see Figure 4.1). These micron sized craters are probably created by the secondary ejecta impacts. Based on the experimental results from Zook et al. [90], the number of secondary impact pits from oblique impact angles is more than two orders of magnitude higher than from primary impacts. This underlines the importance of ejecta measurements on the lunar surface.

The impact process can be separated into two time stages by ejecta dynamics. In the early-time stage of impact process, the projectile is still coupling its energy and momentum to the target leading to different ejecta dynamics compared to the main-stage [40]. The pressures are highest in the impact point zone, and the materials ejected near the impact point are therefore dominated by small fragments with high speeds and shallow ejecta angles with respect to the target surface. These impact ejecta grains can be observed by a dust sensor located on the lunar surface [16, 56].

The angular and speed distributions of ejecta launched from the impact zone determine their trajectories. Hoerth et al. [41] studied the angular and speed distributions of ejecta by experimental methods. They found that the ejecta cone angles range from 44 degrees to 60 degrees with respect to the target surface for vertical impacts during the early-time stage. As the process continues, grains with larger sizes, slower velocities and more vertical ejection angles with respect to the target surface launch from the crater zone as shown in Figure 4.2.

The individual ejecta grains travel on ballistic trajectories determined by their velocity vectors at which the materials are ejected, and by the gravity field of the Moon. Ejecta grains with velocities exceeding the escape velocity (2.4 $\mathrm{km \cdot s^{-1}}$) become interplanetary dust particles, which takes an important role for the determination of the dust density and flux near earth [81]. However, most of the excavated mass returns to the lunar surface and blankets the lunar crust with a highly pulverized layer [34].

All airless planetary bodies are expected to be surrounded by dust clouds, which were firstly detected by the dust detector onboard the Galileo spacecraft during the close flybys

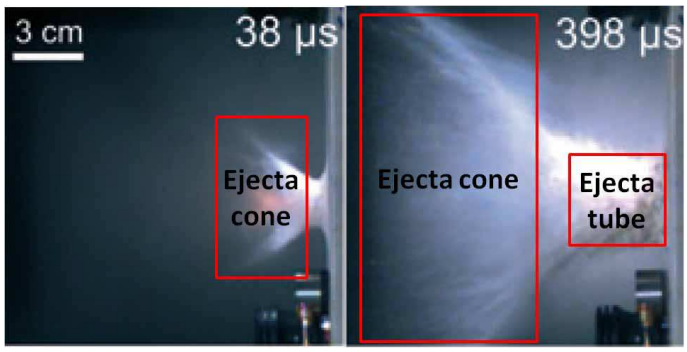

Fig. 4.2 Typical ejecta evolution at different time steps during an impact experiment. The left side of the figure shows the initial ejecta cone and the right side of the figure shows the ejecta cone and ejecta tube [41].

of icy moons of Jupiter [54]. Based on the latest data, the Lunar Dust EXperiment (LDEX) sensor onboard lunar orbiter Lunar Atmosphere and Dust Environment Explorer (LADEE) already identified the existence of a dust cloud around the lunar surface down to 5 km [47]. The ejecta created by the impacts of interplanetary meteoroids are thought to be one of the main components of the dust cloud.

The speed and angular distributions of the ejecta grains vary with impact parameters, including the projectile speeds and impact angles [2, 41]. Correspondingly, the speed and trajectory measurements of ejecta particles with a sensor would yield valuable information of its parent impactor.

4.2.2 Impact Simulations

What are the dust populations a sensor like LDX can detect on the lunar surface? How big is the contribution by impact ejecta falling back to the surface and what is their angular distribution and speed range? In this study, these questions are answered by the software tool - AUTODYN 14.0/2D, which was used to study the ejecta velocity and angular distributions during the early-time stage process of interplanetary dust particles hitting the lunar surface.

The projectiles and targets were implemented with the Smooth Particle Hydrodynamic (SPH) method using 0.5 μm nodes in size. The velocity vector of each ejecta was recorded and analyzed. The semi-finite target is 200 $\times$ 200 μm^2 in size with about 110000 SPH nodes in total. As a material for the regolith target we selected the CONC-35MPA model from the AUTODYN material database. The same material was applied to the projectile properties. CONC-35MPA applies the Riedel-Hiermaier-Thoma (RHT) strength model, which is widely used to simulate the hyper-velocity impact process of brittle materials [66].

The angular and velocity distributions of dust particle bombardments on the lunar surface are generally derived from ground based observations of the meteoroids [1]. In this study, we simplified the distributions as follows. The projectiles impact on the target with angles α ranging from 15° to 90° (see Figure 4.3). For the impact speed we took the maximum of the speed distribution at 1 AU of 17 km·s^{-1}. The speed distribution was measured by LDEF and published by Zook [89].

An instrument like LDX can detect particles in a wide speed and mass range. The speed threshold for ejecta dynamic measurements is limited by the instrument design method. For the induced charge method, only ejecta grains with speed above 50 m·s^{-1} can provide useful output signals for trajectory measurement, which is related to the bandwidth of charge sensitive amplifiers (CSAs). The detectable ejecta grains above the lunar surface should be larger than 0.5 μm to obtain enough surface charge in milliseconds ($>$ 0.1 fC) charged by UV photoionization during the daytime [67]. During the night measurement period, the size threshold of ejecta charged by plasma with potential of -200 V can be down to 20 nm with charging times of microseconds [11, 15, 52]. Here, ejecta grains larger than 0.5 μm are observation goals, and they will be separated into a lower speed population (50 m·s^{-1} $< v_{ejecta} \leq$ 1 km·s^{-1}), and a high speed population ($v_{ejecta} >$ 1 km·s^{-1}). This separation will benefit the design of trigger methods of the detector: (1) the induced charge signals of lower speed ejecta events need to be triggered by analog and digital system, and (2) the high speed ejecta events can be triggered by an analog and digital system and/or the impact charge signal obtained by the target.

The primary impactor flux of micrometeoroids is normally described by a negative power law and the flux decrease with particle mass [35], such that only large projectiles can create a sufficient number of detectable ejecta. To balance the number of dust impact events and impact ejecta grain sizes for detector observations, we selected spherical projectiles with a size of 10 μm in diameter (309 SPH nodes in total). This corresponds to a flux of 1.86×10^{-6} m^{-2}·s^{-1} on the lunar surface.

The exact boundary between the early-time stage and main stage of the hyper-velocity impact process for micron sized particles is still unclear. In this study, three time steps of 0.05, 0.075 and 0.01 μs after the impact were selected in order to determine the approximate boundary of the early-time stage. The impact simulation and dynamical ejecta parameters are shown in Figure 4.3. All impactors have a speed of 17 km·s^{-1} and their impact angles α are 15°, 30°, 45°, 60°, 75°, and 90° with respect to the horizon. Projectiles with incident angles of 90° represent vertical impacts. The ejecta incident angle β is positive in the forward direction and negative in the opposite direction.

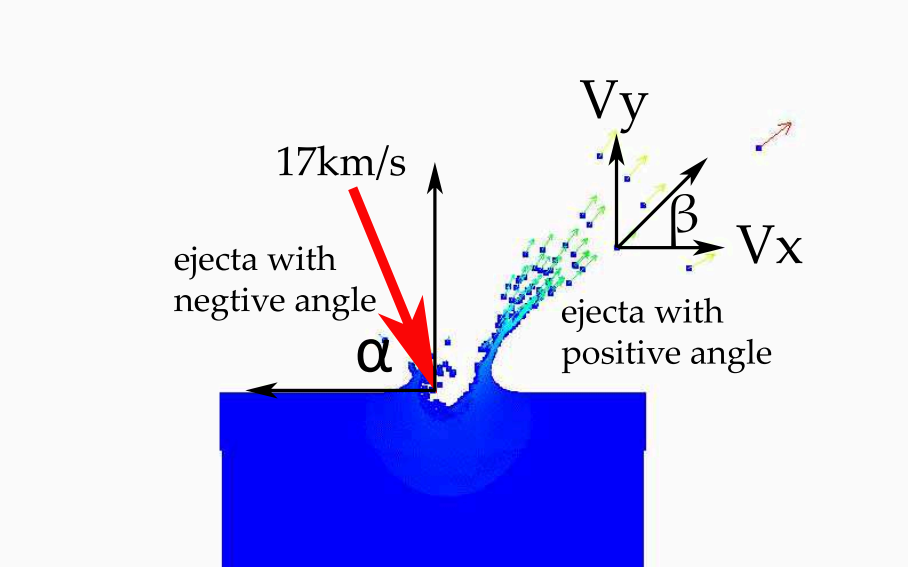

Fig. 4.3 Schematics of the impact ejecta parameters. α is the impact angle with respect to the target surface. The impact ejecta grains are separated into two populations by their starting direction with respect to the impact direction of the projectile. Ejecta grains in the forward direction have positive angles β.

Figure 4.4 shows the relationship between the ratio of the selected ejecta mass to the projectile mass and the impact angle at different time steps after the impact. The two ejecta populations are selected by their speed corresponding to different trigger methods (induced charge or impact ionization). The total mass of low speed ejecta (50 m·s^{-1} $< v_{ejecta} \leq$ 1 km·s^{-1}) has a slow growth for short time steps (0.05 and 0.075 μs) for impact angles above 45°. As the impact process is ongoing, the total mass of low speed ejecta has a linear growth with impact angle. The ejecta generated after 0.075 μs have larger incident angles β, which are thought to be created by the rebound of target material during the main stage of the impact process. More significant results are shown in Figure 4.4(b) for the high speed ejecta population, especially for the vertical impact (α = 90°). Hence, we define the time step of 0.075 μs after the impact as the early-time stage boundary in this study. The mean mass yield of ejecta with speeds above 50 m·s^{-1} is about 3.3 in the early-time stage of the impact process.

The speed distribution of ejecta created at the early-time impact process is shown in Figure 4.5. What should be noted is that for oblique impact events there are a limited number of ejecta grains with speeds higher than the value of their parent projectile. The related amount of low speed ejecta increases with impact angle and the maximum of ejecta distribution ranges from 10 km·s^{-1} to 1000 m·s^{-1} for α = 15° and α = 90°, respectively.

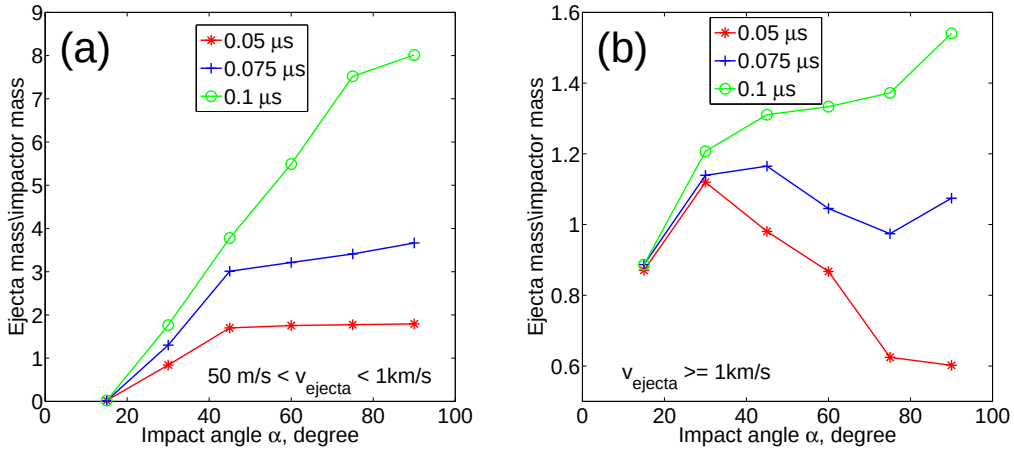

Fig. 4.4 Relationship between the mass yield and impact angle in the early-time stage. In the figure, (a) ejecta with speeds of 50 m·s^{-1} $< V_{ejecta} \leq$ 1 km·s^{-1}. (b) ejecta with speeds of $V_{ejecta} \geq$ 1 km·s^{-1}. The impactor has a diameter of 10 μm and a speed of 17 km·s^{-1}.

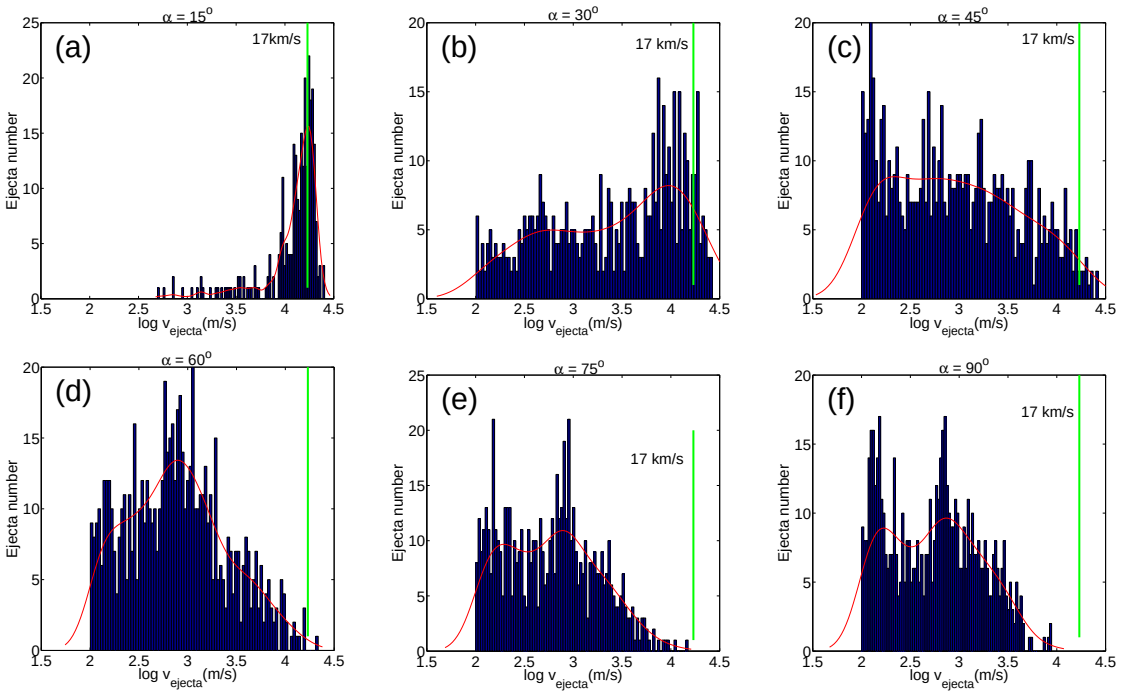

Fig. 4.5 Ejecta speed distributions vary with impact angle at the early-time stage. α is the impact angle of the projectile. (a) α = 15°, (b) α = 30°, (c) α = 45°, (d) α = 60°, (e) α = 75°, (f) α = 90° (vertical impact). The red lines are the fitted ejecta number distribution curves and the green lines show the impact speed (17 km·s^{-1}). The projectile has a diameter of 10 μm and a speed of 17 km·s^{-1}.

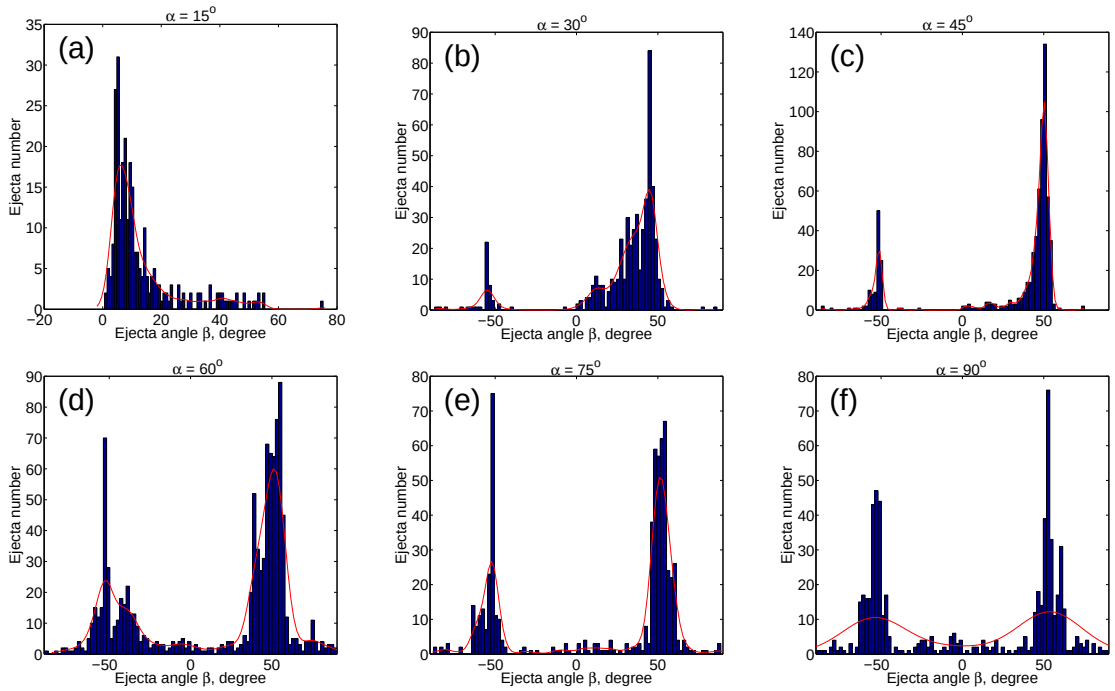

Fig. 4.6 Ejecta angular distributions vary with impact angle at the early-time stage. α is the impact angle of the projectile. (a) $\alpha = 15°$, (b) $\alpha = 30°$, (c) $\alpha = 45°$, (d) $\alpha = 60°$, (e) $\alpha = 75°$, (f) $\alpha = 90°$ (vertical impact). The red lines are the fitted ejecta number distribution curves. Most ejecta are moving in the forward direction for the oblique impact with $\alpha = 15°$. With increasing impact angle the amount of ejecta in the opposite direction rises. For a vertical impact ($\alpha = 90°$), the two populations have a similar number of ejecta. The impactor has a diameter of 10 μm and a speed of 17 km·s^{-1}.

The angular distribution of ejecta has two major components appearing at the range of [-60°, -40°] and [40°, 60°] for events with different impact angles except for events with an impact angle α = 15° (see Figure 4.6). The difference between the two ejecta populations might be caused by the effect of downrange-direction momentum transfer [2]. More high speed ejecta grains are created in the forward direction of the impactor. The corresponding amount of ejecta with negative angle (in the opposite direction of impact) increases with impact angle. The two components of the ejecta with opposite directions have similar numbers for vertical impacts.

4.2.3 Lofted Dust

Fine grains from the lunar surface can be lifted due to human activities, and there are indications that lunar fines can be electrostatically charged and naturally transported under the influence of near-surface electric fields. Observations by the Apollo astronauts of

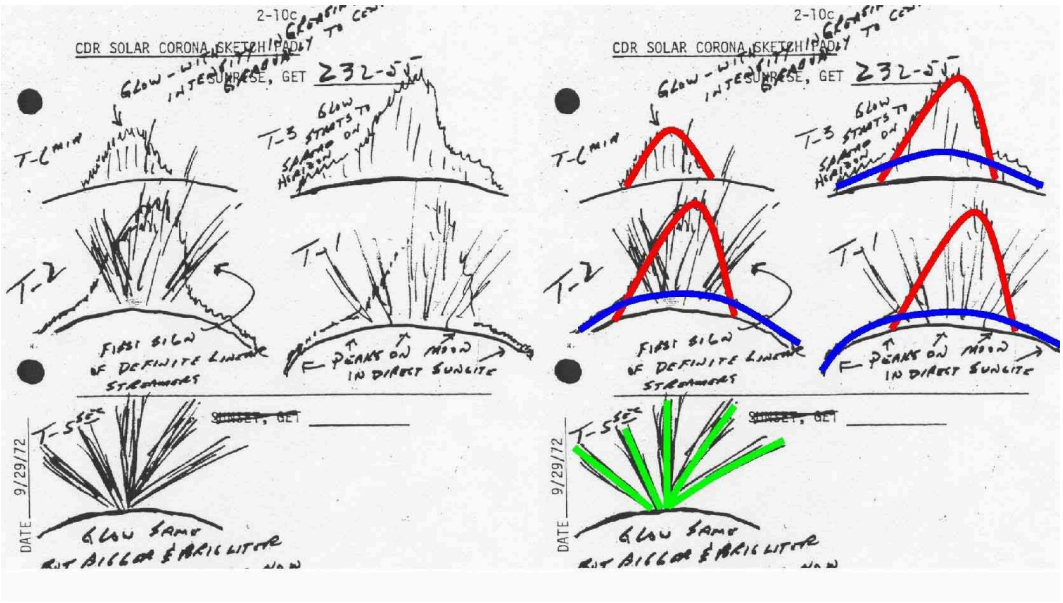

Fig. 4.7 Lunar 'twilight rays' sketched by the Apollo 17 astronauts. Highlighted are the sources of the scattered light: Coronal and Zodiacal Light (red); Lunar Horizon Glow due to exophoric dust (blue); and possible 'crepuscular rays' formed by shadowing and scattered light (green). Image is credited by NASA.

horizon glow phenomena (see Figure 4.7) and sticking of dust to their space suits even after short extravehicular activities (see Figure 1.2) demonstrated the importance of the control of dust contamination [18]. Simple instruments placed on the lunar surface can monitor both natural and man-made dust coverage and cleansing effects which are not fully understood.

The typical height which an electrostatically levitated dust grain can reach depends on its surface charge at the time of ejection from the lunar surface. Murphy and Vondrak [61] assumed an exponential distribution of dust with radius r and with altitude z for particles in accordance withe the horizon glow figures obtained by orbiters. The related formula is:

$$\rho(r,z) = \frac{n_0}{r} exp(-\frac{r^{8/3}z}{2\times 10^{-15}}) \tag{4.3}$$

where n_0 is a scaling factor in m^{-3}, r is the radius of dust grains ranging from 0.1 μm to 6 μm and z is the altitude above the lunar surface. Collier and Stubbs [20] reported the relation n_0 = 4.0 $\times$ 10^5 m^{-3}. The dust concentration for particles with sizes within the range of [r_{min},r_{max}] is obtained by:

$$f_{lofted} = \int_{r_{min}}^{r_{max}} \rho(r,z)dr \tag{4.4}$$

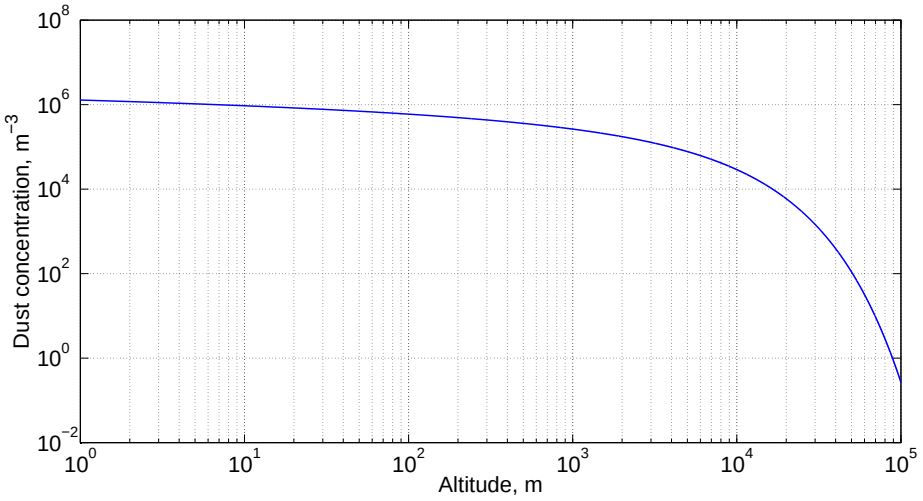

Fig. 4.8 Dust concentration as a function of altitude at the lunar terminator. The dust grain density was calculated by Equation 4.14 with the radius from 0.1 to 6 μm.

A numerical integration for Equation 4.3 and 4.14 for different altitudes is shown in Figure 4.8. The exosphere dust concentration can be described by a function of the altitude at the lunar terminator.

Assuming photoemission as the only contribution for the charging process and the gravitational force as the only acting force, and neglecting the electrostatic force outside the Debye length, Stubbs et al. [76] set up a theoretical formula for the dust grains following ballistic lofting trajectories. Their highest position Z_{max} and the lofting velocity v_{max} can be obtained by: .

$$Z_{max} = \frac{12\varepsilon_0\Phi^2}{\rho_p g_l d_p^2} \tag{4.5}$$

$$v_{max} = \sqrt{2g_l Z_{max}} = \frac{\Phi}{r}\sqrt{\frac{6\varepsilon_0}{\rho_p}} \tag{4.6}$$

where Φ is the surface potential; ε_0 is the vacuum space permittivity, 8.85×10^{-12} F·m^{-1}; ρ_p is the dust grain density, which was assumed as 2.5 g·cm^{-3} in this study; g_l is the gravitational acceleration at the lunar surface, 1.62 m·s^{-2}; and d_p is the diameter of dust grains and $d_p = 2r$.

4.3 Detector Boresight

The three populations of dust grains above the lunar surface have different trajectories and distributions in the vertical. The mounting location and the boresight of the dust detector depends on its scientific goals and on the parameters of dust grains. Three possibilities have been considered for the location of LDX to measure the levitated dust particles, IDPs or their ejecta: (1) on the top of the lander (3 m above the surface); (2) below the lander (1 m above the lander); and (3) on the lunar surface (with legs, 0.5 m above the surface).

4.3.1 Detector Positioning

Which are the most suited locations of the sensor at the spacecraft bus? People might get the answer by reanalyzing the measurement results of previous experiments. The most well known dust sensor placed on the lunar surface is the LEAM experiment during Apollo 17. The objectives of LEAM were to detect secondary ejecta created by the hyper-velocity impacts on the lunar surface and to detect interplanetary dust grains [14]. The experiment has three sensors pointing to the west, east and up directions, which are called West sensor, East sensor and Up sensor in the following paragraphs. The sensors were multi-layered arrays in order to identify the velocity, trajectory and kinetic energy of incident dust grains. A basic sensor (West or Up sensor) consists of a front film-grid sensor array and a rear film-grid sensor array (Figure 4.9), while the East sensor just has the rear film-grid array. The performance of the sensor depends on two basic measurable phenomena that occur when a hyper-velocity particle impacts on a surface: the formation of a plasma and a transfer of momentum. When a low energy particle enters the front sensor, it yields all its kinetic energy at the front film. A pulse-height analysis is performed on the positive output signals as a measure of the kinetic energy of the particle. A relatively high speed particle may pass through the front film sensor and yields some of its kinetic energy toward the generation of impact charge. As the particle continues its path, it achieves its remaining energy at the rear sensor film with a secondary set of impact charge.

Figure 4.14 shows the events recorded by the LEAM sensors per 3-hour intervals averaged over 22 lunations. The sensor recorded hundreds of events per day instead of a few impacts per day recorded by Pioneer 8 and 9. This result also does not coincide with the ejecta and interplanetary dust flux, as shown in Figure 4.1. One possible explanation is that LEAM was registering slowing moving (< 100 m·s^{-1}) and highly charged (> 1 pC) lunar dust particles, caused by the sunrise/sunset triggered levitation and transport phenomena. These results are still contradictory and they were discussed by O'Brien [63] and Grün and

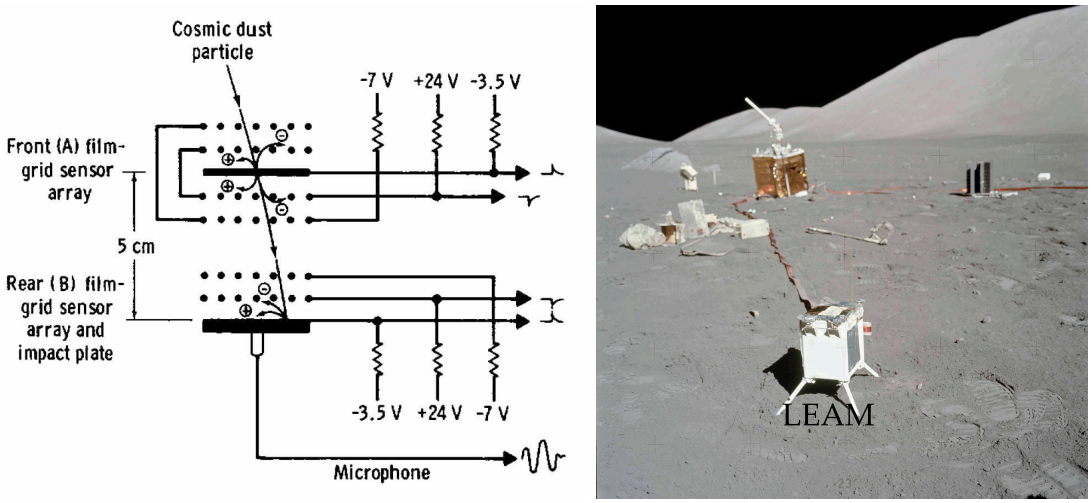

Fig. 4.9 Schematic diagram of the West and East sensor (left side) of LEAM [14]. The front film consisted of 0.3 μm thick aluminized pargyline film. The instrument was deployed at the lunar surface during the Apollo 17 mission (right side, NASA Apollo 17 photograph [62]). Here, the sensors are still protected with a dust cover and the West sensor is hidden in this view.

Horányi [33].

4.3.2 Detection of Secondary Ejecta

Without air resistance, the individual ejecta fragments follow their own ballistic trajectories determined by the gravity field of the Moon (g = 1.62 m·s^{-2}). A dust sensor placed on the lunar surface can measure the ejecta grains moving upwards from the impact point, which we called rising ejecta (see up sketch in Figure 4.11). In contrast, the ejecta grains with launch speeds lower than the escape speed of the Moon (2.4 km·s^{-1}) will fall down to the lunar surface from the vertex of their trajectories, which we called falling ejecta (see bottom sketch in Figure 4.11). The height H of dust detector is an important parameter for the observational geometry, which determines the effective surface area where ejecta can be detected from. The LEAM instrument was standing on the lunar surface with 4 legs, which has an approximate height of only 0.5 m above the lunar surface. In contrast, the LDX-like sensor mounted on the top of a lunar lander (e.g. ESA Lunar Lander) has an approximate height of 3 m above the lunar surface. The effective distance D labeled in the figure is the distance between the impact location and the sensor.

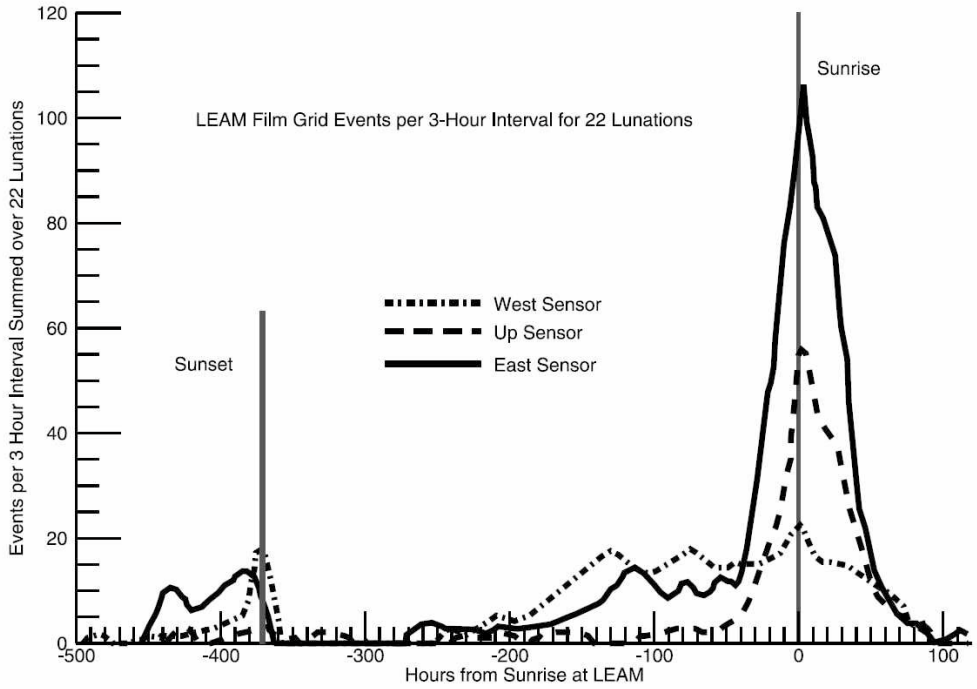

Fig. 4.10 Events recorded by the LEAM sensors per 3-hour intervals averaged over 22 lunations [16]

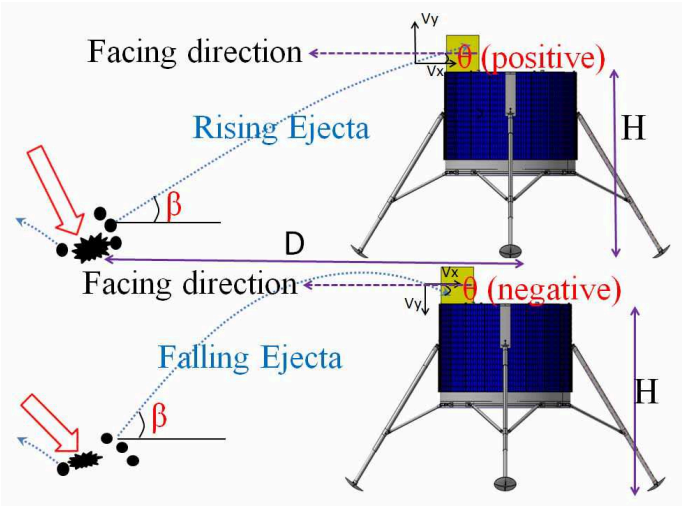

Fig. 4.11 Ejecta trajectories and dust sensor placed on the lunar surface. β defines the primary ejecta angle at the impact point. θ defines the entry angle of ejecta into the instrument with respect to the horizon, which has positive values for rising ejecta moving upwards and negative values for falling ejecta moving downwards. H defines the height of the dust sensor above the lunar surface.

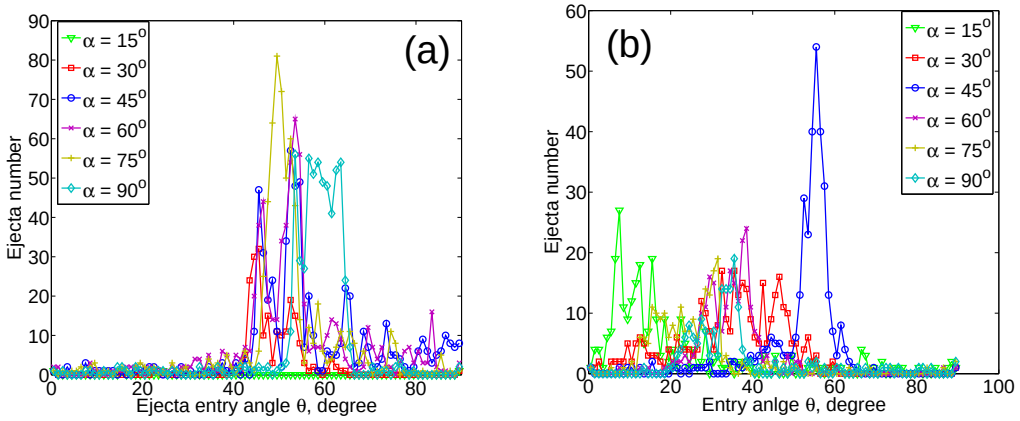

Fig. 4.12 Distribution of the rising ejecta entry angle θ (positive) to an ideal sensor placed on the lunar surface. In this study, the ejecta grains are separated into the ranges: (a) low-speed (50 m·s^{-1} $< v_{ejecta} \leq$ 1 km·s^{-1}) and (b) high-speed ($v_{ejecta} >$ 1 km·s^{-1}). The ideal sensor here has no measurement limitations (2π field of view), and it can obtain all the ejecta created by an individual impacts events.

Rising Ejecta

Rising ejecta grains are described by ejecta trajectories entering the sensor with positive entry angles θ with respect to the instrument horizontal opening. According to our simulation results, the speed and angular distributions of ejecta particle vary with impact angle of the projectile (see Figure 4.5 and Figure 4.6). Rising ejecta have ballistic trajectories ending at the sensor location with a height H. Figure 4.12 shows the angular distributions of rising ejecta for an ideal sensor placed on the lunar surface. The ideal sensor is defined as a detector with no measurement limitations (2π field of view), and it can obtain all the ejecta created by individual impact events. The rising ejecta grains are separated into two populations by our detection methods: induced charge method for dust with speeds between 50 m·s^{-1} and 1 km·s^{-1}, and the impact ionization method for dust with speeds above 1 km·s^{-1}. The main entry angle range of lower speed rising ejecta is between 40° and 70° (See Figure 4.12(a)). Correspondingly, the high speed ejecta have entry angles which mainly appear in the range between 5° and 65° as shown in Figure 4.12(b).

The number of potential rising ejecta events for a dust sensor located on the lunar surface is a function of the parent interplanetary dust flux F, the facing area A (related to the height H, the facing direction ϕ and FOV of the sensor), the recording time t, the possibility p to measure an individual ejecta particles limited by both the ejecta trajectory and the facing direction of the sensor. The facing area A of a sensor can be calculated by its filed-of-view (FOV) and effective distance D. Since H is quite small comparing with ejecta speed, the

entry angles θ of rising ejecta grains are approximately equal to their original angles β. The number $N_{\theta>0}$ of potential ejecta events with positive entry angles for the sensor is obtained as

$$\begin{cases} D = \dfrac{H}{tan(\phi)}, & (4.7) \\ A_{\theta>0} = \dfrac{FOV}{2\pi} \cdot \pi \cdot D^2, & (4.8) \\ p = f(\phi), & (4.9) \\ N_{\theta>0} = F \cdot A \cdot t & (4.10) \end{cases}$$

Based on our simulation results, the increasing factor of the total ejecta mass created in the early-time stage of the impact process varies with impact angle. The mean mass of created ejecta is about 3.3 times larger than the mass of the parent projectile (see Figure 4.4). An interplanetary dust particle with a diameter of above 10 μm and with an impact speed of 17 km·s^{-1} will create at least 1000 detectable ejecta grains (larger than 0.5 μm). The flux of interplanetary dust particles above 10 μm in size is about 1.86 $\times$ 10^{-6} m^{-2}·s^{-1} on the lunar surface [35].

Falling ejecta trajectories

All of the ejecta particles with speeds below 2.4 km·s^{-1} will fall back to the lunar surface. Falling ejecta grains follow ballistic trajectories entering the sensor with negative entry angles with respect to the instrument horizontal opening. Theoretically there is no general limitation on the effective distance D for the measurement of falling ejecta. The distribution of falling ejecta entry angles θ (negative) to an ideal sensor placed on the lunar surface is shown in Figure 4.13. The ideal sensor is defined as a detector with no field-of-view limitation for the measurement. Most of the falling ejecta grains have angles in the range from 40° to 60° except the impact event with incident angle of 15°. The falling ejecta with speeds between 50 m·s^{-1} and 2.4 km·s^{-1} take about 10% of the entire ejecta population created during the early-time stage of the impact process according to our simulations.

The predictive events of falling ejecta are calculated based on the current measurement results of LDEX [47]. The density d_{cloud} of the dust cloud in the altitude ranges from 0 to 50 km is about 4 $\times$ 10^{-3} m^{-3}. When these grains fall down to the lunar surface, they will have a maximum mean speed $v_{falling}$ of 400 m·s^{-1}. The predicted number $N_{\theta<0}$ of falling ejecta into a sensor with an open area of A_{sensor} and a field-of-view (FOV) placed on the

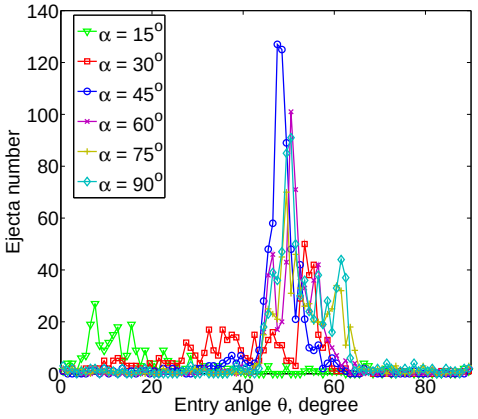

Fig. 4.13 Distributions of falling ejecta entry angles θ (negative) for an ideal sensor placed on the lunar surface for the impact events with different incident angles.

lunar surface is obtained as:

$$N_{\theta<0} = d_{cloud} \cdot v_{falling} \cdot A_{sensor} \cdot \frac{FOV}{2\pi} \tag{4.11}$$

Ejecta as an explanation for LEAM data

The obtained results of LEAM are still contradictory and they were recently discussed by O'Brien [63] and Grün and Horányi [33]. The LEAM sensor recorded hundreds of events per day, but most of these events were registered only in the front films [22]. Figure 4.14 shows the rates recorded by the LEAM sensors per 3-hour interval as reported by Grün and Horányi [33]. In the previous studies [15, 16, 64], the explanation was given, that LEAM was registering slowly moving (< 100 m·s^{-1}) lunar dust particles with surface charges above 1 pC, triggered by the sunrise/sunset levitation and transport phenomena. Assuming a daytime surface potential of +5 V, the measurements indicate grains sizes of the order of a millimeter in radius. Such big sizes are not possible to be lofted just by the weak electric fields on the lunar surface. The direct impact of interplanetary dust particles could be another potential trigger source for the signals. However, the flux of these grains is too low and it is not fitting the high event numbers in the short time intervals (3h). In contrast, our results about ejecta dynamics lead to a more plausible explanation for the measurements of LEAM: the signals were triggered by impacts of secondary ejecta particles originating from the so called early-time impact process. Such ejecta have sufficient speeds to trigger the sensors of LEAM.

The field-of-view (FOV) of each sensor on the LEAM experiment is a square cone with

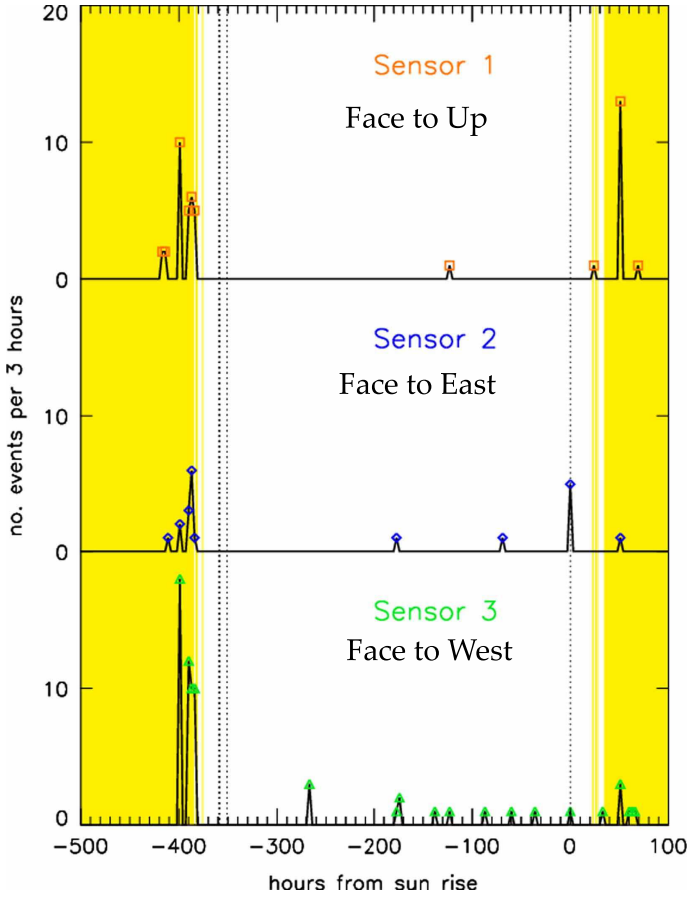

Fig. 4.14 Events recorded by the LEAM sensors per 3-hour during lunar night period [33]. Yellow shaded bars represent times of excessive heating and the dotted lines make the sunrise and sunset. Events recorded during times excessive heating were not correct for noise contribution.

a half angle of approximately 60°. The sensors have the same aperture with a length of L_{sensor} = 10 cm in the vertical direction. LEAM was directly placed on the lunar surface with a height of about 0.5 m. The number of potential ejecta events was calculated and the results for the sensors is shown in Table 4.1. The predicted number of falling ejecta is calculated based on measurement results of LDEX (see Equation 4.11). The predicted events of rising ejecta particles enter the aperture with positive angles and with speeds above 50 m·s^{-1} according to trigger methods. The falling ejecta with lower speeds can also trigger the individual sensors of the LEAM experiment if they carry enough surface charges. What should be noted is that the Up sensor can not record any rising ejecta due to its limited field-of-view. Therefore all potential ejecta grains for the Up sensor belong to the falling ejecta population with velocities lower than 2.4 km·s^{-1}.

Table 4.1 The number of potential ejecta events for the LEAM sensors. EA: Entry Angle; ED: Effective Distance and GS: Grains Speed. As the limit by filed of view, the Up sensor can not record any grains ejected directly from the lunar surface.

Detector	EA, θ(°)	ED, D(m)	GS, V(m·s^{-1})	N(s^{-1})
West	0 - 60	$\sim$ 10	$>$ 50	0.0031
	-60 - 0	-	50 - 2400	0.0053
East	0 - 60	$\sim$ 10	$>$ 50	0.0031
	-60 - 0	-	50 - 2400	0.0053
Up	0 - 60	-	50 - 2400	0.0053
	-60 - 0	-	50 - 2400	0.0053

Flux Predictions of LDX

Based on our simulations, the populations of rising and falling ejecta show different entry angle distributions. Hence, the mounting designs (e.g. height and facing direction) of the detector on the lunar lander influences the predicted measurements. The relationship between the detector facing direction and predicted number of events is shown in Figure 4.15. What should be noted here is that the viewing angles -90° and +90° are pointing directions to the sky and to the ground respectively. Since the rising ejecta have an angular distribution range from 5° to 65°, their measurements start at pointing directions of -40° and the events increase with rising pointing angle, which has a maximum value at 5°. The flux reduction of rising ejecta events is caused by decreasing sensitive area A. The measurements of rising ejecta will stop at a pointing direction of 65°. The falling ejecta mainly have an entry angle range from -60° to -40°. The measurements of falling ejecta start at the facing

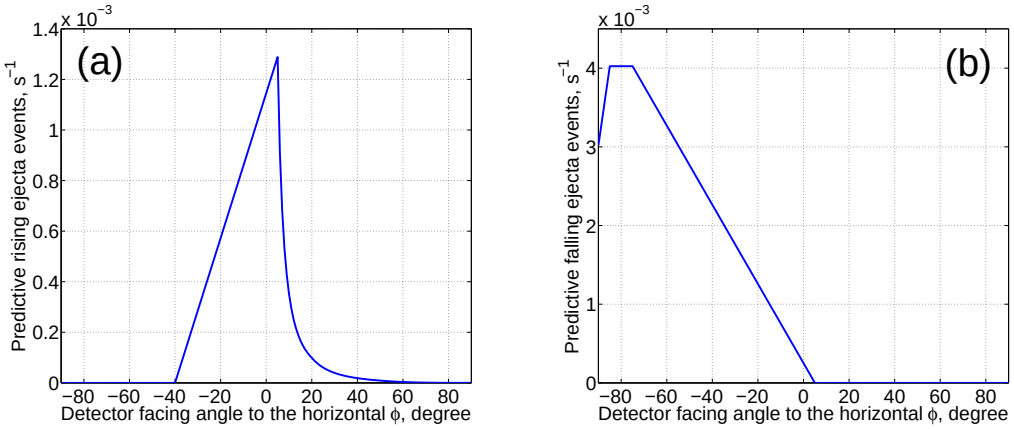

Fig. 4.15 Predictied ejecta events vary with detector pointing direction. (a) and (b) show the predicted flux for the rising ejecta population and the falling ejecta population, respectively. -90° and +90° are the viewing angles when detector faces to sky and ground respectively.

direction of -90° (facing to the sky), and stop at 5°. There is no limitation of facing area for the measurements of the falling ejecta.

The total predicted number of rising ejecta increases linearly with the height of the detector. Therefore the top side of the lander is better than the bottom side for the measurements of high speed ejecta ($v_{ejecta} > 1$ km·s^{-1}). The predicted number of detectable rising ejecta events varies with the mounting height of the detector as shown in Figure 4.16.

4.3.3 Detection of Lofted Dust

In this study, we assume the levitated dust flux on the lunar surface is isotropic and a plane with a FOV of 2π will get 1/3 of the total column density. Based on the following modeling results, the potential event number N_{lofted} of lofted dust for a dust detector mounted 3 meters above the lunar surface is determined by the horizon glow model:

$$N_{lofted} = \frac{1}{3} \cdot f(r,z) \cdot v_{max} \cdot A \cdot \frac{FOV}{2\pi} \tag{4.12}$$

$$= \frac{1}{3}\left(\int_{r_{min}}^{r_{max}} \frac{n_0}{r} exp\left(-\frac{r^{8/3}z}{2\times 10^{-15}}\right) \cdot \frac{\Phi}{r}\sqrt{\frac{6\varepsilon_0}{\rho_p}}dr\right) \cdot A \cdot \frac{FOV}{2\pi} \tag{4.13}$$

$$= 4.5 \times 10^4 s^{-1} \tag{4.14}$$

where $n_0 = 4.0 \times 10^5$ m^{-3}; $r_{min} = 0.1$ μm and $r_{max} = 6$ μm are the minimum and maximum radius of the dust; z is the height of the detector, $z = 3$ m; $A = 0.04$ m^2 is the open area.

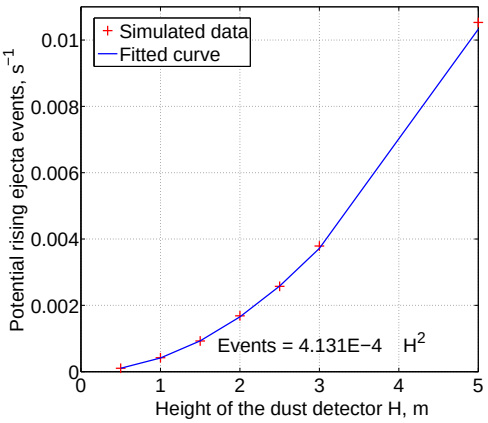

Fig. 4.16 Potential number of rising ejecta events and the mounting height of the dust sensor above the lunar surface

$FOV = \pi/4$ is the field of view of the detector; Φ is the surface potential, $\Phi = 50$ V; ε_0 is the vacuum space permittivity, 8.85×10^{-12} F·m^{-1} and ρ_p is the dust grain density, which was selected as 2.5 g·cm^{-3}.

The predicted event number for lofted dust based on the horizon glow model is so huge, such that it is still questioned by many scientists. The recent laboratory experiments indicate that the interaction of dust on the lunar surface with solar UV and plasma is more complex than previously thought [21, 80]. The simplification by Stubbs et al. [76] might not be an acceptable resolution when considering the latest results from LDEX. Comparing the simulation model described by Szalay and Horanyi [77], in the lunar sheath (0 - 3 meters above the lunar surface), the dust column density is about 10^3 m^{-3}. If we assume these dust grains have an average speed of 1 m·s^{-1}, the impact rate for LDX mounted at 3 m above the lunar surface is:

$$N_{lofted} = 10^3 \cdot \frac{\pi/4}{2\pi} \cdot 0.04 \cdot 1 = 5s^{-1} \tag{4.15}$$

Chapter 5

Future Mission Sensors

5.1 Chang'E 4 Lunar Lander and Yutu Rover

Chang'E 4 is a provisional name of a possible future lunar exploration mission, incorporating a robotic lander and a rover. Chang'E 4 will be China's third lunar lander mission after the sample return mission Chang'E 5 (by 2017). Following the successful landing of its twins (Chang'E 3), Chang'E 4 will try to land on the far side of the Moon within South Pole–Aitken basin area for the first time.

The Yutu rover has a mass of 136 kg with dimensions of 1.5 m $\times$ 1 m $\times$ 1.1 m with solar cells hold off. The rover has a payload capacity of about 20 kg. Energy of the rover is provided by its two solar panels for an operation only during lunar days. The lunar rover changes into sleep mode in the nighttime.

A dust detector onboard a lunar rover has several advantages: the measurements can

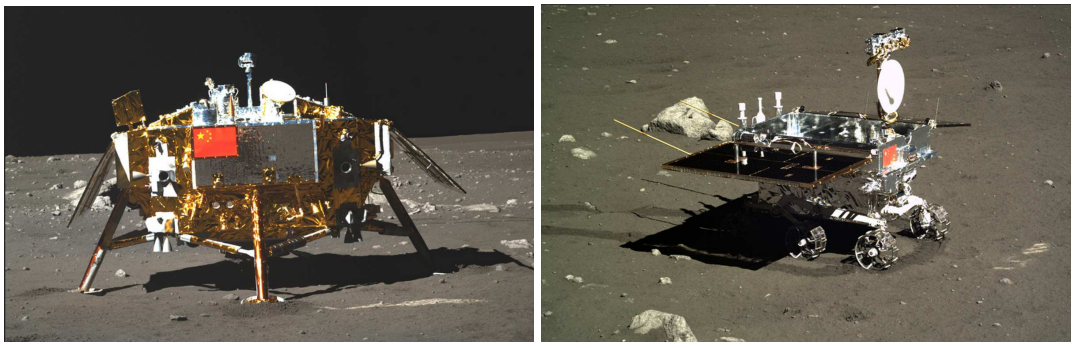

Fig. 5.1 Chang'E 3 lander and Yutu rover. Yutu rover snags a shot of its carrier lander (Left hand side) and Yutu rover was photographed by the Chang'E 3 lander (right hand side). Photos credited by Xinhua, China.

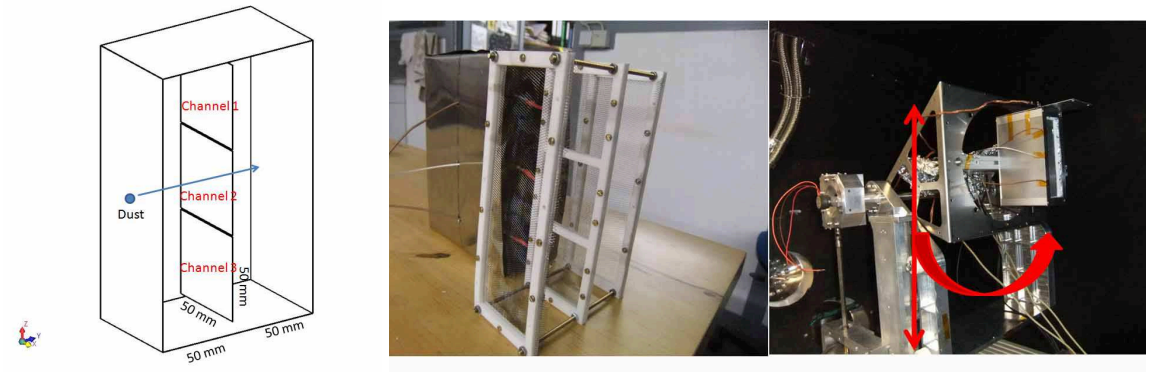

Fig. 5.2 Set up of 3-grid model at the accelerator. The moving platform has 3 degrees of freedom: (1) right ↔ left, (2) up ↔ down, and one angle to tilt in the vertical plane and with respect to the accelerator beam line.

be taken at different regions of the lunar surface. Furthermore, the sensor will monitor the interaction of the rover with the lunar dust environment (plasma, electric fields, and dust). The disadvantage is that such carriers provide very limited mass, power and data volume capacities for the payloads, a more simplified design of a dust trajectory sensor is required.

5.2 3 Grid Electrode Detector Concept

A design with only 3 gird electrodes was simulated and tested in this study. The developed detector contains two shielding grids at the aperture and a plane with three electrodes to measure induced charge signals (see Figure 5.2). All of the charged particles fly though the top regions of channel 2 for both, simulations and experimental studies. The electrodes used in this study are etched grid segments with a size of approximately 5 cm × 5 cm. The nylon frames produced by 3D printer technology were used to hold the grid electrodes.

The induced charge signals are similar with the results obtained by a single plane of the LDX design. Channel 2 give a peak pulse signal with 100% of particle primary charge, and the closest electrodes, channel 1, records a signal with two maxima. Figure 5.3 shows the induced charge signals of channel 1 normalized by the particle primary charge. The incident angles α varies from 0 degree to 32.4 degrees. Similar to LDX, the maxima decrease with the distance between particle entry position to the 'Nearby Segments'. The average values of the two maxima $Q_{alpha} = 0.5(Q1+Q2)$ is obtained by channel 1 related to the particle insertion position Z. Figure 5.4 shows the relationship between average value of induced charge maxima and different insertion positions Z. When dust particles fly through the same position, Q_{alpha} essentially remains constant with different incident angles. The value

of Q_{alpha} decreases with Z, which is the distance from center region (Z = 0 mm) to the edge of channel 2 (Z = 23 mm). The electrode of channel 1 can get up to 27.5% of particle primary charge at maximum. When particles fly through the middle area of channel 2, the induced charge obtained by channel 1 is only about 3% of the particle primary charge.

The relation between particle insertion position Z and the average induced charge Q_{alpha} of channel 1 is shown in Figure 5.5. Q_{alpha} has an exponential growth with increasing values of the particle insertion position Z. Equation 5.1 is the formula derived from Figure 5.5 providing a method to calculate particle insertion positions using obtained induced charge signals.

$$Z = 34.85 - 8.8 \times lg(Q_{alpha} - 0.1041) \tag{5.1}$$

Since this design employs 3 grid electrodes, it has only one plane to detect the particle position information, the trajectory calculation method of LDX using ΔX and ΔZ on different planes is not applicable here. Fortunately, it is obvious from Figure 5.3, that the first maximum of the induced charge signal recorded on channel 1 decreases with particle insertion position Z. Conversely, the secondary maximum increases with Z. This means that the ratio of two maxima k ($k = Q1/Q2$) contains particle incident angle information. The relationship between the ratio k and the particle incident angle α is shown in Figure 5.6, which varies with particle insertion position Z.

As shown by Figure 5.5 and Equation 5.1, the particle insertion position Z and the particle incident angle α can be obtained by analysing the average value Q_{alpha} and the ratio k of the two maxima of the signal recorded by the nearby segment. We can get the particle incident angle α by:

$$\alpha = f_1(Z) - f_2(Z) \times e^{\frac{k}{f_3(Z)}} \tag{5.2}$$

where, $f_1(Z)$, $f_2(Z)$ and $f_3(Z)$ are functions of the particle insertion position Z. These functions have no relationship with the particle entry angle.

$$f_1(Z) = 378.39 - 127.84 \times e^{\frac{Z}{44.67}} \tag{5.3}$$

$$f_2(Z) = 265.76 - 148.63 \times e^{\frac{Z}{46.82}} \tag{5.4}$$

$$f_3(Z) = 2.36 - 1.05 \times e^{\frac{Z}{40.43}} \tag{5.5}$$

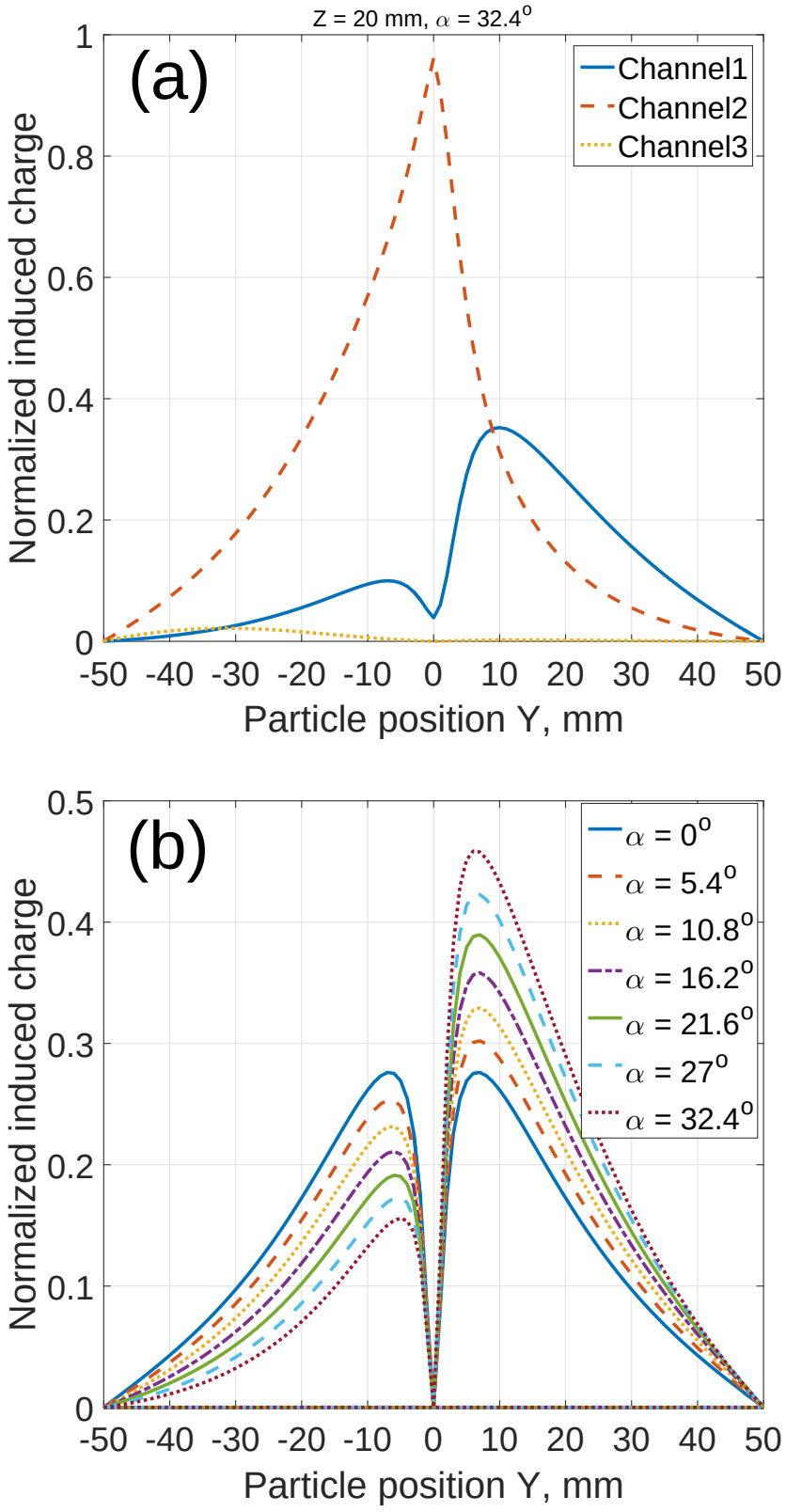

Fig. 5.3 Induced charge signals of a 3-grid electrodes detector. In the figure, (a) shows a typical signal when a dust grains flies through the insertion point $Z = 20$ mm and with an incident angle of 32.4 degrees; (b) shows the summary of signals obtained by channel 1 vary with incident angles α when dust grains fly through the same insertion point $Z = 20mm$.

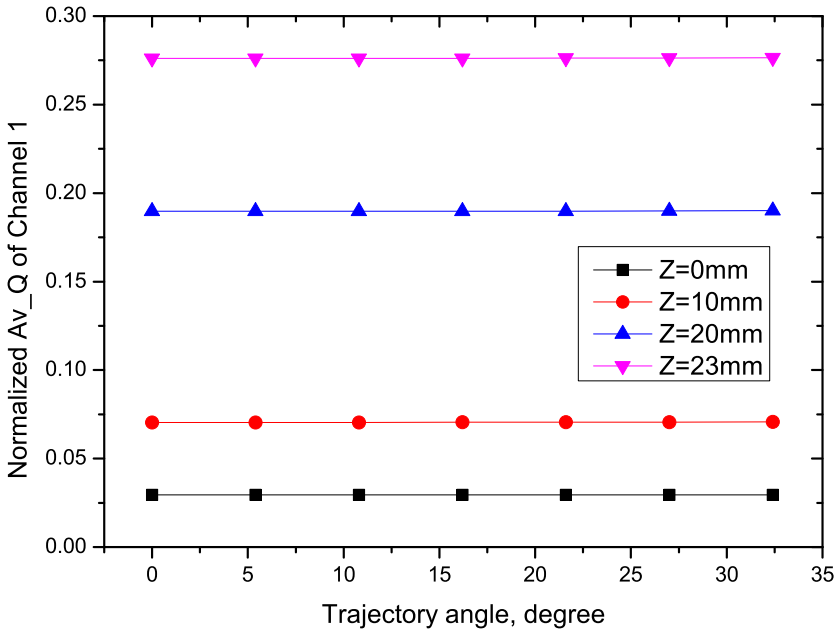

Fig. 5.4 Relationship between Q_{alpha} and the particle insertion position Z with different incident angles. The parameter $Z = 0$ is the middle of the channel 2, and $Z = 25$ mm is the edge of the channel 2.

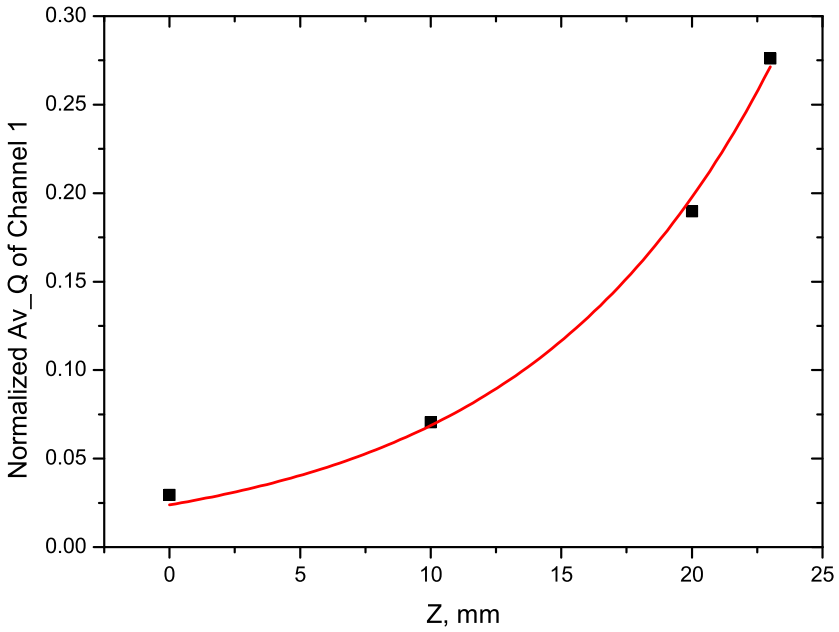

Fig. 5.5 Fitting curve for Q_{alpha} as function of particle insertion position Z. The black points are obtained by simulation, with the mean values of Q_{alpha} as shown in Figure 5.4, and the red line describes a fitting curve.

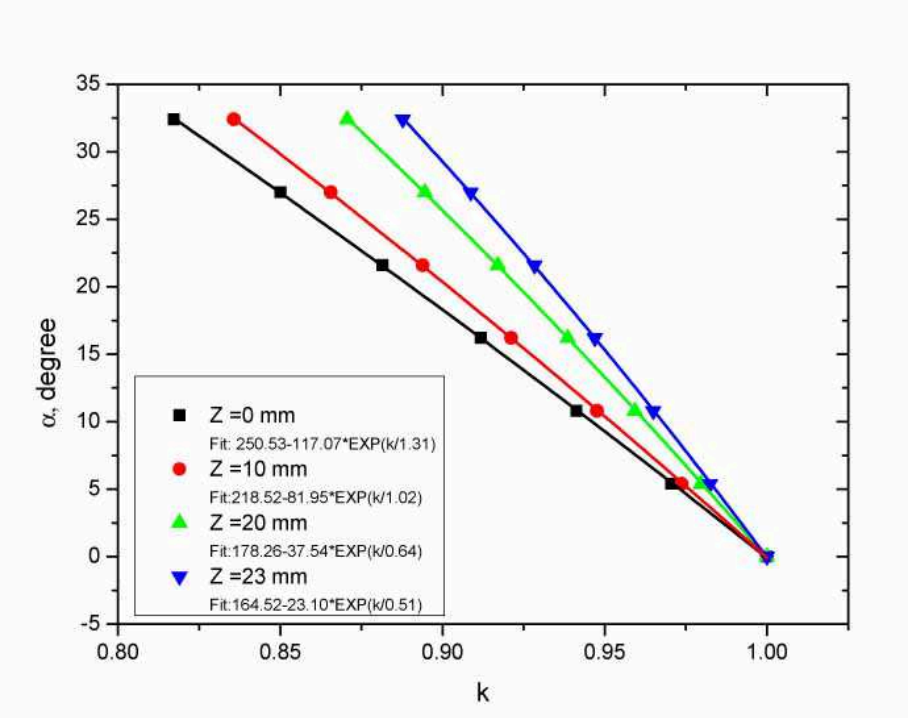

Fig. 5.6 Relationship between ratio k and particle incident angle α for different particle insertion positions Z.

Similar to LDX, the induced charge signal of channel 2, where particle passes through, contains 100% of the particle primary charge, and it also provides particle speed information. Particle entry position and incident angle are obtained by the signals of nearby segments in channel 1. In comparison to the LDX sensor, a single electrode array design can further reduce the mass and data requirement of the detector for some small payload exploration missions.

5.3 Rover Platform Sensor Concepts

Based on our simulation and experimental results, a single plane electrodes detector can also obtain the charge, speed and trajectory information of individual charged particles with high accuracies. Therefore we developed two further simplified designs with less number of electrodes and lower instrument mass with respect to the original LDX design: the cylindrical design (LDX-c) and the square design (LDX-s), which are shown in Figure 5.7 and Figure 5.8, respectively.

There are 7 channels to address particle charge, speed and trajectory information in LDX-c, including four surrounding electrodes, one central circular electrode and two trigger

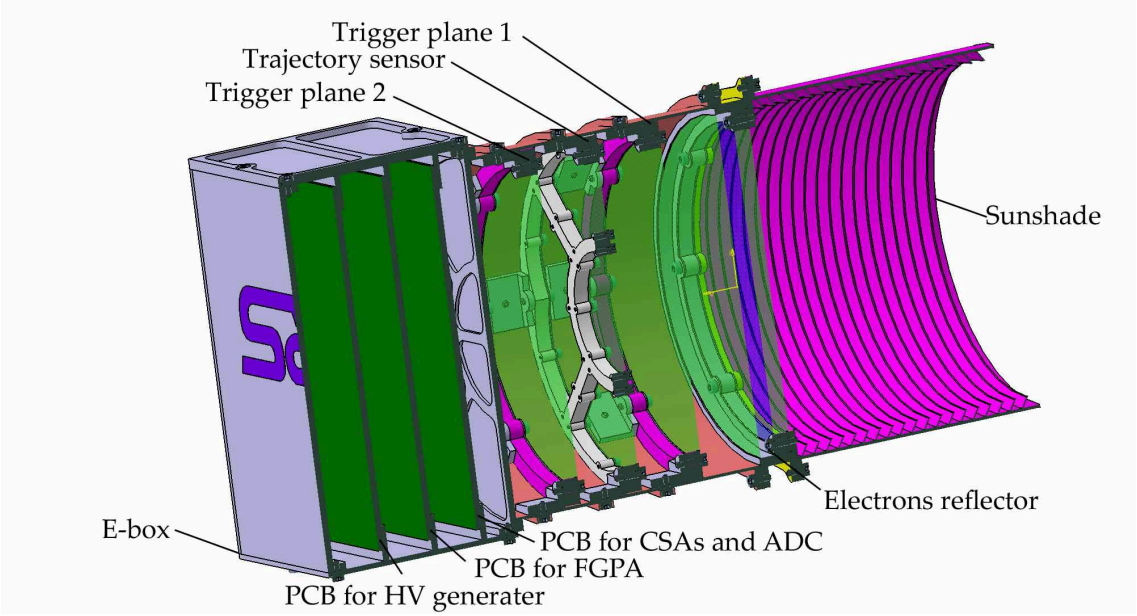

Fig. 5.7 Cross-sectional view of the LDX-c design including the main structure, sunshade, and the electronic box.

grid electrodes (see Figure 5.7). A sunshade is added to limit the direct or reflected UV light during the daytime operations, which causes photoelectron noise measured by the charge sensitive amplifiers. The additional electron reflector system has two grounded grids and one negatively charged grid to shield the solar wind and the lunar surface plasma environment. The corresponding instrument parameters are shown in Table E.1.

LDX-s has four parallel stripe electrodes in the center and two trigger grid electrodes. One potential application of LDX-s is to detect the interaction of the lunar rover and the lunar surface, in the cases when dust grains mainly move in vertical direction. The sensor also has an electron reflector system to avoid the background plasma noise. The corresponding instrument parameters are shown in Table E.1. The measurement accuracy for the particle charge of these two new designs is similar to LDX (better than $\pm 5\%$). However, the trajectory accuracy might slightly decrease by 2 degrees.

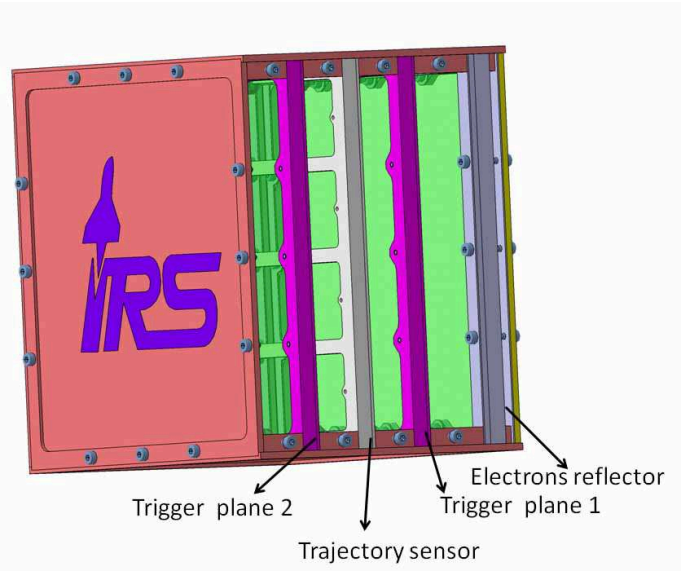

Fig. 5.8 Mechanical structure of LDX-s. The electronics box is on another side of the housing, which is not visible in this figure.

Chapter 6

Summary and Outlook

6.1 Summary

The Moon is a dynamic and complex body. In recent decades, there is a steadily increasing international interest in lunar exploration. Multiple lunar missions were launched by various countries and agencies, which were mainly orbiters. An increasing number of scientists are planning the future exploration of the Moon with both robotic and manned methods allowing us to study important questions for science and exploration. There are several open issues which must be addressed in order to ensure acceptable costs and risks for a sustained human exploration of the Moon. Arguably, one of the highest-priority issues is the characteristics of the lunar dust.

The main goal of this work is to develop, simulate, build and test the design of a dust detector to meet the requirements for future lunar lander missions. Such detectors should have high accuracies for the measurement of particle charges, speeds and trajectories. Furthermore, the primary purpose of the expected ESA lunar lander mission is to test the landing technology, the spacecraft can only offer very limited mass, power and data volume for the payloads. These limitations add challenges for the design of a dust detector.

The interplanetary dust particles (IDPs), impact ejecta and levitated dust are the three main components of the dust environment above the lunar surface. Each year, the Moon is bombarded by about 10^6 kg of interplanetary micrometeoroids of cometary or asteroidal origin. They may excavate the lunar soil with a yield of up to 1000 times of their own mass. Such grains launching from the impact location are called impact ejecta. Surface charging by solar UV light and by solar wind plasma of small atmosphere-less bodies like our Moon or of asteroids, leads to electrostatic fields above the surface, especially around the terminator. The lunar fines are thought to be electrostatically charged and are naturally

transported under the influence of near-surface electric fields. They are called levitated or lofted dust.

The current knowledge on the lunar dust environment is based on a rare set of observations. Different physical processes were proposed to explain the optical and in-situ measurements. The flux and mass distribution of IDPs has been deciphered [35, 48] by the analysis of craters on the lunar rock samples during Apollo missions. Currently, the Lunar Dust EXperiment (LDEX) sensor onboard the lunar orbiter Lunar Atmosphere and Dust Environment Explorer (LADEE) identified the existence of a dust cloud above the lunar surface. The impact ejecta launched from the lunar surface are thought to be the main component of the dust cloud. However, LDEX didn't find any evidence of the levitated dust.

Transport phenomena range from the levitation of micron-sized dust grains at low altitudes (centimeter to meter height), to the lofting of sub-micron particles to tens of kilometers. Observations by the Apollo astronauts of sticking dust to their space suits after only short extravehicular activities demonstrated the importance of dust contamination control. Simple instruments placed on the lunar surface monitored both, natural and man-made dust coverage as well as cleaning effects.

To answer the scientific questions about the lunar dust environment, the three populations of dust grains (IDPs, ejecta and levitated dust) have to be measured and distinguished. The speeds of levitated dust are lower than the speed thresholds of dust detectors using impact ionization, particle momentum, capacitor discharge or target penetration. The charge induction method was therefore selected for solution to address the lunar dust environment.

Before the development of a new design, the previously designed charge induction detectors were re-evaluated. The two existing detector designs using charge induction techniques, the Dust Trajectory Sensor (DTS) and the Cosmic Dust Analyser (CDA), both can measure the charge, speed and trajectory of charged dust grains. The COULOMB software package was used to analyse the advantage and disadvantage of these two designs. By employing an array of metal wire electrodes, the DTS-like design has a finer spatial resolutions to determine the particle trajectory ($\pm 1^{\circ}$) and speed ($\pm 10\%$). But a DTS-like detector is limited in particle charge detection with a relatively high uncertainty of up to 40%. Another disadvantage of DTS is that the long and thin wire electrodes are relatively fragile, which might be destroyed by hyper-velocity impacts. Furthermore, the detector needs 64 analog front-end amplifiers, which increases the mass and power and which leads to an unnecessary big data set.

CDA onboard the Cassini mission detected for the first time electrostatic charges carried

by the dust particles in interplanetary space. Its design employs only one charge sensitive amplifier leading to a very low sensor mass, power and data volume. CDA also provides rather high accuracies in particle charge values. However, the electrode is a large grid with a related high capacitance of approximately 220 pF such that the noise level is as high as 1 fC. It is therefore impossible to obtain high accuracies for the dust trajectory and speed values for small and weakly charged particles.

Considering the known advantages and disadvantages of the two existing sensor designs, a new sensor based on charge induction method was developed. The sensor Lunar Dust eXplorer (LDX) measures the charge, speed and trajectory of dust grains above the lunar surface with relatively high accuracies. In contrast to the former described sensors, the LDX design uses an array of grid electrodes. The benefit is a reduced number of electronic channels which simplifies the electronics and therefore the mass and power of a space instrument. By analyzing the data of all electrodes, the particle trajectory can be derived with an accuracy of $\pm 2^{\circ}$. Another advantage of the grid electrode based design of LDX is the detection of nearly 100% of the dust particle primary charge in each electrode plane. This value is more than twice as high as for a detector using individual wires. Furthermore, the signals are highly symmetric and the amplitudes in each plane are equal which allows for the means of digital filters in future instruments. Especially the detection of low speed particles (< 1 km$\cdot$s^{-1}) will benefit from this process.

The mounting geometry of the detector affects its final measurement results. Based on our results, the impact ejecta are likely candidates to explain the results of the LEAM sensors. Due to the high measurement thresholds of LEAM, a more detailed data analysis is difficult. A newly designed trajectory sensor mounted on a lunar lander, e.g. LDX, would be a powerful tool to study the lunar dust environment and new instrumentation would also further constrain the interpretation of LEAM. A sensor mounted on the lander instead of standing on the lunar surface has more chances to measure the high-speed component of the ejecta population.

6.2 Outlook

During this work, a laboratory model of the design of LDX was developed, simulated, built and tested at the dust accelerator. It has high accuracies for the measurement of particle charges (better than $\pm 5\%$), speeds (better than $\pm 10\%$) and trajectories (better than $\pm 2^{\circ}$). In addition to LDX, we developed two further sensor designs using grid based electrodes (LDX-c and LDX-s). The goal is a further reduction of complexity, of instrument mass

and power in order to allow measurements on smaller landers or even rovers. The lunar environment with its wide speed range of moving dust particles is a challenge for the triggering of dust sensors. Former missions like Galileo, Ulysses, Cassini or LDEX used impact ionization of fast particles with speeds typically above 1 km·s^{-1} to generate the required signal which was used for triggering.

On the lunar surface there are also high speed interplanetary dust particles and ejecta grains which can generate enough impact charge. However, there are also levitated dust particles and ejecta grains with speeds as lower as a few meters per second. Such low velocities are not sufficient to cause a reliable impact charge signal which is required for sensitive triggering. Therefore the trigger scheme has to be completely revised for applications in the lunar surface environment. We propose a digital triggering system and advanced filter methods using our symmetric set of electrodes. Related development activities have been started and are very promising [10].

Another challenge is the required high sensitivity to measure small or only weakly charged dust grains. The currently developed laboratory model has an approximate charge threshold of 1 fC. A major problem for a high signal-to-noise is the proper electrical shielding of the sensor electrodes and the overall grounding scheme of the front-end electronics and detector setup. Dust particles with a radius of 1 μm and a typical surface potential of 1 V carry only 700 electrons. This charge of 0.11 fC is very low and can only be reliably measured using low detector capacitances and sensitive charge amplifiers. Furthermore, the connection between the electrodes and the front-end electronics is a critical part. A high integration, extensive shielding and grounding with short electrical connections is necessary in order to ensure the required sensitivity of 0.1 fC. Future designs have to be highly integrated and might use even ASICs to account for the high sensitivity and large bandwidth.

Although LDX was developed for the scientific requirements of a lunar mission, such a system can be employed in any environment to monitor low fluxes of dust particles with a broad speed range between a few m·s^{-1} and many km·s^{-1}. Possible science targets include interplanetary missions focused on the measurement of interplanetary dust or planetary dust (rings). A specific advantage of LDX-like trajectory sensors is their ability to be compatible with other types of dust detection systems. A combination with momentum sensors, impact ionization sensors or even mass spectrometers is possible and would enable us to measure both, the trajectory and composition of individual dust particles in space.

Appendix A

Impact Simulation

A.1 Autodyn Software Tool

The excellent abilities for modeling nonlinear dynamics of solids, fluids, gas, and their interaction [3], make Auodyn to be an explicit analysis tool for hypervelocity impact studies. The mesh-free particle solvers (Smooth particle hydrodynamic, SPH), and its multi-solver with finite elements (FE) provided by Autodyn are ideally suited for the computation of high velocities, large deformations, fragmentation and structural dynamics. The software has a user-friendly graphical user interface window combining pre-processor, solver, and post-processor (see Figure A.1).

A.2 Material Models

The following discussion can be found in the user manual of the AUTODYN software [3].

The application of the laws of mass, momentum and energy, and as well as the appropriate initial and boundary conditions are indispensable to solve a dynamic material problem. A material model demands equations that relate stress to deformation and internal energy (or temperature). Autodyn separates the total stress tensor into a hydrostatic pressure (all three normal stresses equal) and a stress deviatoric tensor associated with the resistance to shear distortion. Equation of state (EOS) is the relationship between the pressure, density and specific energy (or temperature) of matter. EOS can be determined from knowledge of the thermodynamic properties of the material. However, in practice, the only practical way of obtaining data on the behavior of the material at high strain rates is to carry out well-characterized dynamic experiments. It is important to recognize that, since the relationship

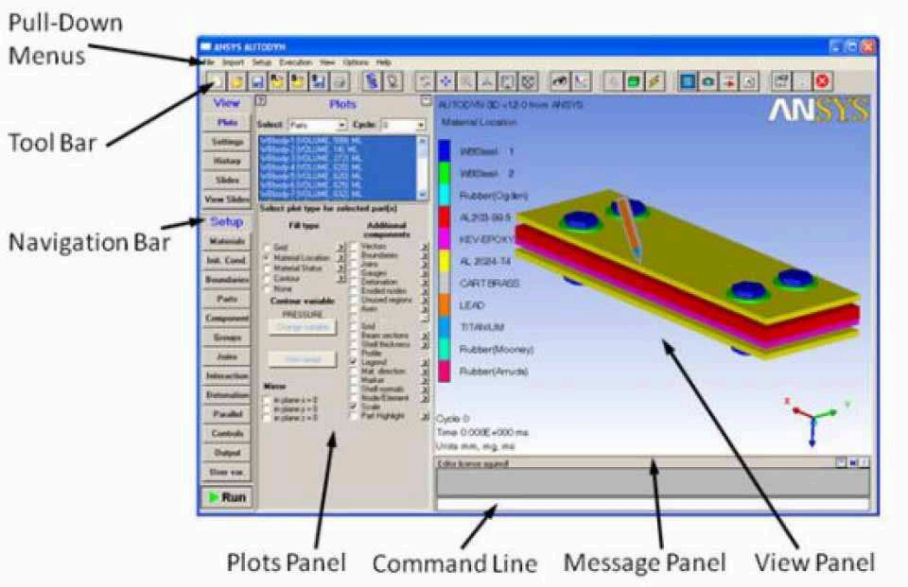

Fig. A.1 Autodyn program window.

is required for use in a numerical code, an analytic form is chosen to facilitate a solution. Such an analytic form is at best an approximation to the true relationship. Further, the equation of state may be given in extensive tabular form and in that case the analytic form chosen can be considered as an interpolation relationship. Meanwhile, the deviatoric stress tensor describes the material's resistance using a strength model. Thus, the EOS and the strength model gives the volumetric and the distortional changes of a material subjected to load respectively. Depending on the type of material and the characteristics of the loads in the problem, different types of EOS and strength models are used. Finally, a criteria for failure of the material is also needed [36].

In considering the behavior of the materials in AUTODYN, viscosity, heat conduction and deviation of the medium from thermodynamic equilibrium (at any instant and any point) is neglected. In this case, at each instant and each point in a fluid, there is a definite state of thermodynamic equilibrium defined by [3]:

p hydrostatic pressure
p_H Hugonoit pressure
ρ density
ρ_0 initial density
v specific volume = $1/\rho$
v_0 initial specific volume = $1/\rho_0$

μ compression = $\rho\rho_0$-1
e specific internal energy
e_H Hugonoit energy
S specific entropy
i specific enthalpy = e + pv
T temperture
c velocity of sound
c_0 initial velocity of sound

The Rankine-Hugoniot equations for the shock jump conditions can be regarded as defining a relation between any pair of the variables density ρ, pressure p, specific internal energy e, shock wave velocity U and the material speed behind the shock u_p. Based on dynamic experiment results, U and u_p have a linear relationship as [3]:

$$U = c_0 + s_1 u_p + s_1 u_p^2 \tag{A.1}$$

For most material, it can be simplified as:

$$U = c_0 + s_1 u_p \tag{A.2}$$

Then the Mie-Gruneisen form of EOS is established as:

$$p = p_h + \Gamma\rho(e - e_h) \tag{A.3}$$

where

$$p_h = \rho_0 c_0^2 \mu(1+\mu) \tag{A.4}$$

$$\mu = \rho/\rho_0 - 1 \tag{A.5}$$

$$\Gamma(Gruneisen \quad Gamma) = v\left(\frac{\partial p}{\partial e}\right)_v \tag{A.6}$$

$$e_h = \frac{1}{2}\frac{p_h}{\rho_0}\left(\frac{\mu}{1+\mu}\right) \tag{A.7}$$

The Piecewise JC strength model is one if the modifications of Johnson-Cook model. The dependence on effective plastic represented by a piecewise linear function of yield stress

Y versus effective plastic strain ε_0. Johnson-Cook model normal used for representing the strength behavior of material within large strains, high strain rate and high temperatures due to high velocity impact and explosive detonation. The yield stress Y is defined as [3]:

$$Y = \left(A + B\varepsilon_p^n\right)\left(1 + C\ln\varepsilon_p^*\right)\left(1 - T_H^m\right) \tag{A.8}$$

where ε_p is the effective plastic strain. ε_p^* is the normalized effective plastic strain rate. T_H is the homologous temperature, T_H = (T - T_{room})/(T_{melt} - T_{room}). In Piecewise JC strength model, the strain rate dependence and thermal softening terms is the same as in the Johnson-Cook model. The term $\left(A + B\varepsilon_p^n\right)$ is replaced by a piecewise linear function of yield stress Y versus effective plastic strain ε_0.

Although AUTODYN can calculate with both Lagrangian and Eulerian grids, it may sometimes be the case that materials have to be defined using Lagrangian grids even though it is clear that these materials will be subjected to very large distortions arising from gross motion of the Lagrange grid. Target and projectile material in hypervelocity impact problems will be subject to gross distortion and again an accurate calculation of this problem should follow the material as it "splashes". In both examples calculations using an Euler grid suffer unless an accurate interface tracking routine is used and so one defines the problem using a Lagrange grid [3].

Table A.1 Copper material model parameters.

Equation of State	**Shock**	Eff. Plastic Strain #1	0.3
Reference density	8.9 (g/cm^3)	Eff. Plastic Strain #2	1.0E+20
Gruneisen coefficient	2.0	Yield Stress #1	4.5E+11 (mPa)
Parameter C1	3.958E+06 (mm/s)	Yield Stress #2	4.5E+11 (mPa)
Parameter S1	1.497	Ther. Soft. Exponent	1
Reference Temperature	300 (K)	Melting Temperature	1.0E+20 (K)
Specific Heat	1.0E-06 (uJ/kgK)	Ref. Strain Rate (/s)	1
Strength	**Piecewise JC**	**Erosion**	**Geom. Strain**
Shear Modulus	4.64E+13 (mPa)	Erosion Strain	300
Yield Stress	1.20E+11 (mPa)	Type of Geo. Strain	Instantaneous

In this thesis, the CONC-35MPA material model was selected to simulate the lunar surface and the dust grains.

Herrmann's P-alpha model [39] gives the correct behavior at high stresses but at the same time provides a reasonably detailed description of the compaction process at low stress levels [3].

This form of the P-alpha model used in Autodyn is as follows:

$$p = \left(\frac{1}{\alpha}\right) f\left(\frac{v}{\alpha}, e\right) \tag{A.9}$$

where the factor $1/\alpha$ was included to allow for their argument that the pressure in the porous material is more nearly $1/\alpha$ times the average pressure in the matrix material.

The RHT Concrete model is an advanced plasticity model for brittle materials developed by Riedel, Hiermaier and Thoma of Ernst Mach Institute. It is particularly useful for modeling the dynamic loading of concrete. It can also be used for other brittle materials such as rock and ceramic [3, 66].

The RHT constitutive model is a combined plasticity and shear damage model in which the deviatoric stress in the material is limited by a generalized failure surface of the form:

$$f(P, \sigma_{eq}, \theta, \dot{\varepsilon}) = \sigma_{eq} - Y_{TXC(P)} \star F_{CAP(P)} \star R_{3(\theta)} \star F_{RATE(\dot{\varepsilon})} \tag{A.10}$$

The fracture surface is represented through the expression:

$$Y_{TXC} = f_c^{'} \left[A_{fall} \left(P^* - P^*_{spall} F_{rate} \right)^{N_{fall}} \right] \tag{A.11}$$

where $f_c^{'}$ is the cylinder strength, A_{fall} and N_{fall} are user defined coefficients, P^* is pressure normalized with respect to $f_c^{'}$, P^*_{spall} is the normalized hydrodynamic tensile limit, F_{rate} is a rate dependant enhancement factor.

The RHT model can represent the difference between the compressive and the tensile meridian in terms of material strength using the third invariant J_3 dependence term (R3). The rate Q_2 is used to describe reduced strength on shear and tensile meridians. The load angle θ describes stress triaxiality and depends on the third invariant J_3. This can be utilized to represent the observed reduction in strength of concrete under triaxial extension, compared with triaxial compression. The input parameter $Q_{2.0}$ defines the ratio of strength at zero pressure, and the coefficient BQ^*_p defines the rate at which the fracture surface transitions from approximately triangular in form to a circular form with increasing pressure. The third invariant dependence term is formulated using the expression [3, 66]:

$$R_3 = 2(1 - Q_2^2)cos\theta + (2Q_2 - 1)\sqrt{4(1 - Q_2^2)cos^2\theta - 4Q_2} \tag{A.12}$$

$$cos3\theta = \frac{3\sqrt{3}}{2}\frac{J_3}{J_2^{3/2}} \tag{A.13}$$

$$Q_2 = Q_{2.0} + B_p^* \tag{A.14}$$

Strain rate effects are represented through increases in fracture strength with plastic strain rate. Two different terms can be used for compression and tension with linear interpolation being used in the intermediate pressure regime. α and δ are two input parameters.

For the compression case, where hydrostatic pressure above $f_c/3$,

$$F_rate = 1 + \left(\frac{\dot{\varepsilon}}{\dot{\varepsilon}_0}\right)^{\alpha} \tag{A.15}$$

For the tension case, where hydrostatic pressure below $f_t/3$,

$$F_{rate} = 1 + \left(\frac{\dot{\varepsilon}}{\dot{\varepsilon}_0}\right)^{\alpha} \tag{A.16}$$

Strain hardening is represented in the model through the definition of an elastic limit surface and a 'hardening' slope. The elastic limit surface is scaled down from the fracture surface by user defined ratios: $(f_{c,el}/f_c)$ and $(f_{t,el}/f_t)$. For pressure below $f_{t,el}/3f_t$, the elastic scaling function $F_{elastic}$ take the value $f_{t,el}/f_t$ and when the value above $f_{c,el}/3f_c$, it is equal to $f_{c,el}/f_c$ [3, 66].

$$Y_{hard} = Y_{elastic} + \frac{\varepsilon_{eq}^{pl}}{\varepsilon_{eq}^{pl,hard}}\left(Y_{fail} - Y_{elastc}\right) \tag{A.17}$$

$$\varepsilon_{eq}^{pl,hard} = \frac{\left(Y_{fail} - Y_{elastc}\right)}{3G}\left(\frac{G_{elastic}}{G_{elastic} - G_{plastic}}\right) \tag{A.18}$$

Damage is assumed to accumulate due to inelastic deviatoric straining (shear induced cracking) using the relations:

$$D = \sum \frac{\Delta\varepsilon_{pl}}{\varepsilon_p^{fail}} \tag{A.19}$$

$$\varepsilon_p^{fail} = D_1\left(P^* - P_{spall}^*\right)^{D_2} \tag{A.20}$$

where D_1 and D_2 are material constants used to describe the effect strain to fracture as a

function of pressure.

Table A.2 CONC-35MPA material model parameters.

Equation of State	**P alpha**	Shear Strength (fs/fc)	0.18
Reference density	2.75 (g/cm^3)	Failure Surface Constant A	1.6
Porous density	2.314 (g/cm^3)	Failure Surface Exponent N	0.61
Porous sound speed	2.92E+06 (mm/s)	Meridian Ratio (Q)	0.68
Initial comp. pressure	2.33E+10 (mPa)	Brittle to Ductile Transition	0.0105
Solid comp. pressure	6.0E+12 (mPa)	G (elas.)/(elas.-plas.)	2.0
Compaction exponent	3.0	Elastic Strength / ft	0.70
Solid EOS	Polynomial	Elastic Strength / fc	0.53
Bulk Modulus A1	3.527E+13 (mPa)	Strength Constant B	1.6
Parameter A2	3.958E+13 (mPa)	Strength Exponent M	0.61
Parameter A3	9.04E+12 (mPa)	Strain Rate Exp. Alpha	0.032
Parameter B0	1.22	Strain Rate Exp. Delta	0.036
Parameter B1	1.22	Max. Fracture Strength Ratio	1.0E+20
Parameter T1	3.527E+13 (mPa)	Use CAP on Elastic Surface?	Yes
Parameter T2	0 (mPa)	**Failure**	**RHT Concrete**
Reference Temperature	300 (K)	Damage Constant, D1	0.04
Specific Heat	6.54E+08 (uJ/kgK)	Damage Constant, D2	1.0
Thermal Conductivity	0 (uN.um/mKs)	Minimum Strain to Failure	0.01
Comp. Curve	Standard	Shear Modulus Fraction	0.13
Strength	**RHT Concrete**	Tensile Failure	Hydro (Pmin)
Shear Modulus	1.67E+13 (mPa)	**Erosion**	**Geom. Strain**
Comp. Strength (fc)	3.5E+10 (mPa)	Erosion Strain	2.0
Tensile Strength (ft/fc)	0.1	Type of Geo. Strain	Instantaneous

Appendix B

Laboratory Signals

In this appendix, the figures show the experimental induced charge signals obtained by gird electrodes of the design of LDX, which are similar with the results shown in Section 3.3.2. Each figure shows the signals of 6 channels. The front-bottom group is for Plane A (three channels) and the backward group is for Plane B (three channels) (see Figure 3.1).

The incident angles α change from 0 degree to 27 degrees with a spacing of 5.4 degrees. When a charged particle flies through an array of electrodes, two types of induced charge signals are created with one maximum or two maxima.

The signals of the directly crossed segments have only one maximum and lead to amplitudes of 100% of the particles primary charge. They are called 'Main Segment'. Since the maximum values and the peak positions of the signals remain unchanged on these main segments, they can be used to determine the charge and velocity of the particle. Another type of signals has two maxima which appear on segments. They are closest segments to the insertion points on the main segments and are called 'Neighbor Segment'. The two maxima of neighbor segments show opposite change with the particle incident angle.

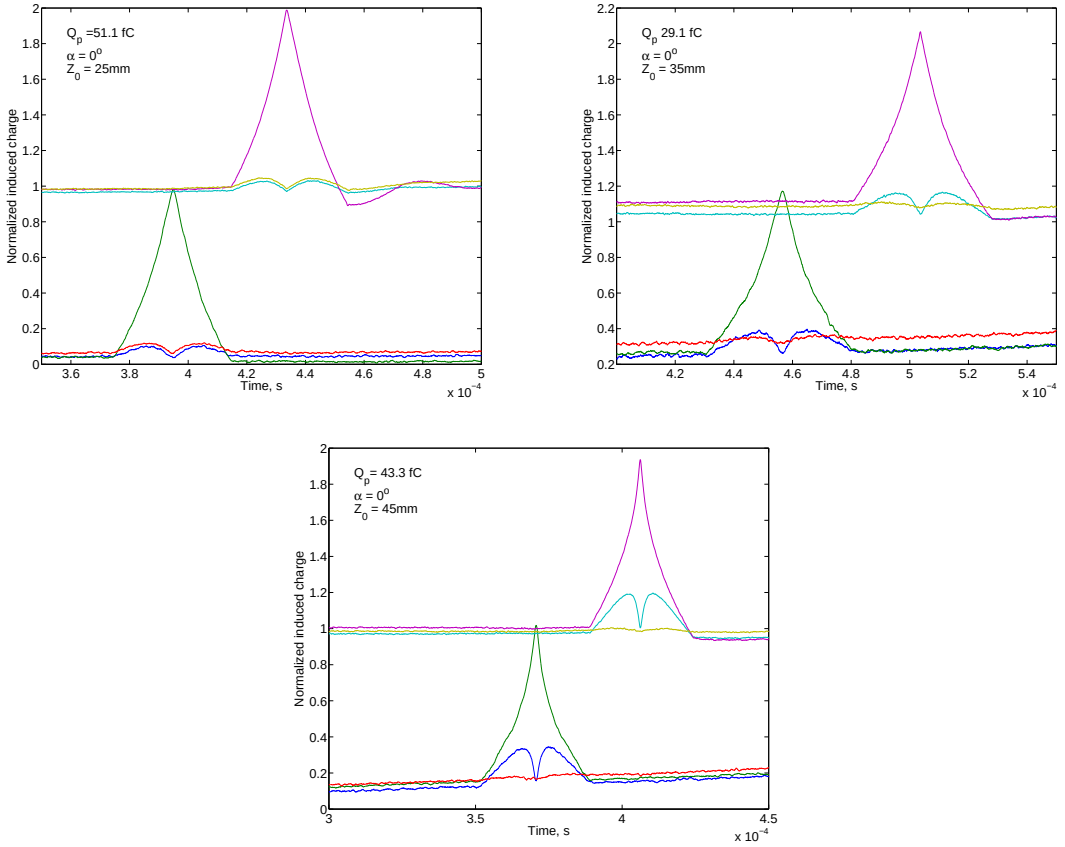

Fig. B.1 Signals for different entry positions with a trajectory of 0°. Q_p is the primary charge of particle; α is the particle incident angle in Z direction and Z_a is the entry position on Plane A.

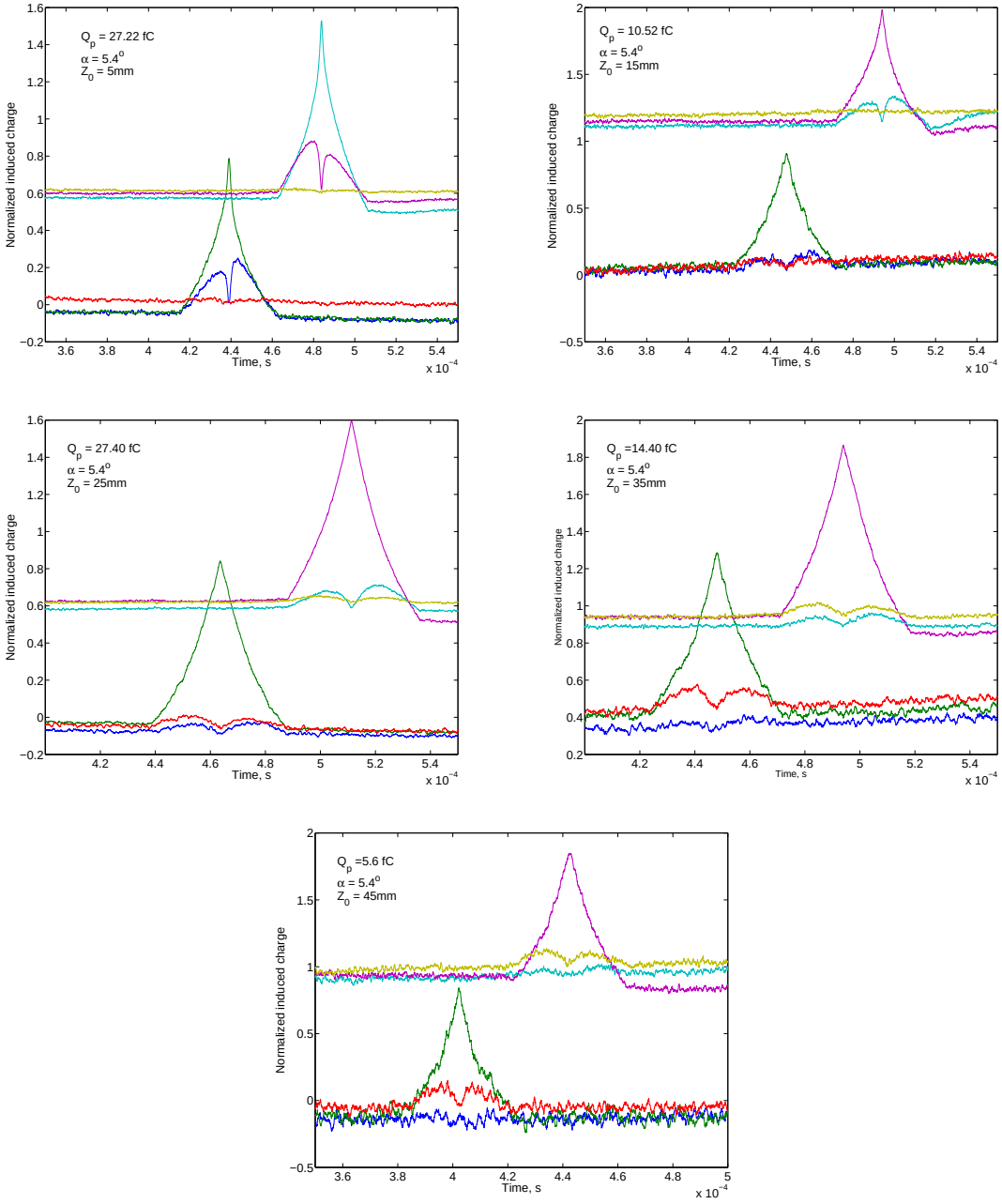

Fig. B.2 Signals for different entry positions with a trajectory of 5.4°. Q_p is the primary charge of particle; α is the particle incident angle in Z direction and Z_a is the entry position in Plane A.

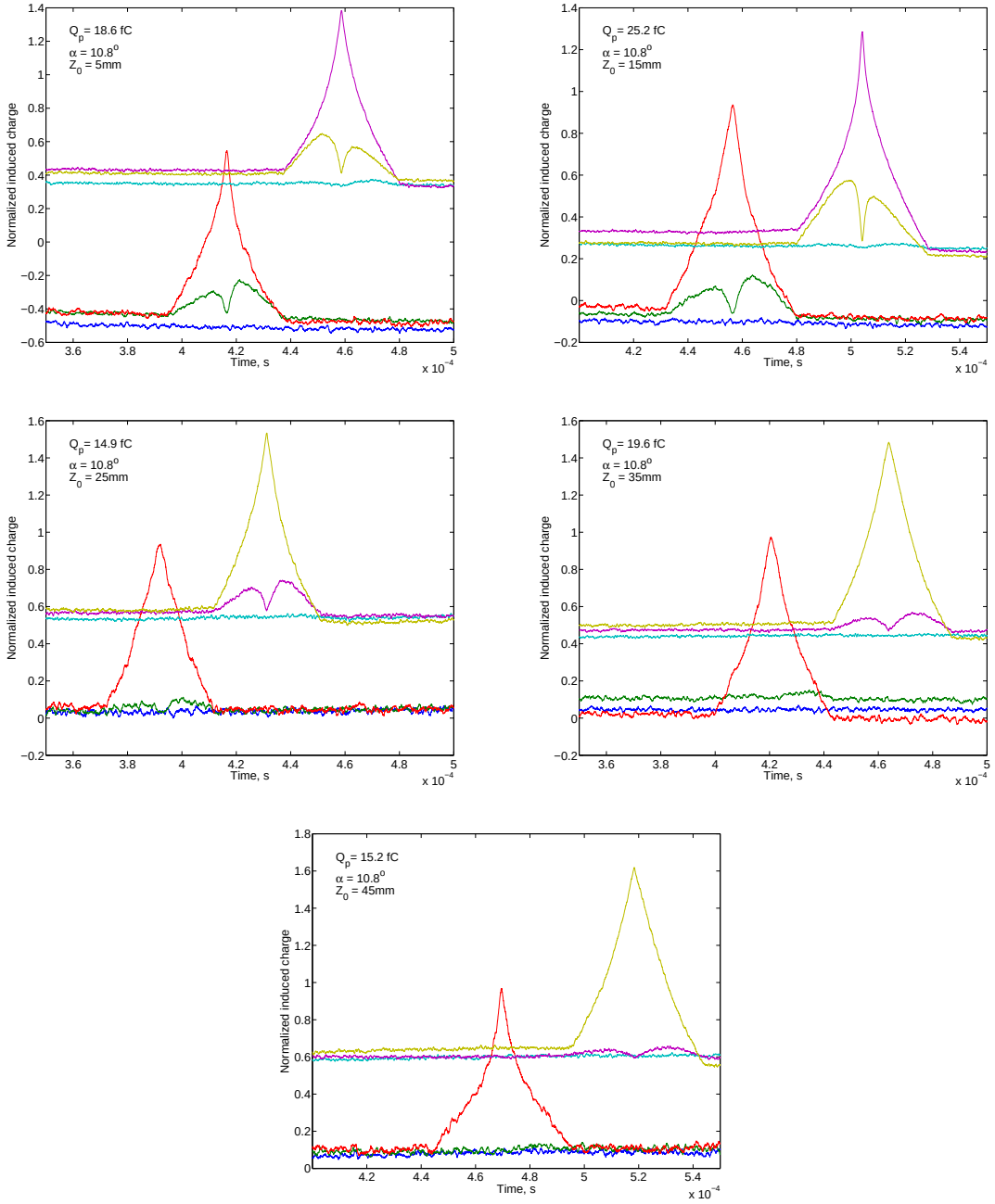

Fig. B.3 Signals for different entry positions with a trajectory of 10.8°. Q_p is the primary charge of particle; α is the particle incident angle in Z direction and Z_a is the entry position in Plane A.

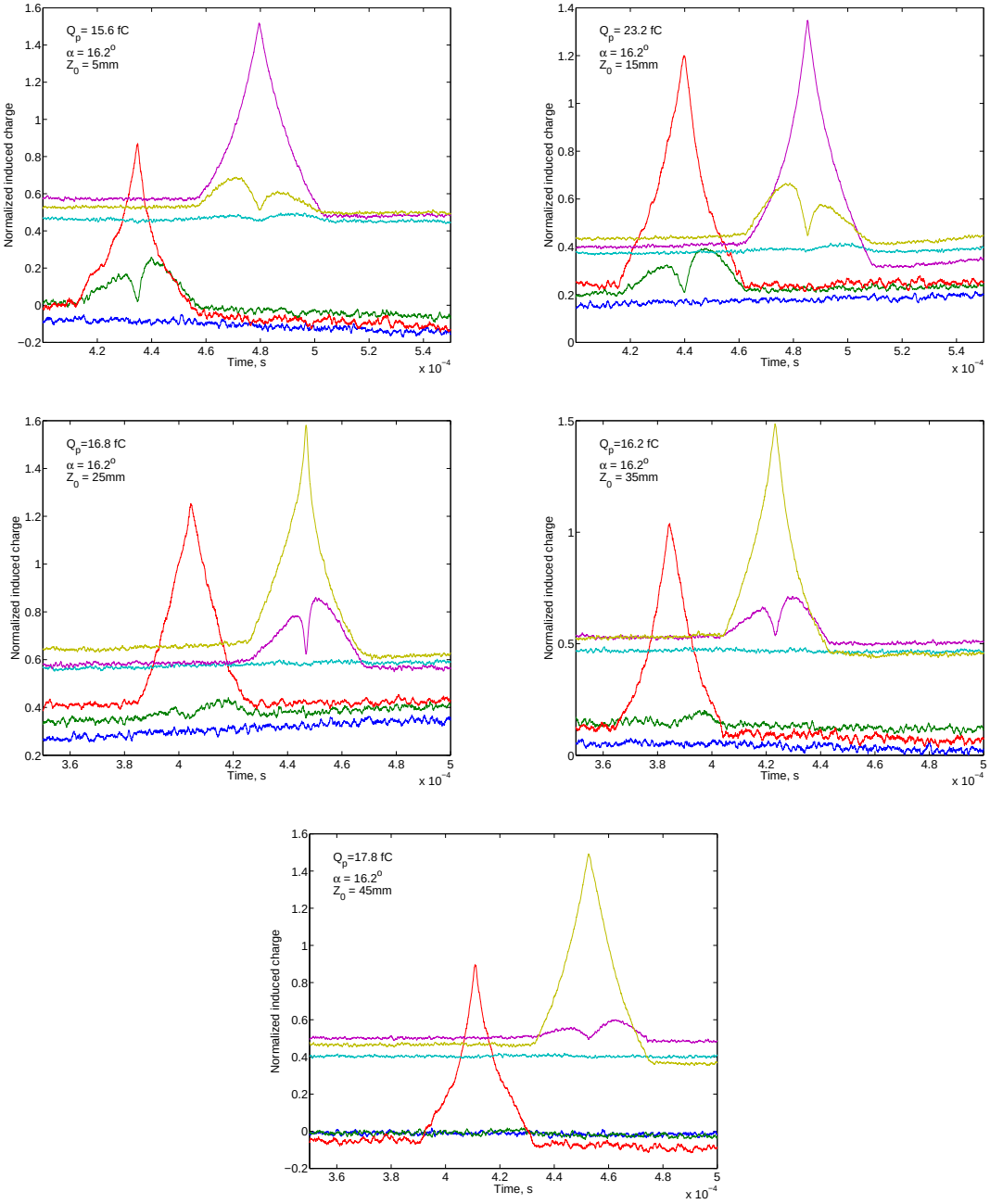

Fig. B.4 Signals for different entry positions with a trajectory of 16.2°. Q_p is the primary charge of particle; α is the particle incident angle in Z direction and Z_a is the entry position in Plane A.

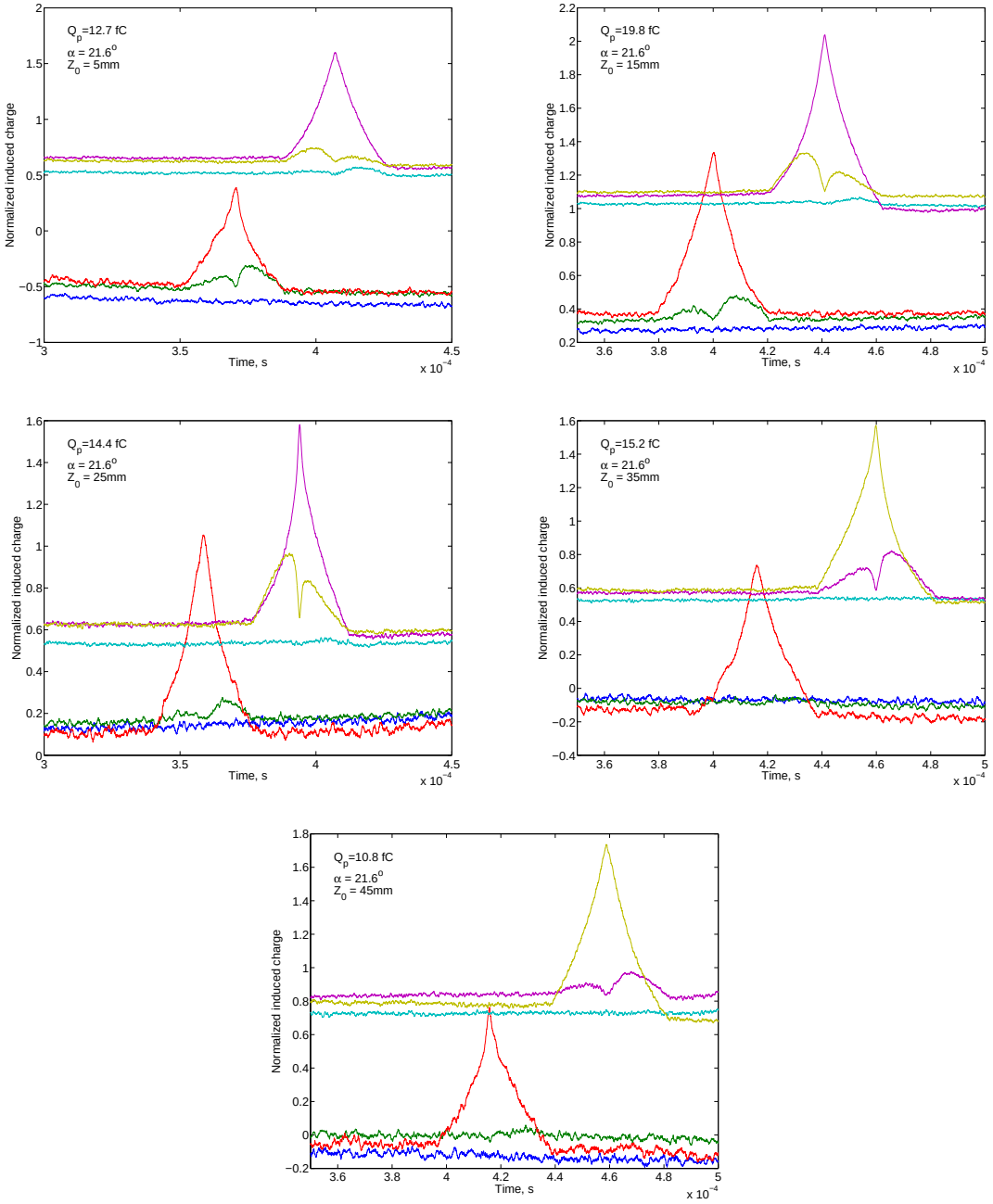

Fig. B.5 Signals for different entry positions with a trajectory of 21.6°. Q_p is the primary charge of particle; α is the particle incident angle in Z direction and Z_a is the entry position in Plane A.

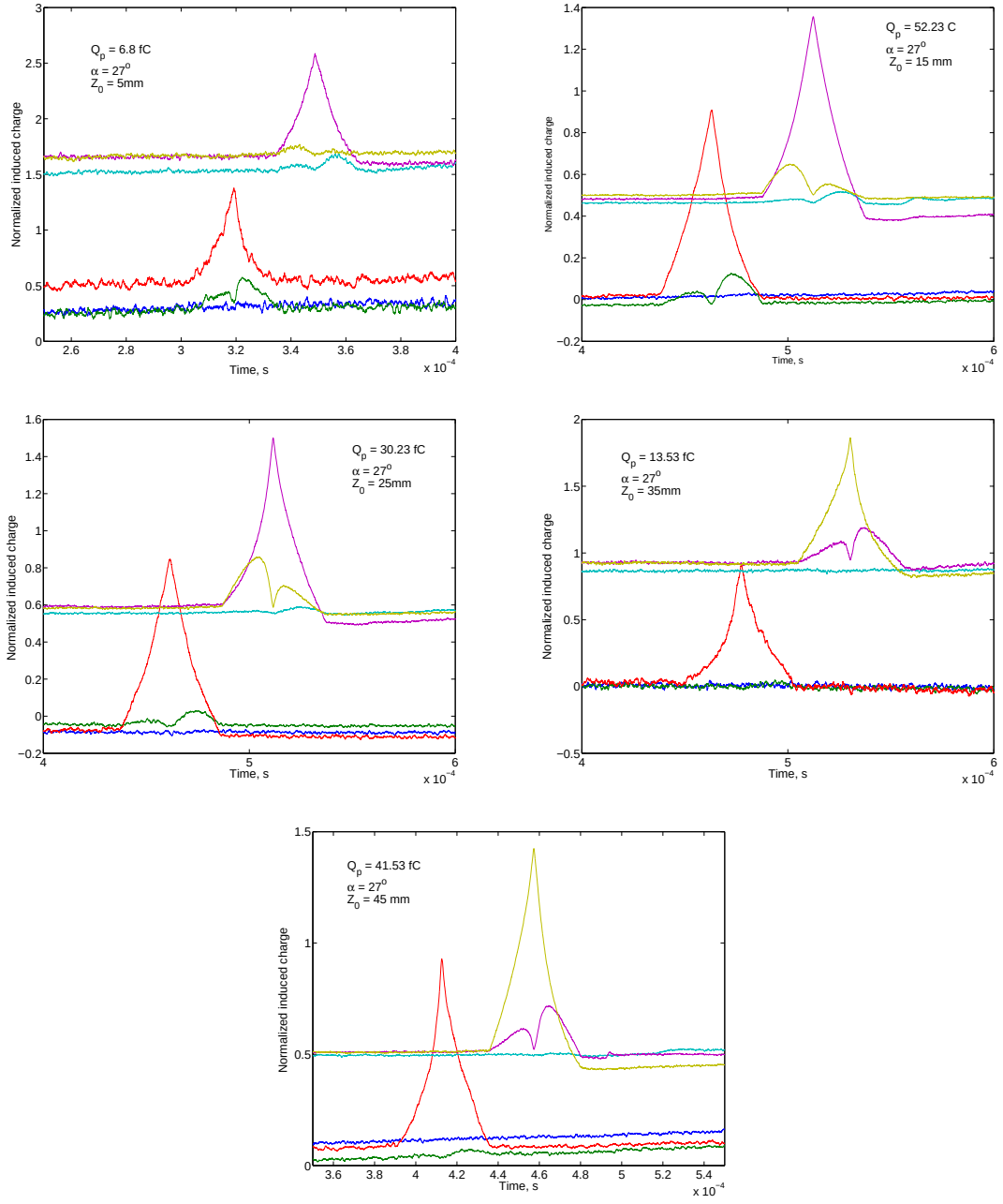

Fig. B.6 Signals for different entry positions with a trajectory of 27°. Q_p is the primary charge of particle; α is the particle incident angle in Z direction and Z_a is the entry position in Plane A.

Appendix C

Simulation of Charge Induction

COULOMB is a CAE software package designed to perform full 3D electric field simulations of quasi-static physical systems. The following discussion can be found in the user manual of the COULOMB software [71].

COULOMB provides a wide variety of anality to create contour plots and graphs of field quantities. Macroscopic parameters such as surface charge, torques and capacitances can also be calculated. To perform a simulation using COULOMB, first a geometric model of the physical system must be constructed. This can be done by using the built in geometric modeler. Once the geometric model has been built, physical properties (such as boundary conditions, materials, source, etc.) have to be assigned. After the physical properties have been assigned, the model is then discretized and the solution is calculated by the field solver . The dimensions of elements required depend on two main factors: (1) The choice of the numerical field solver method for performing the simulation. The default solver type is the Boundary Element Method (BEM). A Finite Element Method (FEM) solver is also available. (2) The nature of the physical properties assigned to the model. For example, the types boundary conditions, material properties, and source will influence the type of elements needed.

Depending on the model, BEM simulations may utilize elements of all three dimension numbers. At first, it may appear that FEM is simpler, since only 3D elements are used. However, solving electromagnetic problems using FEM usually requires an artificial truncation of the model space by a user created boundary box, and requires some experience to produce a correct field solution. For these reasons, we used BEM for the simulation in this thesis. An additional advantage of using BEM is that it does not require meshing either of free space regions, or of volumes composed of linear conductive or dielectric materials. Figure C.2 shows several important features of the COULOMB program window.

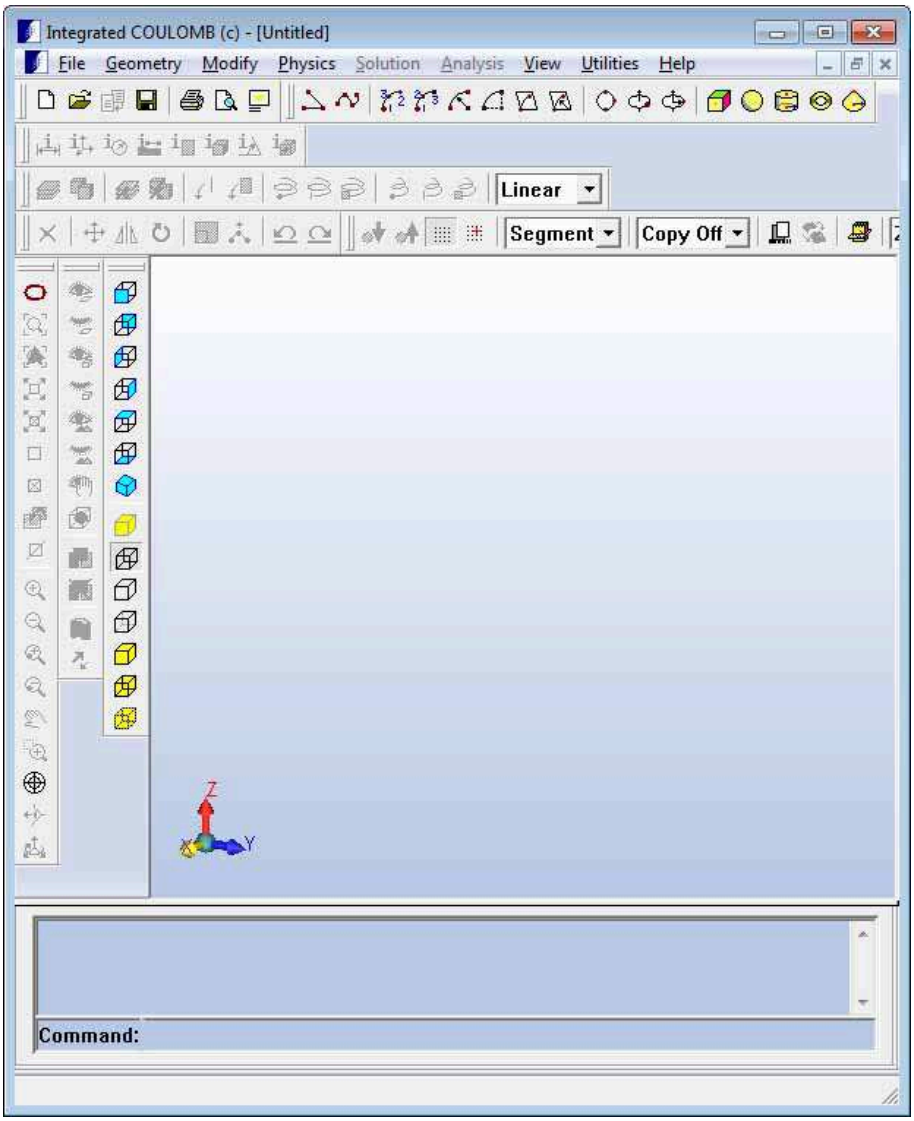

Fig. C.1 COULOMB program window.

The BEM uses only 2D elements on the surfaces which are the material interfaces or assigned boundary conditions. Therefore, users can set up a problem quickly and easily. Since only elements on interfaces are involved in the solution procedure, problem modifications are also easy. For example, in motor design optimization, solutions are required for different rotor positions. Using BEM software, only one boundary element distribution is necessary to solve all the rotor positions, and no element reassignments are required. With FEM software, finite elements in the whole space must be regenerated for

every new rotor position. Complete 3D Finite Element meshes are impossible to visually represent and comprehend on a 2D drawing.

The Boundary Element Method solves (analyses) field problems by solving an equivalent source problem. In the case of electric fields, it solves for equivalent charge, while in the case of magnetic fields, it solves for equivalent currents.

BEM also uses an integral formulation of Maxwell's Equations, which allows for very accurate field calculations. Unlike FEM, the electric and magnetic fields are computed directly from the source. This technique produces accuracies not attainable by Finite Element Method.

BEM allows all field variables at any point in space to be obtained very accurately. Also, the results are more precise because the integration operation is inherently more accurate than FEM's differentiation operation. Moreover, the unknown variables used in INTEGRATED's software are the equivalent currents or equivalent charges. These variables have real physical meanings. By using these physical variables, global quantities such as forces, torque, stored energy, inductance, and capacitance, among others, can be accurately obtained through some very simple methods.

The analysis of unbounded structures (e.g. electromagnetic fields exterior to an electric motor) can be solved by BEM without any additional effort because the exterior field is calculated the same way as the interior field. The field at any point in space can be calculated (even at infinity). Therefore, for any closed or open boundary problem, INTEGRATED's software users need only to deal with real geometry boundaries. In contrast, open boundary problems are problematic for FEM since artificial boundaries, which are far away from the real structure, must be used. How to determine these artificial boundaries becomes a major difficulty for FEM-based software applications. Since most electromagnetic field problems are associated with open boundary structures, BEM naturally becomes the best method for general field problems.

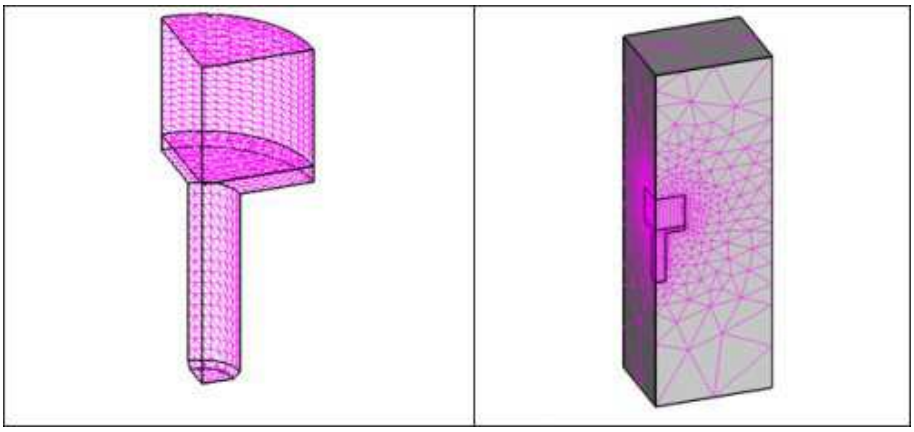

Fig. C.2 Comparison between BEM and FEM methods. (Left) Permanent Magnet and Pole Piece modeled using BEM. No artificial boundary box or meshing of open regions is required. (Right) Permanent Magnet and Pole Piece modeled using FEM. A boundary box to limit the model space is required, as is meshing of the entire simulation space [71].

Appendix D

Lunar Properties

D.1 Formation of the Moon

The Moon is the only natural satellite of Earth. The Moon is thought to have formed nearly 4.6 billion years ago, similar to the Earth. Although there have been several hypotheses for the origin of the Moon in the past, most of scientists accept the explanation that the Moon formed from the impact debris left over after a giant impact between Earth and a sprayed molten rock [37].

D.2 Surface Geology

When looking up the Moon from Earth with the unaided eye, the surface of the Moon we can see is called 'near side', which is divided into light areas (Lunar Highlands) and darker areas (Maria). Highlands have high altitude than Maria. There are craters both on Maria and Highlands, and the crater density on Highland is higher than Maria. The far side of the Moon is the side, which people can not see from earth [17, 82]. Maria cover about 17% of the lunar surface, but most of them exist on the near side of the Moon. The far side of the Moon is mostly covered by craters [82].

D.3 Impact Craters

The Moon was subjected to intense bombardment by meteorites and the craters vary from micron-sized [35] to hundreds of kilometers in diameter [82]. Most of these projectiles range from 10 nm to about 1 mm in size and impact the Moon at 10 - 72 $km \cdot s^{-1}$ speed.

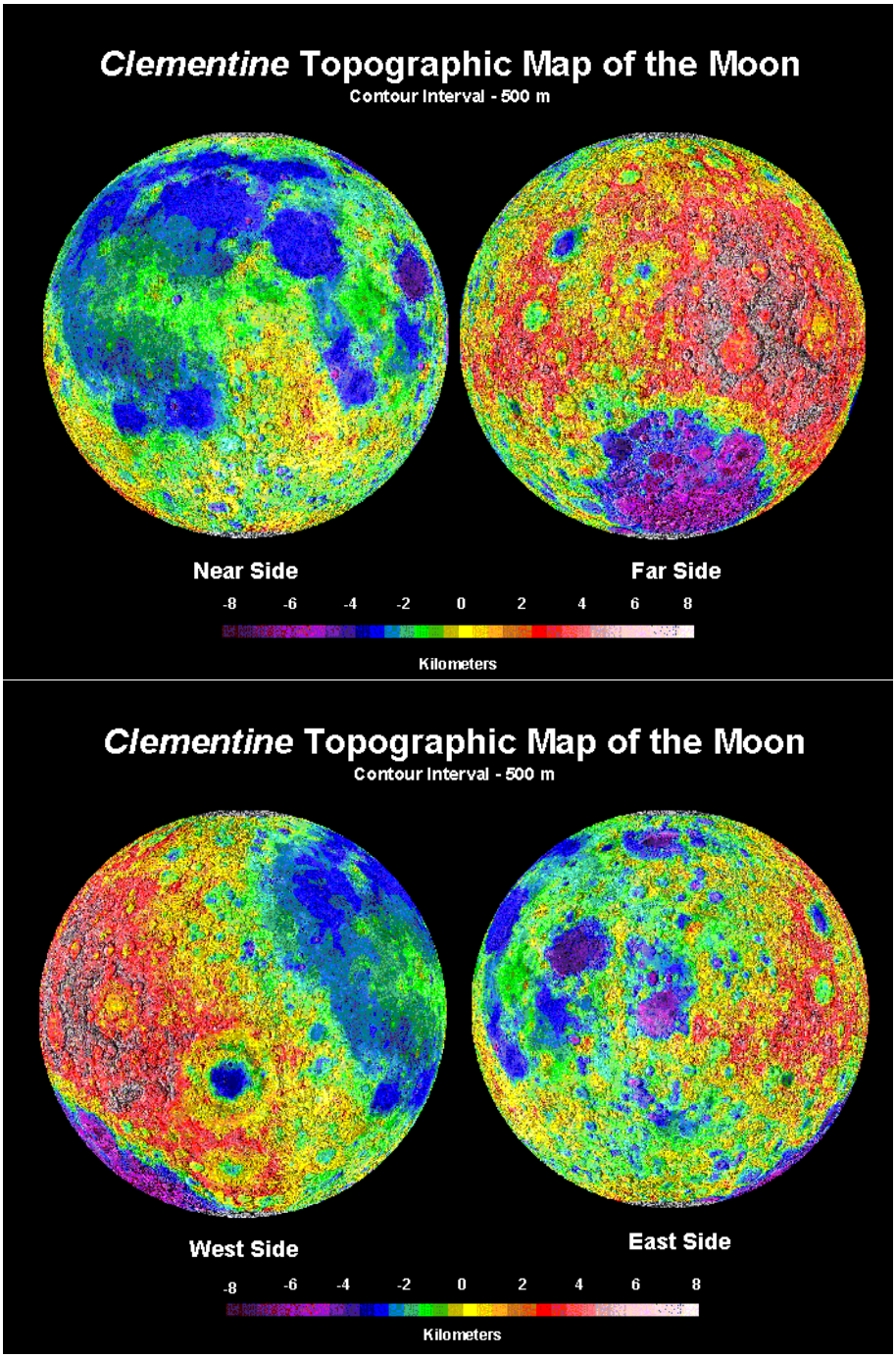

Fig. D.1 The laser altimetry images of Clementine spacecraft showing the lunar surface. Top image showing the near and far sides of the moon and bottom image showing the west and east sides of the moon. red = high, purple = low. Image processing by Brian Fessler and Paul Spudis, LPI.

Table D.1 Characteristics of the Moon.

Characteristics	Values
Average distance from Earth	384,400 km [82]
Mean Diameter	3,476 km [82]
Surface area	3.8×10^7 km^2
Volume	2.2×10^{10} km^3
Mass	7.35×10^{22} kg [82]
Mean density	3.34 g·cm^{-3} [82]
Surface gravity	1.622 m·s^{-2}
Escape velocity	2.38 km·s^{-1} [82]
Rotation period (Sidereal)	27.3 d [82]
Rotation period (synodic)	29.5 d [82]
Orbital velocity	1.08 km·s^{-1} [82]
Surface Temperature (day)	130°C [82]
Surface Temperature (max)	-184°C [82]

They may excavate lunar soil about mostly 1000 times their own mass [34]. The majority of ejecta that separates from the Moon's bedrock will fall back to the lunar surface and form as the lunar regolith.

Appendix E

LDX-like Instrument Parameters

E.1 Data Handling

The total number of channels using in LDX is 18, each with 10 bit resolution and a buffer depth of 8 ksamples. Additionally, the target channel has 10 bits and 1 ksamples. The raw data of one event are uncompressed 1.48 Mbits. A lossless compression by a factor 3.5 leads to 424 kbits.

For scientific data transmission an Universal Asynchronous Receiver/Transmitter (UART) with a data rate of 115200 bit/s is used. Considering the start, parity, and stop bits, the UART gives an user data rate of 83.7 kbit/s. The transfer of the data from one event with loss-less compression requires 5 seconds transmission time. After this time the sensor is ready again to wait for the next event.

E.2 Parameters and Operations

The main parameters of LDX and LDX-like designs (LDX-s and LDX-c) are shown in Table E.1.

The instrument shall operate continuously during dusk/dawn phases. The duty cycle between the burst data rate and the nominal data rate is 30% and 70%. The instrument shall operate during night for a period of 30 minutes, every 2 hours or at least 10 times during longer darkness phases. The relationship between plasma conditions and particle charging conditions is investigated at different time phases. All operations are carried out at low-noise environment without sun light in the field of view of the detector.

Table E.1 Parameters of three different types of LDX-like designs.

Sensor	Parameters	part name	Value
LDX	Open area		400 cm^2
	Mass	House structure	781 g
		fastener	36 g
		E-box	384 g
		SUM	1200 g
	Voltage	CSAs	12 V
	Power	CSAs (18)	1.1 W
LDX-s	Open area		100 cm^2
	Mass	House structure	340 g
		fastener	15 g
		E-box	330 g
		SUM	685 g
	Voltage	CSAs	12V
	Power	CSAs (6)	0.36 W
LDX-c	Open area		80 cm^2
	Mass	House structure	265 g
		fastener	10 g
		E-box	330 g
		Sunshade	100 g
		SUM	705 g
	Voltage	CSAs	12V
	Power	CSAs (7)	0.42 W

References

[1] Anderson, B. J., 1994. Natural orbital environment guidelines for use in aerospace vehicle development. NASA Technical Memorandum 4527, 13(1–10).

[2] Anderson, J. L. B., Schultz, P. H., Heineck, J., 2003. Asymmetry of ejecta flow during oblique impacts using three-dimensional particle image velocimetry. J. Geophys. Res. 108, 13(1–10).

[3] ANSYS, I., 2013. ANSYS Autodyn user's manual (Release 15.0). ANSYS, Inc.

[4] Auer, S., 1975. Two high resolution velocity vector analyzers for cosmic dust particles. Rev. Sci. Instrum. 46, 127–135.

[5] Auer, S., 1982. Imaging by dust rays: A dust ray camera. Opt. Acta. 29 29, 1421–1426.

[6] Auer, S., 2001. Interplanetary Dust. Springer, Ch. Instrumentation, pp. 385–444.

[7] Auer, S., 2007. Low-noise amplifier for measuring dust charges in the presence of plasama and uv radiation. Workshop on Dust in Planetary System (ESA SP-643), 231–233.

[8] Auer, S., Grün, E., Kempf, S., Srama, R., 2008. Characteristics of a dust trajectory sensor. Rev. Sci. Instrum. 79, 084501(1–7).

[9] Auer, S., Grün, E., Srama, R., Kempf, S., Auer, R., 2002. The charge and velocity detector ofthe cosmic dust analyzer on cassini. Planet. Sapce. Sci. 50, 773–779.

[10] Auer, S., Lawrence, G., Grün, E., Henkel, H., Kempf, S., Srama, R., Sternovsky, Z., 2010. A self-triggered dust trajectory sensor. Nucl. Instrum. Methods A622, 74–82.

[11] Basha, T. S., Abbas, A., 1988. Charging times for dust particles in plasma. Eur. J. Phys. 10, 151–156.

[12] Bean, A. L., 1970. Apollo 12 preliminary science report. NSAS SP-235.

[13] Berg, O. E., Richardson, F. F., 1969. The pioneer 8 cosmic dust experiment. NSAS TN D-5267, 1–9.

[14] Berg, O. E., Richardson, F. F., 1973. Lunar Ejecta and Meteorites experiment. In: Apollo 17 preliminary science report NSAS SP-330, 16(1–9).

[15] Berg, O. E., Richardson, F. F., Rhee, J. W., Auer, S., 1974. Preliminary results of a cosmic dust experiment on the moon. Geophy. Res. Lett. 1, 289–290.

[16] Berg, O. E., Wolf, H., Rhee, J., 1975. Lunar soil movment registered by the apollo 17 cosmic dust experiment. In:Interplanetary Dust and Zodiacal Light, Lecture Note in Physic 48, 233–237.

[17] Byrne, C. J., 2007. The far side of the Moon. Springer.

[18] Christoffersen, R., Lindsay, J. F., Noble, S. K., Lawrence, J. A., 2009. Lunar dust effects on spacesuit systems-insights from the apollo spacesuits. NASA/TP-2009-214786.

[19] Collier, M. R., Hills, H. K., Stubbs, T. J., Halekas, J. S., 2011. Lunar surface electric potential changes associated with traversals through the Earth's foreshock. Planet. Space Sci. 59, 1727–1743.

[20] Collier, M. R., Stubbs, T. J., 2009. Neutral solar wind generated by lunar exospheric dust at the terminator. Jour. Geo. Res. 114, A01104(1–10).

[21] Colwell, J., Robertson, S., Horányi, M., Wang, X., Poppe, A., Wheeler, P., 2009. Lunar dust levitation. J. Aerosp. Eng. 22, 2–9.

[22] Colwell, J. E., Batiste, S., Horányi, M., Robertson, S., Sture, S., 2007. Lunar surface: Dust dynamics and regolith mechanics. Reviews of Geophysics 45 (2), RG2006(1–26).

[23] Cottini, C., Gatti, E., Giannelli, Rozzi, G., 1955. Minimum noise pre-amplifier for fast ionization chambers. Nuovo Cimento 31, 473–483.

[24] Dietzel, H., Eichhorn, G., Fechtig, H., Grün, E., Hoffman, H. J., Kissel, J., 1973. The heos 2 and helios micrometeoroid experiments. J. Phys. E: Sci. 6, 209–217.

[25] Duncan, N., Sternovsky, Z., Grün, E., Auer, S., Horányi, M., Drake, K., Xie, J., Lawrence, G., Hansen, D., Le, H., 2011. The Electrostatic Lunar Dust Analyzer (ELDA) for the detection and trajectory measurement of slow-moving dust particles from the lunar surface. Planet. Space Sci. 59, 1446–1454.

[26] Durin, C., Mandeville, J., 2009. Sodad: first resutls and post-flight analysis. 11th ISMSE, 1–6.

[27] Flandes, A., Krüger, H., Loose, A., Sperl, M., Seidensticker, K. J., Ficher, H. H., Arnold, W., 2013. Dust impact monitor (DIM) onboard Rosetta/Philae: Comparison of experimental results and the theory behind the experiment. Planet. Space. Sci. 84, 122–130.

[28] Friichtenicht, J., 1962. Two-million-volt electrostatic accelerator for hypervelocity research. Rev. Sci. Instrum. 33, 209.

[29] Gaier, J. R., 2005. The effect of lunar dust on EVA systems during the Apollo missions. NASA/TM-2005-213610.

[30] Göller, J. R., Grün, E., Mass, D., 1980. Calibration of the DIDSY-IPM dust detector and application to other impact ionisation detectors on board the P/Halley probes. Astronmy and Astrophys 85, 5841–5852.

[31] Goodwin, R., 1973. Apollo 17 NASA mission reprot. JSC-07904.

[32] Grün, E., Fechtig, F., Hanner, M. S., Kissel, J., Linkert, B. A., Maas, D., Morfill, G. E., Zook, H. A., 1992. The Galileo dust detector. Space Sci. Rev. 60, 317–430.

[33] Grün, E., Horányi, M., 2013. A new look at Apollo 17 LEAM data: Nighttime dust activity in 1976. Planet. Space Sci. 89, 2–14.

[34] Grün, E., Horányi, M., Sternovsky, Z., 2011. The lunar dust environment. Planet. Space Sci. 59, 1672–1680.

[35] Grün, E., Zook, H. A., Fechtig, H., Giese, R. H., 1985. Collisional balance of the meteoritic complex. Icarus 62, 244–272.

[36] Hansson, H., Skoglund, P., 2002. Simulation of concrete penetration in 2d and 3d with the RHT material model. Tech. rep., SWEDISH DEFENCE RESEARCH AGENCY.

[37] Hartmann, W. K., Davis, D. R., 1975. Satellite-sized planetesimals and luanr origin. ICARUS 24, 504–515.

[38] Heiken, G. H., Vaniman, D. T., French, B. M., 1991. Lunar sourcebook: A user's guide to the moon. Cambridge University Press.

[39] Hermann, W., 1969. Constitutive equation for the dynamic compaction of ductile porous materials. J. Appl. Phys. 40, 2490–2499.

[40] Hernalyn, B., Schultz, H., 2010. Early-stage ejecta velocity distribution for vertical hypervelocity impacts in to sand. Icarus 209, 866–870.

[41] Hoerth, T., Schäfer, F., Thoma, K., Kenkmann, T., M, H, P., Lexow, B., Deutsch, A., 2013. Hypervelocity impact on dry and wet sandstone: observationa of ejecta dynamic and crater growth. Meteorit. Planet. Sci. 1, 23–32.

[42] Hoffmann, H.-J., Fechtig, H., Gün, E., Kissel, J., 1975. Temporal fluctuations and anisotropy of the micrometeoroid flux in the Earth-Moon system measured by HEOS 2. Planet. Space. Sci. 23 (6), 985–991.

[43] Horányi, M., 1996. Charged dust dynamics in the solar system. Annu. Rev. Astrophys. 34, 383–418.

[44] Horányi, M., Gagnard, S., Gathright, D., Gün, E., James, D., Kempf, S., Lankton, M., Srama, R., Sternosky, Z., Szalay, J., 2014. Lunar Dust Experiment (LDEX): First results. European Geosciences Union General Assembly 2014.

[45] Horányi, M., Hoxie, V., James, D., Poppe, A., Bryant, C., Grogan, B., Lamprecht, B., Mack, J., Bagenal, F., Batiste, S., Bunch, N., Chanthawanich, T., Christensen, F., Colgan, M., Dunn, T., Drake, G., Fernandez, A., Finley, T., Holland, G., Jenkins, A., Krauss, C., Krauss, E., Krauss, O., Lankton, M., Mitchell, C., Neeland, M., Reese, T., Rash, K., Vaudrin, C., Westfall, J., 2008. New Horizons: Reconnaissance of the Pliuto-Charon system and the Kuiper Belt. Space Sci. Rev. 140, 387–402.

[46] Horányi, M., Sternovsky, Z., Srama, R., 2009. The Lunar Dust EXperiment (LDEX) for the Lunar Atmosphere and Dust Environment (LADEE) mission. 40th Lunar Planet. Sci. Con., 1741–1742.

[47] Horányi, M., Szalay, J. R., Kempf, S., Schmidt, J., Gün, E., Srama, R., Sternosky, Z., Szalay, J., 2015. A permanent, asymmetric dust cloud around the Moon. Nature 522, 324–326.

[48] Hörz, F., Brownlee, D. E., Fechtig, H., Hartungand, J. B., Morrison, D. A., Neukum, G., Schneider, E., Vedder, J. F., Gault, D. E., 1975. Lunar microcraters: Implication for the micrometeorid complex. Planet. Space Sci. 23, 151–172.

[49] Humes, D. H., 1980. Results of Pioneer 10 and 11 Meteoroid Experiments: Interplanetary and near-saturn. J. Geophy. Res. 85, 5841–5852.

[50] Kassel, J., Glasmachers, A., Grün, E., Henkel, H., 2003. Cometray and interstellar iust analyzer for comet Wild 2. Jour. Geophys. Res. 108, 8114(1–10).

[51] Kassel, P. C., 1973. Characteristics of capacitor-type micrometeoroid flux detecors when impacted with simulated micrometeoroids. NASA TN D-7359, 1–38.

[52] Kempf, S., Srama, R., Altobelli, N., Auer, S., Tschernjawski, V., 2004. Cassini between Earth and asteroid belt:first in-situ charge measurements of interplanetary grains. Icarus 171, 317–335.

[53] Kissel, J., 1986. The Giotto particulate impact analyzer. ESA SP-1007, 67–83.

[54] Krüger, H., Krivov, A. V., Grün, E., 2000. A dust cloud of Gmanymede maintained by hypervelocity imoacts of interplantary micrometeoroids. Planet. Space Sci. 48, 1457–1471.

[55] Landgraf, M., Baggaley, W. J., Grün, E., Krüger, H., Linkert, G., 2000. Aspects of the mass distribution of interstellar dust grains in the solar system from in-site measurements. Jour. Geophys. Res. 105, 10343–10352.

[56] Li, Y. W., Srama, R., Henkel, H., Sternovsky, Z., 2014. Instrument study of the Lunar Dust eXplorer (LDX) for a lunar lander mission. Adv. Space. Res.

[57] Linnarsson, D., Carpenter, J., Fubini, B., Gerde, P., 2012. Toxicity of lunar dust. Planet. Space. Sci. 74, 57–71.

[58] Liu, Y., Schnare, D., Park, J. S., Hill, E., Eimer, B., Taylor, L. A., 2007. Shape analyses of lunar dust particles for astronaut toxicological studies. 38nd Lunar and Planetary Science Conference, 1383(1–2).

[59] Ma, Q., Matthews, S., Hyde, T. W., 2011. Charging of interplanetary dust grains and consequences for aggregation. 42nd Lunar and Planetary Science Conference, 1981(1–2).

[60] McCoy, J. E., 1976. Photometric studies of light scattering above the lunar terminator from Apollo solar corona photography. Proc. Lunar Sci. Conf. 7th, 1087–1112.

[61] Murphy, D. L., Vondrak, R. R., 1993. Effects of levitated dust on astronnomical observations form the lunar surface. 24nd Lunar and Planetary Science Conference, 10331–1034.

[62] NASA, 1972. The project Apollo image.
URL http://www.apolloarchive.com/apollo_gallery.html

[63] O'Brien, B. J., 2011. Review of measurements of dust movements on the moon during apollo. Planet. Space Sci. 59, 1708–1726.

[64] Perkins, D., 1976. Analysis of the LEAM experiemnt response to charged particles. BSR4233.

[65] Rhee, J. W., Berg, O. E., Richardson, F. F., 1974. Heliocentric distribution of cosmic dust intercepted by Pioneer 8 and 9. Geophy. Res. Letters 1 (8), 345–346.

[66] Riedel, W., Kawai, N., Kondo, K., 2009. Numerical assessment for impact strength measurements in concrete materials. Int. J. Impact Eng. 36, 283–293.

[67] Sickafoose, A. A., 1999. Experimental dust charging and dynamics with applications for planetary environments. Ph.D dissertation, University of Colorado.

[68] Simpson, J. A., Rabinowitz, D., Tuzzolino, A. J., Ksanfomality, L. V., 1987. The dust coma of comet P/Halley: measurments on the Vega-1 and Vega-2 spacecrfat. Astron. Astrophys. 187, 742–752.

[69] Simpson, J. A., Tuzzolino, A. J., 1985. Ploarized ploymer films as electronic pluse detectors of cosmic dust particles. Space Sci. Rev. A236, 187–202.

[70] Singer, S. F., Stanley, J. E., Kassel, P., 1985. The ldef interplanetary dust experiment. Astrophysics and Space Science Library 119, 117–120.

[71] Software, I. E., 2010. COULOMB 3D electric: V9.0 quick start guide. Integrated Engineering Software.

[72] Srama, R., Ahrens, T. J., Altobelli, N., Auer, S., 2004. The Cassini cosmic dust analyzer. Space Sci. Rev. 114, 465–518.

[73] Srama, R., Ahrens, T. J., Altobelli, N., Auer, S., Bradley, J. G., 2004. The cassini cosmic dust analyzer. Space Sci. Rev. 114 (465-518).

[74] Srama, R., Auer, S., 2008. Low-charge detector for the monitoring of hyper-velocity micron-sized dust particles. Meas. Sci. Technol. 19, 055203(1–8).

[75] Srama, R., Srowig, A., Auer, S., Harris, D., Helfert, S., 2007. A trajectory sensor for sub-micron sized dust. ESA SP-643.

[76] Stubbs, T., Vovdrak, R., Farrel, W. M., 2006. A dynamic fountain model for lunar dust. Adv. Space Res. 37, 59–66.

[77] Szalay, J., Horanyi, M., 2012. Modeling dust cloud on the moon. 43(rd) Lunar and Planetary Science Conference, 1796(1–2).

[78] Team, L. L., 2012. European Lunar Lander - Experiment interface definition document: Part A (EID-A). Tech. rep., ESA.

[79] Tuzzolino, A. J., Economou, T. E., McKibben, R. B., Simpson, J. A., McDonnell, J. A. M., Burchell, M. J., 2003. Dust flux monitor instrument for the Stardust mission to comet Wild 2. Icarus 108, 8115(1–24).

[80] Wang, X., Horányi, M., Robertson, S., 2010. Investigation of dust transport on the lunar surface in a laboratory plasma with an electron beam. J. Geophys. Res. 115, A11102(1–6).

[81] Whipple, F. L., 1961. The dust cloud about the earth. Nature 189, 127–128.

[82] Wilkinson, J., 2010. The Moon in close-up. Springer.

[83] Willis, M. J., Burchell, M. J., Willis, M. J., Ahrens, T. J., 2005. Decreased values of cosmic dust number density estimates in the solar system. Icarus 176, 440–452.

[84] Winters, D., Vogel, M., Segal, D., Thompson, R., 2006. Electronic detection of charged particle effects in a penning trap. J. Phys. B: At. Mol. Opt. Phys. 39, 3131(1–16).

[85] Wyatt, S., 1969. The electrostatic charge of interplanetary grains. Planet. Space Sci. 17, 155–171.

[86] Xie, J., Sternovsky, Z., Auer, S., Drake, K., Grün, E., Horányi, M., Le, H., Srama, R., 2013. Laboratory testing and data analysis of the Electrostatic Lunar Dust Analyzer (ELDA)instrument. Planet. Space Sci. 89, 63–70.

[87] Xie, J., Sternovsky, Z., Grün, E., Auer, S., Duncan, N., Drake, K., Le, H., Horányi, M., Srama, R., 2011. Dust trajectory sensor: Accuracy and analysis. Rev. Sci. Instrum. 82, 105104(1–11).

[88] Yano, H., Hirai, T., Okamoto, C., Fujii, M., Tanaka, M., Moriyama, N., Burchell, M., 2013. Heliocentric variation of cosmic dust flux measured by the IKAROS-ALADDIN between the earth and venus. 44th Lunar and Planetary Science conference abstract.

[89] Zook, H. A., 1991. Deriving the velocity distribution of meteoroids from the measured meteoroid impact directionality on the various ldef surfaces. NASA CP 3134, Part 1, 569–579.

[90] Zook, H. A., Lange, G., Grün, E., Fechtig, H., 1984. Lunar primary and secondary microcraters and the micrometeoroid flux. Lunar Planet. Sci. XV, 965–966.

Acknowledgements

First and foremost I want to thank my advisor Dr.Ing Ralf Srama. It has been an honor to be his first PhD student in University of Stuttgart. He has taught me, both consciously and un-consciously, how good experimental study is done. I appreciate all his encouragements, advices and generous supports to make my PhD pursuit productive and stimulating. I am also thankful for the excellent example he provided both for life and work. Prof. Dr. Eberhard Grün can always get many useful actives and encouragements during discussions. He knows almost everything about the cosmic dust. I am motivating by the joy and enthusiasm he has for research.

The Cosmicdust group is a source of friendships, advice and collaboration. My collogues have contributed immensely to my personal life and professional time in Germany. I am especially grateful Sebastian Bugiel who operates the accelerator for all the experiments relating to this thesis. I would like also acknowledge his suggestions during the instrument laboratory model building up. In regard to the electric parts, I thank Heiko Strack and Günther Baust who help me for developing the amplifiers, they also give me a lot of background information and advice to understand the functionality and electronics of the detector and its components. For induced charge simulation, Prof. Siegfried Auer, Dr. Zoltan Sternovsky, Dr. Jianfeng Xie and Anthony Shu gave me many suggestions for the Coulomb software and dust trajectory detector.

I have appreciated all my collogues in Max Planck institute for nuclear physics: Anna Mocker, Katharina Otto, Khalisi Emil and Katherina Fiege; in University of Stuttgart: Rachel Soja, Anja Schilling and Georg Moragas-Klostermeyer; in University of Heidelberg: Prof. Mario Trieloff, Nozair Khawaja, Massimo Guglielmino and René Reviol; and in University of Kent: Dr. Jon Hillier and Dr. Mark Price.

I gratefully acknowledge the funding sources which made my PhD work possible. This work was founded by Deutsches Zentrum für Luft-Raumfart (DLR), Grant project number: 50 OW 0903. I also supported by the China Scholarship Council (CSC).

Lastly, I would like to thanks my parents, my older brother, my loving girlfriend and all families!